



**UNIVERSITÀ  
DEGLI STUDI  
DI TRIESTE**

# **UNIVERSITÀ DEGLI STUDI DI TRIESTE**

## **XXXIII CICLO DEL DOTTORATO DI RICERCA IN NANOTECNOLOGIE**

### **“Comprehensive Characterization and Effective Combinatorial Targeting of Epithelial Ovarian Cancer and High-Grade Serous Ovarian Cancer via Single-cell Analysis.”**

Settore scientifico-disciplinare: **MED/08**

**DOTTORANDO / A  
DOMENICO TIERNO**

**COORDINATORE  
PROF. ALBERTO MORGANTE**

**SUPERVISORE DI TESI  
PROF. SERENA BONIN**

**ANNO ACCADEMICO 2019/2020**

# TABLE OF CONTENTS

<b>ABSTRACT .....</b>	<b>1</b>
<b>1. INTRODUCTION .....</b>	<b>3</b>
<b>1.1 Ovarian Cancer .....</b>	<b>3</b>
1.1.1 Epidemiology .....	3
1.1.2 Pathologic Classification of Ovarian Cancer .....	4
1.1.3 Epithelial Ovarian Cancer .....	5
1.1.4 Low Grade Serous Ovarian Cancer .....	7
1.1.5 Clear Cells Ovarian Cancer .....	8
1.1.6 Endometrioid Ovarian Cancer .....	10
1.1.7 Mucinous Ovarian Cancer .....	11
<b>1.2 High Grade Serous Ovarian Cancer .....</b>	<b>13</b>
1.2.1 Epidemiology and Risk Factors .....	13
1.2.2 Carcinogenesis .....	13
1.2.3 Morphological Features .....	15
1.2.4 Molecular Features .....	18
<b>1.3 Prognosis and Treatment of Ovarian Cancer .....</b>	<b>19</b>
1.3.1 Prognosis .....	19
1.3.2 Ovarian Cancer Treatments .....	21
<b>1.4 Biomechanics and Atomic Force Microscope .....</b>	<b>22</b>
1.4.1 Role of Mechanical Features in Biological Specimens .....	22
1.4.2 Atomic Force Microscope .....	24
1.4.3 Application of Atomic Force Microscope in Biology .....	25
<b>1.5 The Ubiquitin-Proteasome System .....</b>	<b>28</b>
1.5.1 Proteolysis .....	28
1.5.2 Ubiquitination .....	29
1.5.3 Proteasome .....	29
1.5.4 Deubiquitination .....	30
1.5.5 Inhibitors of Ubiquitin-Proteasome system for tumor treatment .....	31
1.5.6 The inhibitors G5 and 2C .....	32
<b>2. AIM OF THE STUDY .....</b>	<b>34</b>
<b>3. MATERIALS AND METHODS .....</b>	<b>35</b>
<b>3.1 Cell lines .....</b>	<b>35</b>

3.1.1	Culture Methods and Cell Lines Features .....	35
3.1.1.1	CAOV3 .....	35
3.1.1.2	HEY .....	36
3.1.1.3	IGROV1 .....	36
3.1.1.4	OAW42 .....	37
3.1.1.5	OVCAR4 .....	37
3.1.1.6	OVCAR8 .....	38
3.1.1.7	SKOV3 .....	38
3.1.1.8	TYKNU and TYKNU CpR .....	38
3.1.2	Histological Classification .....	40
3.1.3	Morphological Classification .....	41
3.1.4	Cell Count and Viability Assay .....	43
<b>3.2</b>	<b>AFM .....</b>	<b>45</b>
3.2.1	Cell Seeding .....	47
3.2.2	AFM Set-up .....	48
3.2.2.1	<i>Cantilever Functionalization</i> .....	48
3.2.2.2	<i>Cantilever Elastic Constant Calibration</i> .....	48
3.2.3	AFM Measurements .....	50
3.2.4	Data Analysis .....	50
3.2.5	Variation in Experimental Set-up .....	51
<b>3.3</b>	<b>Invasion Assay .....</b>	<b>52</b>
<b>3.4</b>	<b>2C Treatment .....</b>	<b>54</b>
3.4.1	2C Sensitivity Assessment .....	55
3.4.2	2C Uptake Assay .....	57
3.4.3	AFM Measurements of Treated Cell Lines .....	58
3.4.4	Immunofluorescence Assay .....	58
3.4.4.1	<i><math>\beta</math>-Tubulin</i> .....	58
3.4.4.2	<i>F-Actin</i> .....	60
3.4.4.3	<i>Analysis of Cytoskeleton Distribution</i> .....	60
<b>3.5</b>	<b>Statistical Analysis .....</b>	<b>61</b>
<b>4.</b>	<b>RESULTS .....</b>	<b>62</b>
<b>4.1</b>	<b>Cell Lines Classification .....</b>	<b>62</b>
4.1.1	Histological Classification .....	62
4.1.1.1	CAOV3 .....	62
4.1.1.2	HEY .....	62

4.1.1.3	<i>IGROV1</i>	62
4.1.1.4	<i>OAW42</i>	63
4.1.1.5	<i>OVCAR4</i>	63
4.1.1.6	<i>OVCAR8</i>	63
4.1.1.7	<i>SKOV3</i>	64
4.1.1.8	<i>TYKNU and TYKNU CpR</i>	64
4.1.2	Morphological Classification	65
<b>4.2</b>	<b>Mechanical Characterization</b>	<b>66</b>
4.2.1	Average Young's Modulus	66
4.2.2	Young's Moduli Distribution	69
4.2.3	Effects of Variation in Experimental Set-up	72
<b>4.3</b>	<b>Metastatic Potential</b>	<b>73</b>
<b>4.4</b>	<b>2C Treatment</b>	<b>76</b>
4.4.1	IC50 Assessment	76
4.4.2	Average Young's Modulus after 2C Treatment	78
4.4.3	Young's Moduli Distribution after 2C Treatment	80
4.4.4	Time-depending Effects on Young's Modulus of 2C Treatment	83
<b>4.5</b>	<b>Fluorescence Assay</b>	<b>85</b>
4.5.1	Uptake Assay	85
4.5.2	F-Actin Staining	86
4.5.3	$\beta$ -Tubulin Staining	90
4.5.4	Analysis of Cytoskeleton Distribution	93
<b>5.</b>	<b>DISCUSSION</b>	<b>96</b>
5.1	Histological, Morphological and Mechanical Characterization	97
5.2	Invasion Assay	98
5.3	2C Treatment	100
5.3.1	Mechanical Properties and 2C Sensitivity	100
5.3.2	Kinetics of 2C Uptake and Action	101
5.3.3	2C Effects on Cytoskeleton	101
5.4	Effects on Mechanical Properties of Culture Medium Composition	103
<b>6.</b>	<b>CONCLUSIONS</b>	<b>104</b>
<b>7.</b>	<b>REFERENCES</b>	<b>106</b>

# Abstract

Ovarian cancer kills more than 40 000 women in Europe and more than 150 000 women globally each year. The epithelial ovarian cancer (EOC) is the most common subtype and encompasses a collection of neoplasms with distinct clinical-pathological, molecular features and prognosis; among them the most common are the clear cells (CCOC), the mucinous (MOC), the endometrioid (ENOC), the low grade serous (LGSOC) and the high grade serous ovarian cancer (HGSOC). The HGSOC, in particular, is the most deadly form of EOC due to its high intratumor heterogeneity and lack of early diagnosis. The mechanical properties can be useful as new possible biomarkers of EOC subtypes in association to the classic ones used in clinical routine. In this thesis, the mechanical characterization of 9 ovarian cancer cell lines with different histological and morphological classification was carried out by AFM. Then, the achieved mechanical properties were evaluated on the same cell lines as markers of metastatic potential and drug sensitivity against 2C, a compound synthesized by the group of prof. Benedetti at the University of Trieste with anti-tumoral and cytoskeleton depolymerizing activity. Finally, an assessment of the effects of the culture medium composition on mechanical properties was performed.

The mechanical characterization showed that the HGSOC cell lines had a high variability in the average Young's modulus and resulted stiffer than the other cell lines with different histological classification. Moreover, the cell lines displayed two distinct single cell Young's moduli distribution patterns: unimodal and bimodal. The cell lines with bimodal pattern showed two different populations with distinct mechanical behaviors.

The invasion assay indicated a correlation between the stiffness decrease and the increase of invasion capacity. Accordingly, in cell lines with bimodal pattern only the "softer" population showed eventually the metastatic potential to invade.

The cell lines with bimodal pattern were more resistant to 2C than the ones with unimodal pattern. For cell lines with bimodal pattern, the "stiffer" population had tendentially a higher resistance to 2C than the "softer" one. The F-actin network organization could influence the 2C resistance and the stiffness of cell lines: the HEY and OVCAR4 (high 2C resistance and high average Young's modulus) had an Actin cytoskeleton more distributed over the cell than the TYKNU (low 2C resistance and low average Young's modulus).

Finally, variations in the culture medium components had an impact on the achieved Young's moduli. This highlighted the need to develop optimized culture protocols for elasticity measurements, able to overcome the effects of different media on the mechanical properties.

# 1.INTRODUCTION

## 1.1 Ovarian Cancer

### 1.1.1 Epidemiology

Ovarian cancer (OC) is the seventh most common cancer and the fifth cause of cancer death among females [1]. In 2018, as reported by Global Cancer Observatory [2], OCs have accounted for 3.4% of all female cancer diagnoses and for 4.4% of all female cancer deaths.

A higher incidence of OC has been estimated in USA, Eastern and Centre Europe (>8 for 100 000 inhabitants) than Africa and Asia (<3 for 100 000 inhabitants) (**Figure 1.1**). Moreover, the incidence rate is dependent by age: OC is rare in young women, (<30 age) while occurrence drastically increases after the age of 50, with a peak between 50 and 70 years [3].

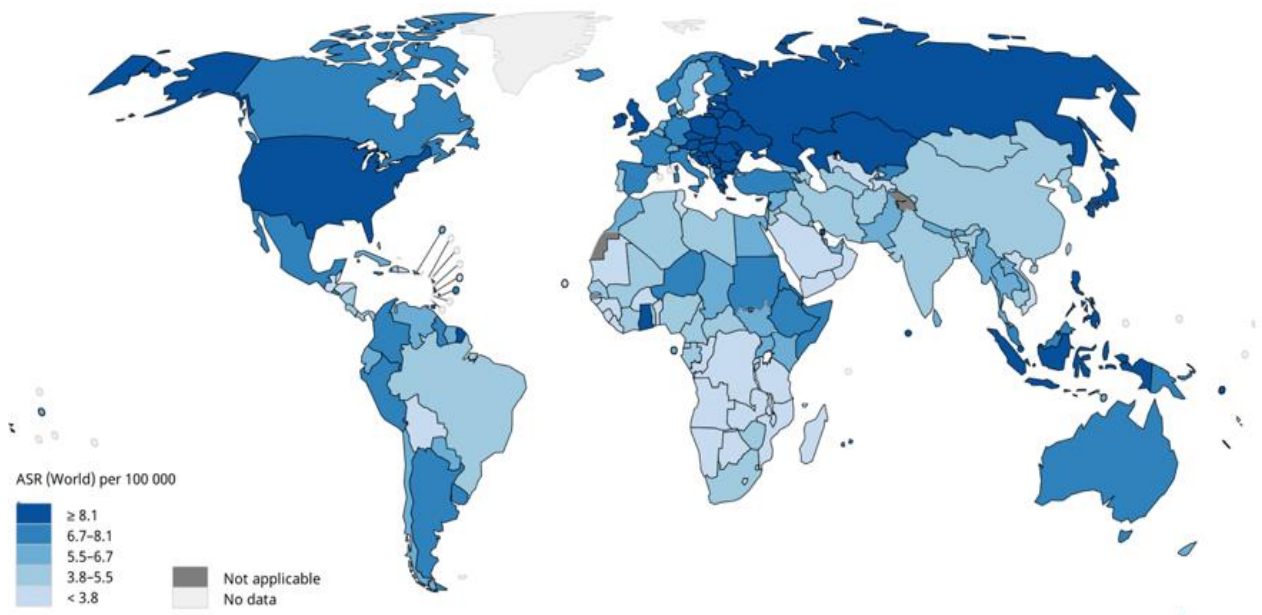


**Figure 1.1:** Global incidence of Ovarian Cancer in 2018. ASR: age-standardized rates [49].

Despite the progresses in understanding OC biology, the carcinogenesis of this tumor remains poorly understood. This is due to late diagnosis and molecular heterogeneity of OCs. As a consequence, the assessment of risk factors is clinically difficult and is primarily based on family history [4].

The high heterogeneity is one of the main causes of lack of molecular and tissue biomarkers allowing an efficient screening of OCs. This hampers its diagnosis in early stage and consequently a better prognosis and survival of patients.

Advances in cancer research and medical practice have determined an increase of the 5-year survival rate from 33.7% (1975) to 46.6% (2009) [4], but the lack of an efficient screening method and treatment hinders the improvement of survival rate over this value.

### 1.1.2 Pathologic Classification of Ovarian Cancer

Ovarian cancer encompasses a collection of neoplasms with distinct clinicopathological and molecular features and prognosis. The current classification splits ovarian tumors into three groups according to their anatomic site of origin:

- *Epithelial tumors (EOC)*: these tumors originate from ovarian surface epithelium (OSE) or from extra-ovarian epithelia and account for 60% of all ovarian cancers and for 90% of all malignant ovarian tumors. The EOCs can be further classified in subtypes according to their histology [5].
- *Sex cord-stromal tumors (SC-SOC)*: these tumors originate from gonadal stroma cells (e.g. Granulosa cells, theca cells, Sertoli cells and Leydig cells) and account for 8% of all OCs and for 5-6% of all malignant ovarian tumors [5][6]. These tumors are often characterized by consistent endocrine manifestations and for this reason are easily diagnosable. The granulosa cell tumors are the most common SC-SOC subtypes [7].
- *Germ cell tumors (GOC)*: these tumors originate by primordial germ cells and account for about 25% of all OCs, but only for 2-3% of all malignant ovarian tumors [5]. The GOCs typically occur in children and adolescent (about 50% of OCs in young women are GOCs) and 33% of these are malignant. These tumors are relatively uncommon in adult and are mostly benign [6].

Each category has different subtypes that can be often found in different combination within a single tumor. These kinds of tumors are called mixed (for the classification only subtypes that accounts for >10% of total tumor mass are considered) [6].

### 1.1.3 Epithelial Ovarian Cancer

The epithelial ovarian cancers (EOCs) are the most common and deadly OCs and constitute a heterogeneous group of neoplasms with different behavior, epidemiology, molecular profile and prognosis [8]. According to current classification, the EOCs are divided into nine groups [9]:

- Serous tumors (SOC): characterized by two different subtypes, high grade and low grade
- Endometrioid tumors (ENOC)
- Clear Cells tumors (CCOC)
- Mucinous tumors (MOC)
- Brenner tumors (BOC)
- Seromucinous tumors (SMOC)
- Mesenchymal tumors (MesOC)
- Mixed epithelial tumors (MixOC): composed by two or more subtypes of common EOCs.
- Undifferentiated tumors (UOC).

Among them the high grade serous carcinoma (HGSOc, 70% of all EOCs cases), the low grade serous carcinoma (LGSOC, <5% of all EOCs), the endometrioid carcinoma (10%), the clear cell carcinoma (10%) and the mucinous carcinoma (3%) are by far the most common and representative subtypes [5]. A correct diagnosis of these subtypes is a key point in EOC management, because each one needs a different treatment approach. The classification of ovarian cancer is now highly reproducible using modern diagnostic criteria supplemented (when necessary) by immunohistochemistry [10] (**Figure 1.2**).

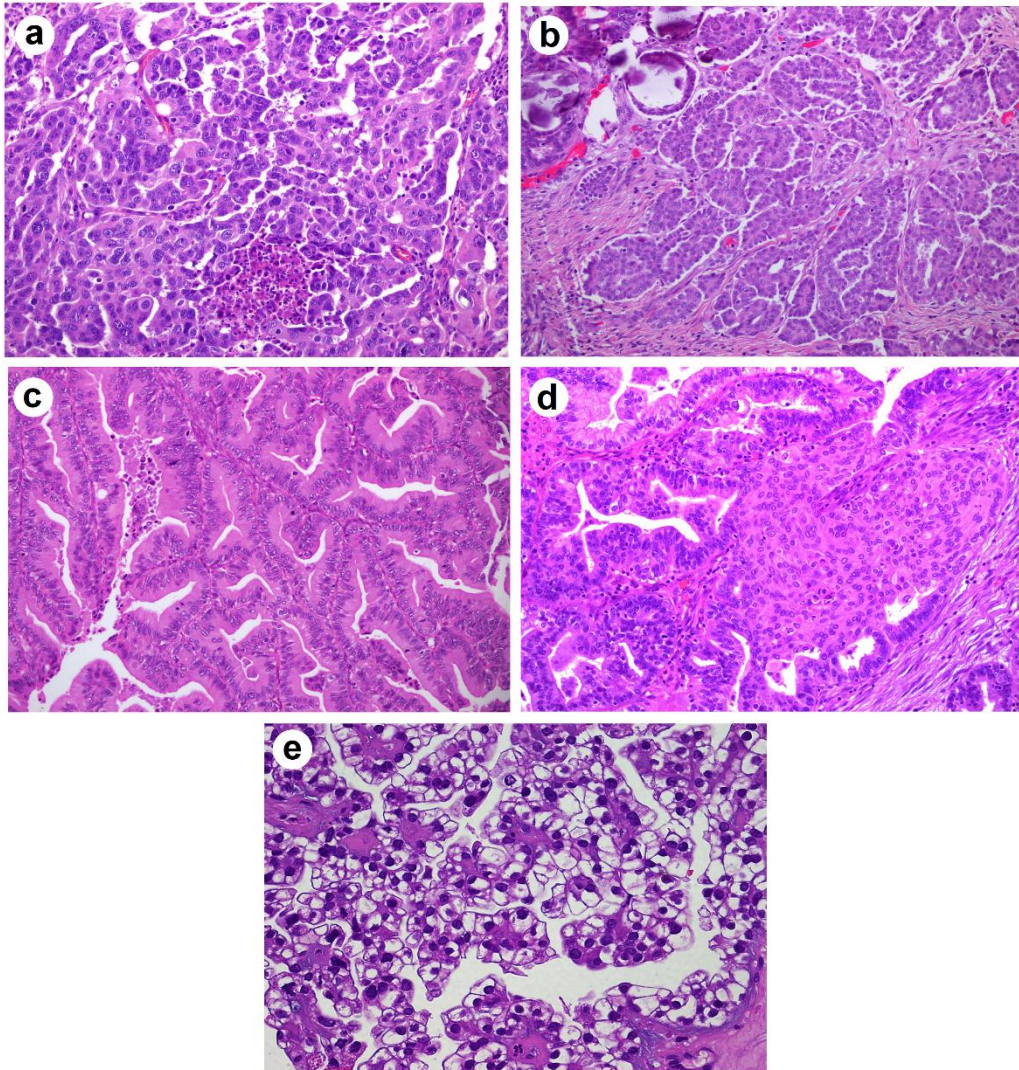


**Figure 1.2:** Representative histological H&E images (200x magnification) of most common EOCs subtypes: a) HGSOc, characterized by solid masses of cells with glandular lumens, nuclear atypia and necrosis; b) LGSOC, papillary architecture characterized by cells with small and uniform nuclei c) MC, shows expansile invasion and closely packed malignant glands with no stromal response d) ENOC, well-differentiated adenocarcinoma characterized by confluent growth of glands and squamous cells e) CCOC, with clear cells lined to papillae and hyalinized cores [8].

### 1.1.4 Low Grade Serous Ovarian Cancer

LGSOC is a rare form of epithelial ovarian cancer that accounts annually for 5-10% of all ovarian cancers diagnosed in Canada and United States [11][12]. This tumor is mildly aggressive but is usually highly resistant to chemotherapy (response rate is 4-25%). For this reason, the survival rate at ten years from diagnosis is only of 10-20% [13].

The LGSOCs have a slow tumoral growing and are usually diagnosed at an earlier median age than the high grade counterpart (around 50 years versus around 60 years) [14]. This tumor origins mostly from a Mullerian epithelium which can arise in ovary in three different ways: 1) Cortical inclusion cysts (CICs) originated from salpingeal cells of fallopian tubes, 2) metaplasia of ovarian surface epithelial cells (OSE), 3) retrograde passage of endometrial epithelium [14].

The molecular characterization of this tumor has showed rare mutations at TP53 (only 8%) [15] and a widespread expression of estrogen and progesterone receptors (ER and PR respectively) [16]. Moreover, LGSOCs are characterized by activating mutations of genes involved in MAPK pathway, such as KRAS (20-40%), NRAS (7-26%) and BRAF (5-33%) [17][18]. The involvement of MAPK pathway in LGSOC has led to consider MEK inhibitors (like selumetinib or binimetinib) as candidates for an efficient therapeutic approach [19].

Other possible molecular biomarkers for LGSOC are mutations at USP9X and EIF1AX (genes involved in mTOR pathway, they are mutated in 11% and 15% of all LGSOC cases respectively) and the overexpression of PAX2, AGR3 and IGF-1 (**Fig 1.3**). In contrast with high grade serous tumors, the low grade ones are characterized by chromosomal stability [14].

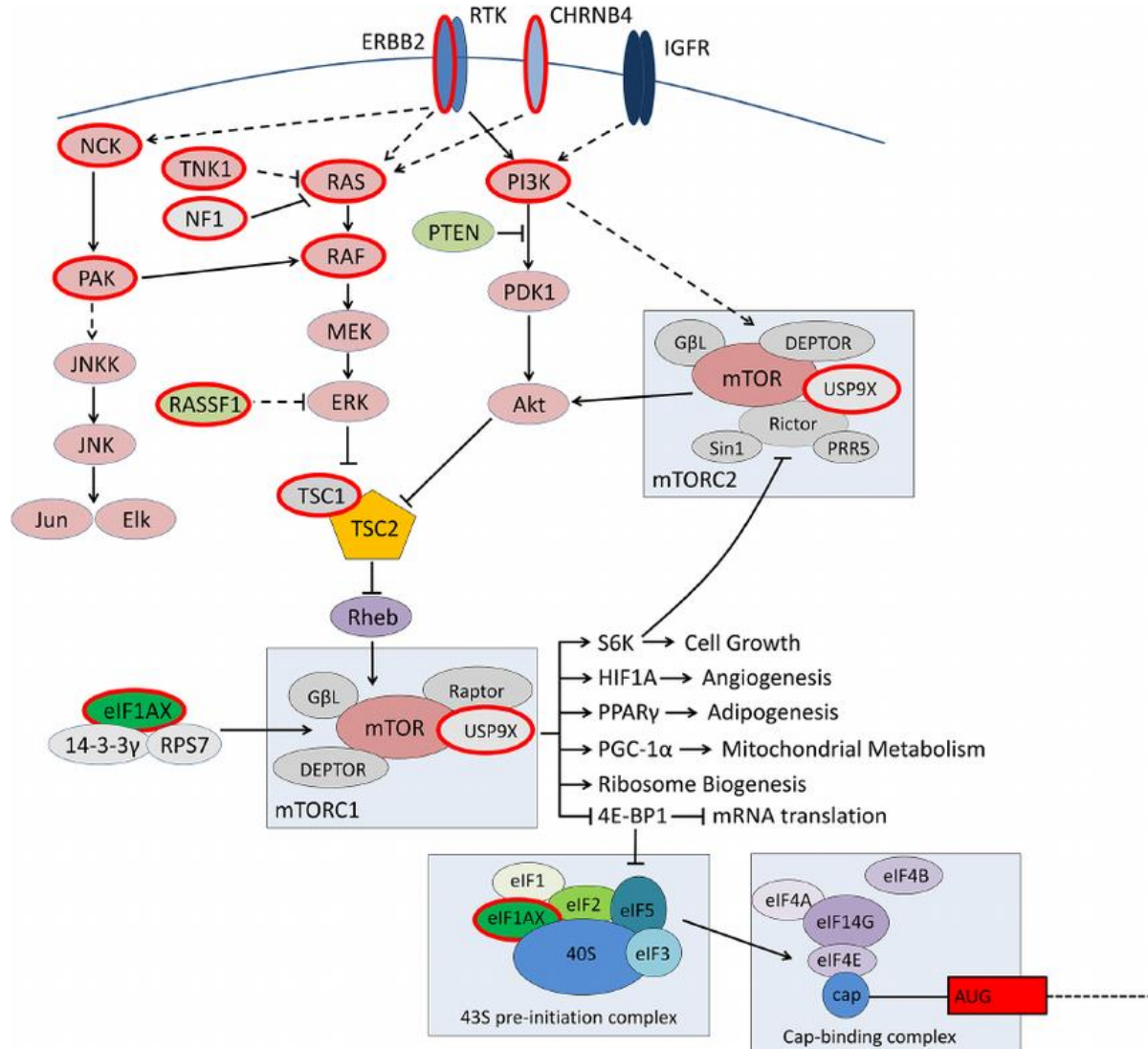


**Figure 1.3:** Molecular drivers in LGSOC. In red are circled the protein mutated [165].

### 1.1.5 Clear Cells Ovarian Cancer

The Clear cells ovarian tumor (CCOC) is a subtype of EOC characterized by high aggressiveness and resistance to platinum based chemotherapies [20]. These tumors are usually associated to endometriosis, which is identified in 50% of all CCOCs cases [21] and is widely described as principal precursor of CCOC [22]. The presence of endometriosis is related to good prognosis [23].

The median age of diagnosis of CCOC is lower than serous carcinoma (around 55 years versus 64 years). In the early stage the prognosis is good: the five years survival rate in patients with stage I is 84-100% [24]. Nevertheless, CCOCs cases diagnosed at advanced stage show a poorer outcome in comparison to the corresponding ones at early stage [25]. Moreover, the recurrence of this tumor is relatively common and tends to occur in different sites: 62% of CCOC patients indeed, show multiple-recurrence sites in pelvis, extra-pelvis, intrathorax, lymphonode and meninges [26]. Relapsed CCOCs patients have a poor prognosis: the survival rates at one, two and five years from recurrence are 67.8%, 93.1% and 13.2% respectively [27].

From a morphological point of view, CCOC is characterized by different patterns (papillary, tubulocystic and solid mixed in different combination) and eosinophilic clear cells. Moreover, the tumor can show a background endometriosis or a clear cell adenofibroma [28].

The molecular profile of CCOC shows a remarkable percentage of mutations in ARID1A (around 50% of all cases), a gene that plays an important role in the chromatin remodeling complex SWI/SNF [29]. The presence of dysfunction in SWI/SNF complex as biomarker for CCOC is further proved by mutations in other genes involved in the chromatin remodeling pathway, such as ARID1B and SMARCA4 (6-18% and 5-18% of all CCOC cases respectively) [30] (**Figure 1.4a**).

Another gene often mutated in CCOC is PIK3CA (around 50% of case), the activity of which is increased by mutation and leads to altered activation of the downstream AKT pathway (**Figure 1.4b**). Mutations in PIK3R1 (7-10% of all cases) and PTEN (2-13%), in addition to the amplification of AKT2 (8-26.6%), indicate frequent alterations of AKT pathway in CCOC [31].

Aberrations in chromatin remodeling pathway and AKT pathway are closely correlated in CCOC. ARID1A and PIK3CA were, indeed, found co-mutated in 20-56% of cases, while 82% of tumors with activation in AKT pathway present also mutations in components of SWI/SNF complex [30].

Other typical molecular alterations of CCOC are: PPP2R1A mutations (4.1-20%), KRAS mutations (4.7-20%) [20], ERBB2 mutations and amplifications (4-13%) [30] (**Figure 1.4c**), MET amplifications (24-37%) [32] and TERT mutations (5.7-16.0%, the highest frequency among EOC subtypes) [33]. Finally, TP53 is usually wild-type and BRCA1/2 have a low mutation frequency [30].

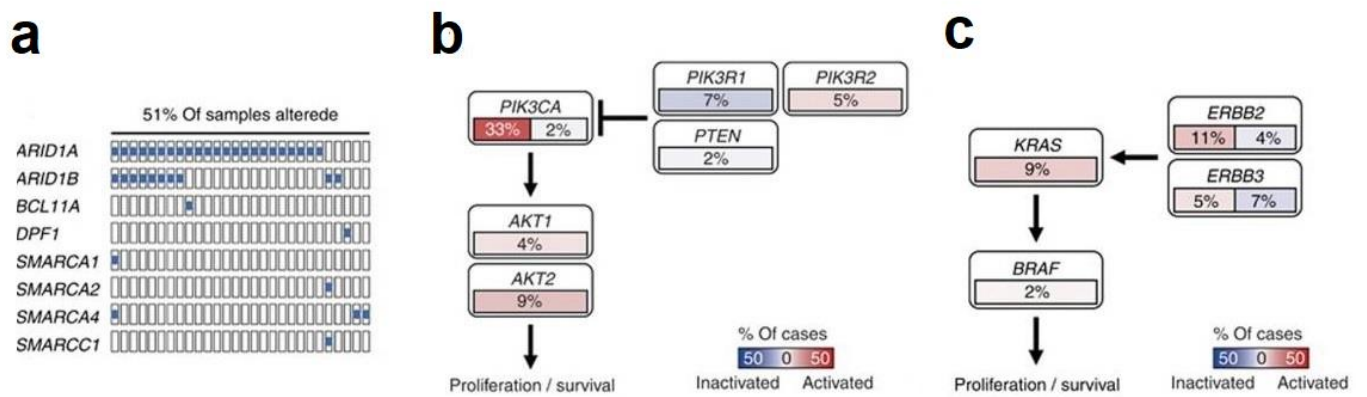


**Figure 1.4:** a) Pattern of gene mutations of SWI/SNF family subunit; b) Pattern of genes alterations in AKT pathway; c) Pattern of genes alterations in RTK/RAS pathway. Adapted from Itamochi [30].

### 1.1.6 Endometrioid Ovarian Cancer

The endometrioid ovarian cancer (ENOC) is a EOCs subtype characterized by a high proportion of cases with well differentiated histology and early stage diagnosis (50% of all cases are diagnosed at stage I and II) [34]. This tumor arises from endometriosis and often is associated to synchronous endometrial carcinoma (with which share many molecular and histologic features) [35]. ENOC patients have tendentially a good outcome (five-years survival rate is 78%) [36], regardless to their stage and differentiation level [34]. Nevertheless, some patients can suffer from disease relapse which is responsible for a poorer prognosis [37].

ENOCs have heterogeneous molecular profiles characterized by microsatellite instability (MSI, 19% of cases) and mutations and/or expression alterations in KRAS (46%), PIK3CA (39%), PTEN (33%), CTNNB1 (25%), KMT2B (24%), KMT2D (20%), ARID1A (19%), TP53 (17%), PIK3R1 and R2 (11% and 8% respectively), AKT1 (8%), CDKN2A (6%) [36] [38]. These tumors show a mutational burden of 0,17-263 mutations/Mb, which suggests for a ENOC subtype characterized by a hypermutated phenotype. The latter is associated to disfunctions in mismatch / homologous recombination repair pathway and mutations in POLE, a molecular profile that resembles the HGSOC one (**Figure 1.5b**). The distinction between this ENOC subtype and HGSOC is possible considering the lowest mutational burden of the serous carcinoma (0,07-64 mutations/Mb) [36] (**Figure 1.5a**).

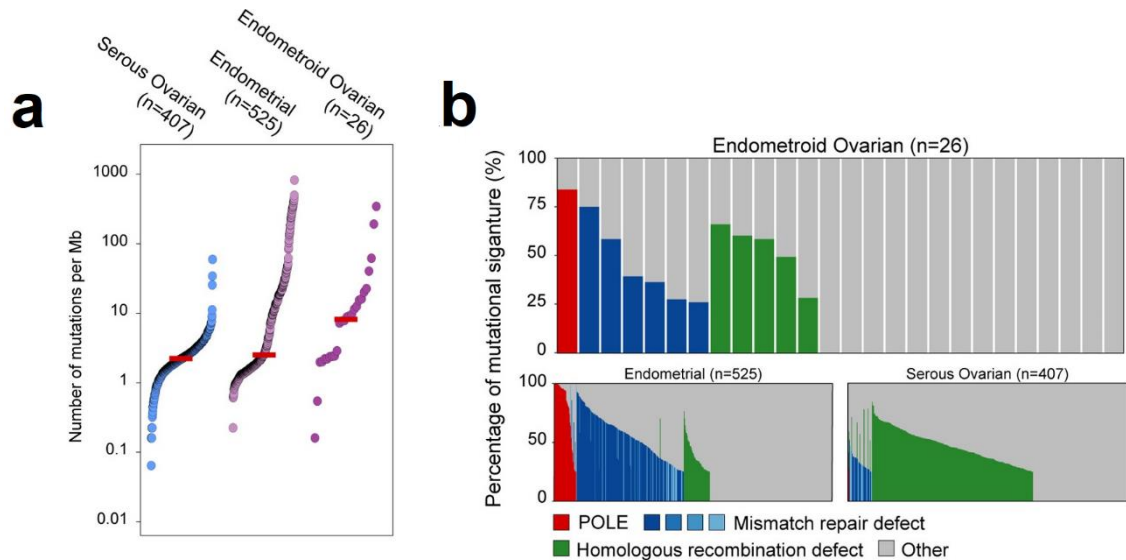


**Figure 1.5:** Comparison between mutational profile of endometrioid ovarian cancer, endometrial cancer and high grade serous ovarian cancer. a) Somatic mutation frequencies observed in exomes. Tumor types are ordered by median mutation frequencies (red lines). Mutation frequencies vary more than 1000-fold within tumor types.; b) Mutational signatures in tumor types. Endometrioid and endometrial cancer show 19% and 10% of samples respectively with Homologous recombination defect. Moreover, they have similar mutation frequencies of POLE (red). Adapted from Pierson [36].

### 1.1.7 Mucinous Ovarian Cancer

The Mucinous Ovarian Cancer (MOC) is a unique EOC subtype with etiology and poorly defined progression mechanisms [39]. Its origin is still uncertain and the debate is focused on its nature of actual ovarian tumor or metastatic disease from other organs [40]. The mucinous benign cystadenomas and mucinous borderline ovarian tumor (MBT) have been suggested as precursor lesions of MOC. Since both of them can be cured by surgery alone, the theory of their ovarian origin (and so of MOC ovarian origin) is more likely than an extra-ovarian one [41].

The molecular profile of MOC is characterized by mutations or copy number loss at *CDKN2A* (76% of cases), mutations at *KRAS* or *TP53* (64% of cases for both), amplification of *ERBB2* (26%) and mutations at *RNF43*, *BRAF*, *PIK3CA* and *ARID1A* (8-12%). These molecular data indicate the MOC as ovarian carcinoma rather than extra-ovarian metastasis: the comparison with molecular profiles of similar tumors (e.g high grade serous ovarian cancer, endometrial, gastric and colorectal tumors, mucinous colorectal tumors) shows indeed marked differences [39] (**Figure 1.6**).

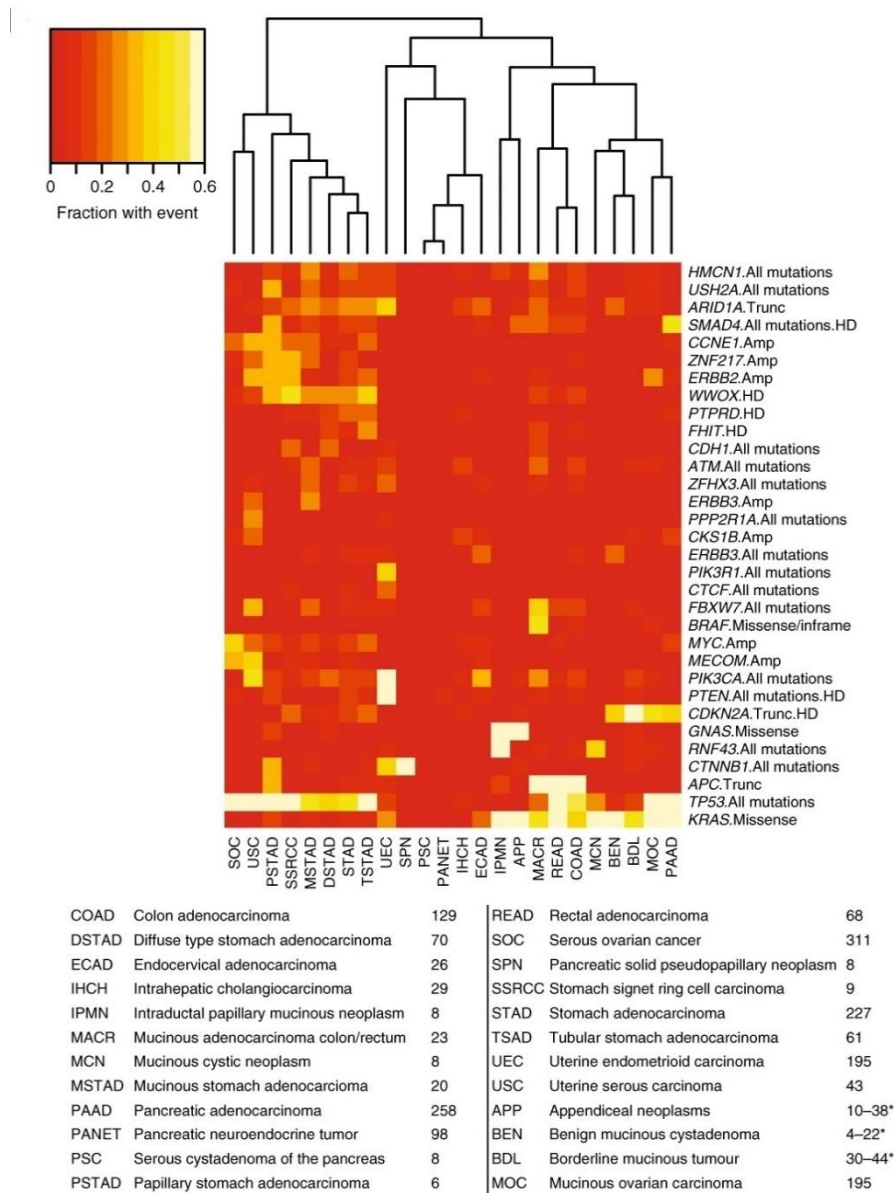


**Figure 1.6:** Comparison of molecular profile (Copy number alterations and mutation frequencies) of MOC and similar tumors. Below is reported the number of samples for each tumor. Adapted from Cheasley [39].

According to the theory of a benign tumor as precursor lesion of MOC, the comparison of molecular profiles of the latter and MBT shows a similar mutation pattern, especially in driver events such as loss of CDKN2A and/or mutations in TP53 and KRAS (around 90% of all MOC cases and 95% of MBT cases) [39]. MOC tumors, especially high-grade ones, have a higher copy number variation rate than MBT tumors, which suggests the increase of copy number alterations as key event in malignance insurgence. The commonest chromosomal aberration in MOCs is the depletion/LOH of 9p and amplification of 9p13, which are associated to poorer clinical outcome [42].

## **1.2 High Grade Serous Ovarian Cancer**

### **1.2.1 Epidemiology and Risk Factors**

The High Grade Serous Ovarian Cancer (HGSOC) is the most common epithelial ovarian cancer (EOC) subtype and accounts for the 70-80% of all ovarian cancer death. The diagnosis generally occurs at a median age of 65 years, mostly in an advanced stage. The HGSOCs limited to the ovary are very rare (<10%), because these tumors have a remarkable inclination to extraovarian dissemination with common and extensive omentum involvement. Interestingly, the size of ovarian tumor is smaller than other EOCs types and the bilateral involvement occurs in around 66% of cases [8].

The HGSOC is characterized by high mortality: the five years survival rate is indeed around 46%. One of the main causes is the late stage diagnosis due to lack of efficient predictive biomarkers and specific symptoms. The diagnosis in advance stages occurs in 75% of cases, which have a five year survival rate of 30%, while early stage diagnosis is rare with 25% of cases, that have a five years survival rate of around 92% [43].

The most important risk factor is a strong family history of breast and/or ovarian cancer. Hereditary HGOSCs are, indeed, mainly correlated at inherited mutation in BRCA1 and BRCA2 (women with germline mutation in these genes have a lifetime risk of 44% and 10% respectively). Other possible risk factors have been proposed (e.g. lifetime ovulations, oral contraceptives, smoking, obesity etc.), but their validity must yet be proved [44].

### **1.2.2 Carcinogenesis**

The carcinogenesis and tumoral progression of HGSOC are widely studied and debated topics, but, still now, they are not completely understood.

Currently, two main theories try to establish a coherent model for the carcinogenesis of HGSOC. The first and oldest one indicates the ovarian surface epithelium (OSE) as the site of origin for HGSOC insurgence. The OSE cells are exposed during normal ovulation at a prooxidative and proinflammatory environment that induces DNA

damages. According to this model, some altered OSE cells can invaginate and form cortical inclusion cysts (CICs) in underlying stroma. Under the effects of ovarian hormones, the CICs mesothelial cells can differentiate in Müller epithelial cells (metaplasia) and then progress to a malignant state [45].

The second theory, most widely accepted nowadays, proposes the fallopian tube as origin site of HGSOC. Accordingly, the fallopian tube secretory serous epithelial cells (FTSEC), after oxidative or inflammatory genotoxic stress, undergo malignant transformation and clonal expansion that progress to a precursor lesion called serous tubal intraepithelial carcinoma (STIC). Probably, a starting mutational event of TP53 in FTSECs leads to a sensitive-DNA damage state that promotes the subsequent tumorigenic molecular alterations (like BRCA loss that further increases the chromosomal instability and so the copy number variations rate) [8]. However, these malignant cells can exfoliate from fimbriated ends of fallopian tube to peritoneal surface or near ovaries inducing the HGSOC insurgence [46] [47] (**Figure 1.7**).

There are some evidences supporting this theory such as the presence of a STIC lesion in 50-60% of sporadic tumors and in 80% of hereditary tumors with germline BRCA mutations [48]. Moreover, some studies have highlighted similar mutation of TP53 in some serous ovarian tumors and correlated to STICs. Furthermore, the expression of PAX8 (a Müller epithelium marker), but not of calretinin (a mesothelium marker) has been detected by immunohistochemistry in serous ovarian cancers [47]. The correlation between tumorigenic mutations and a proinflammatory-prooxidative environment induced by ovulation indicates that the number of lifetime ovulations (absence of pregnancy, early age of menarche and late age at menopause) can be used as possible risk factor [49].

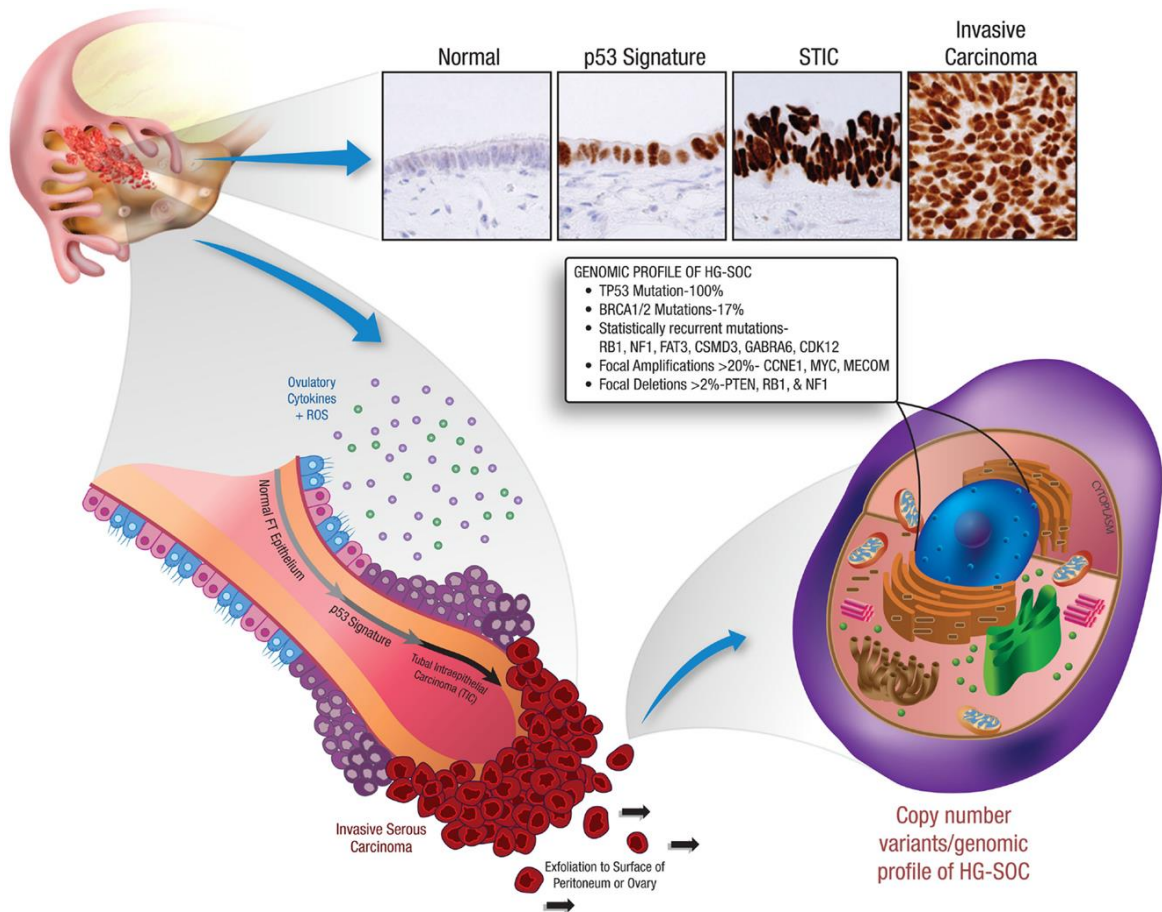


**Figure 1.7:** Sequence of principal carcinogenesis events of HGSOE according to the "fallopian tube" model. Moreover, in figure are reported the results of immunohistochemical staining for TP53 in each step of tumor progression and the molecular profile of HGSOE cells [166].

### 1.2.3 Morphological Features

HGSOEs are heterogeneous tumors characterized by different morphological patterns and tissue architectures that can also coexist in the same tumoral mass.

From a cytologic point of view, the HGSOE cells are often pleomorphic (different size), multinucleated and characterized by the presence of psammoma bodies (concentric calcium deposits associated to papillary growth pattern). Moreover, they have a great nuclear atypia, large hyperchromic nuclei, nuclear pleomorphism and large eosinophilic nucleoli (typical characteristics of tumors with high mitotic index) [50].

The HGSOEs can show different tissue architectures: solid, transitional, cribriform/pseudo-endometrioid, papillary, classic and compressed micropapillary, infiltrative papillary and infiltrative micropapillary [51]. According to these

morphological architectures, to the invasion behavior and to the presence of BRCA mutations, HGSOCs can be grouped in two main groups (**Table 1.1**):

- Classic HGSOCs including tumors with papillary and micropapillary patterns. Papillary tumors show a finger-like connective axis surrounded by tumoral cells. Micropapillary tumors instead show clusters of tumor cells without a vascular core [51]. These tumors show BRCA mutation in 28% of cases, lag between STIC lesion and symptomatic disease insurgence (in women without BRCA mutations), higher median age of diagnosis, low responsiveness to chemotherapy, PARPs inhibition and poor outcome [52].
- SET HGSOCs including solid, endometrioid-like and transitional tumors. Solid tumors show cells arranged in sheet, endometrioid-like tumors have instead cells that grow in a glandular and nested pattern, while transitional tumors are characterized by thick and stratified layers. SET HGSOCs are characterized by more tumor infiltrating lymphocytes (TILs), necrosis and higher mitotic index than classic ones. Moreover, they are mutated at BRCA genes in about 50% of cases, and they are also associated to a rapid growth after the tumorigenic lesion (in patients with BRCA mutations), young age of occurrence, good response to therapy and good outcome [52] (**Figure 1.8**).

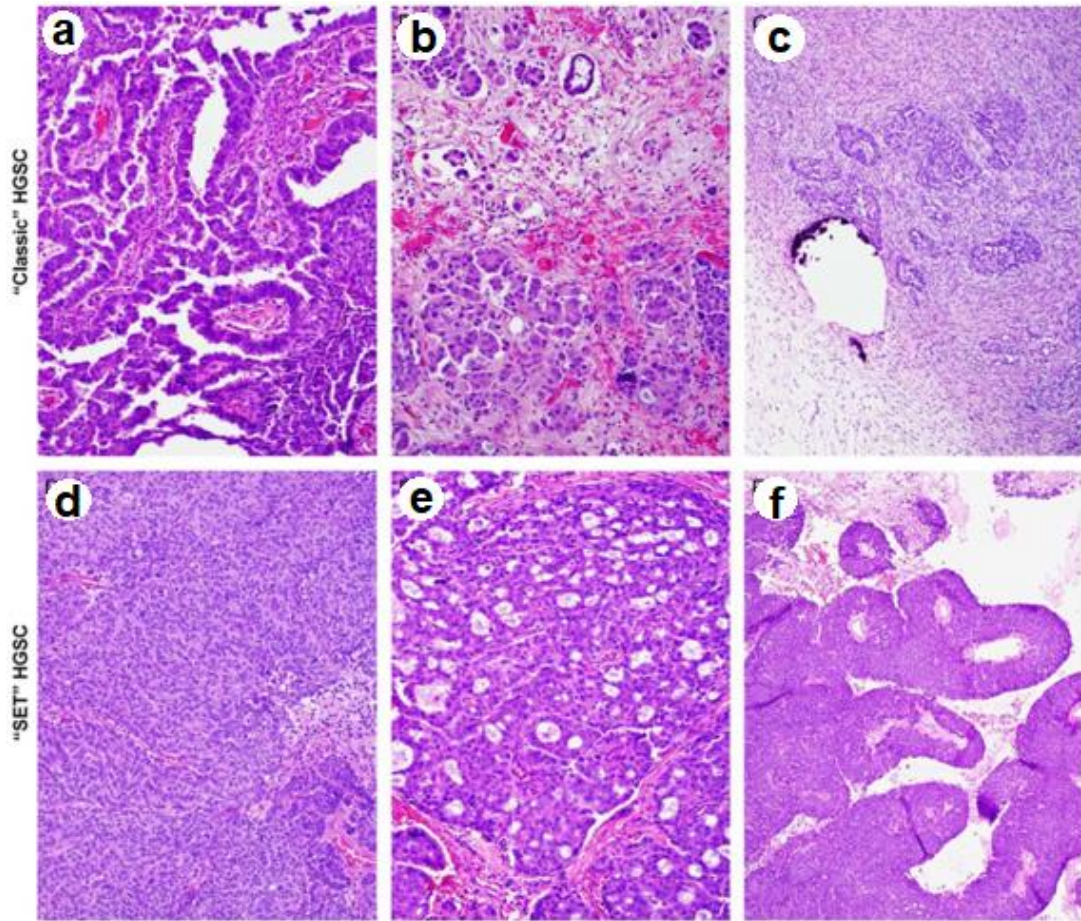


**Figure 1.8:** Morphological patterns of HGSC: a) papillary; b) micropapillary; c) infiltrative; d) solid; e) pseudoendometrioid; f) transitional; g) summary of dualistic model of HGSC [52].

	“SET”	Classic
Histologic pattern	Solid, endometrioid, transitional	Solid growth with slit-like glandular lumens
Age	Younger	Older
STIC	23%	67%
BRCA mutation	50%	28%
Behavior	Rapidly growing	Lag phase from STIC to symptomatic metastatic tumor
Response to chemotherapy and PARP inhibitors	More responsive	Less responsive

**Table 1.1:** Principal features of the two morphological groups of HGSC: SET and Classic [52].

## 1.2.4 Molecular Features

In 2011, the Cancer Genome Atlas (TCGA) has provided an overview of molecular profile of HGSOC by whole genome sequencing (WGS) of 489 cases [15]. The results of this study have showed a low mutation rate and a multitude of genomic structural variants which indicate HGSOC as an extremely heterogenous tumor characterized by high chromosomal instability.

The only gene with a significant mutational frequency in HGSOC is TP53, which is mutated in 96% of the cases. Around 80% of these mutations occur in the exons coding the DNA binding domain and cause loss of function inherent to transcriptional activity of TP53. Sometimes the mutations can cause a gain of function that makes TP53 a promoter of invasiveness, drug resistance and cellular proliferation [53].

The other genes with a significant mutation rate are BRCA1 and BRCA2 which are mutated respectively in 12.5% and 11.5% of the cases. Moreover, around 11% of patients present an inactivation to BRCA1 due to gene hypermethylation. Besides these genes, HGSOCs show alteration in other genes involved in the DNA repair mechanism such as RAD50, RAD51, RAD51C (genes from RAD core, mutated in 1.5% of all cases) CDK12 (3%), FA genes (mainly PALB2, FANCA, FANCI, FANCC for a total of 2%), ATM, ATR, CHECK1 and CHECK2 (genes involved in DNA damage response, mutated in 2% of cases) [15]. According to presence of alterations in homologous recombination DNA repair system (HRR, where are involved BRCA1 and BRCA2) it is possible to divide HGSOCs in two groups [54]:

- HRR deficient: accounting for 51% of all HGSOC and showing alterations in different components of DNA repair mechanism.
- HRR proficient: characterized by amplification of CCNE1 in 15-20% of cases. This alteration is mutually exclusive with BRCA mutations and it is often correlated to activation of AKT pathway [55]. These tumors show a worst chemotherapy response and outcome than HRR deficient ones (**Figure 1.9**).

Other molecular hallmarks of HGSOCs include alterations of different pathway, such as RB pathway (CDKN2A, CCNE1, CCND1, CCND2, RB1), PIK3CA/RAS pathway (PTEN, PIK3CA, AKT1, AKT2, NF1, KRAS, BRAF) and NOTCH pathway (JAG1, JAG2, MAML1, MAML2, MAML3, NOTCH3) [15].

Moreover, the results of the TCGA study have highlighted a higher rate of copy number variation that involves mainly the amplification of MYC, MECOM and CCNE1 in around 20% of HGSOCs and depletion of PTEN, RB1 or NF1 [15].

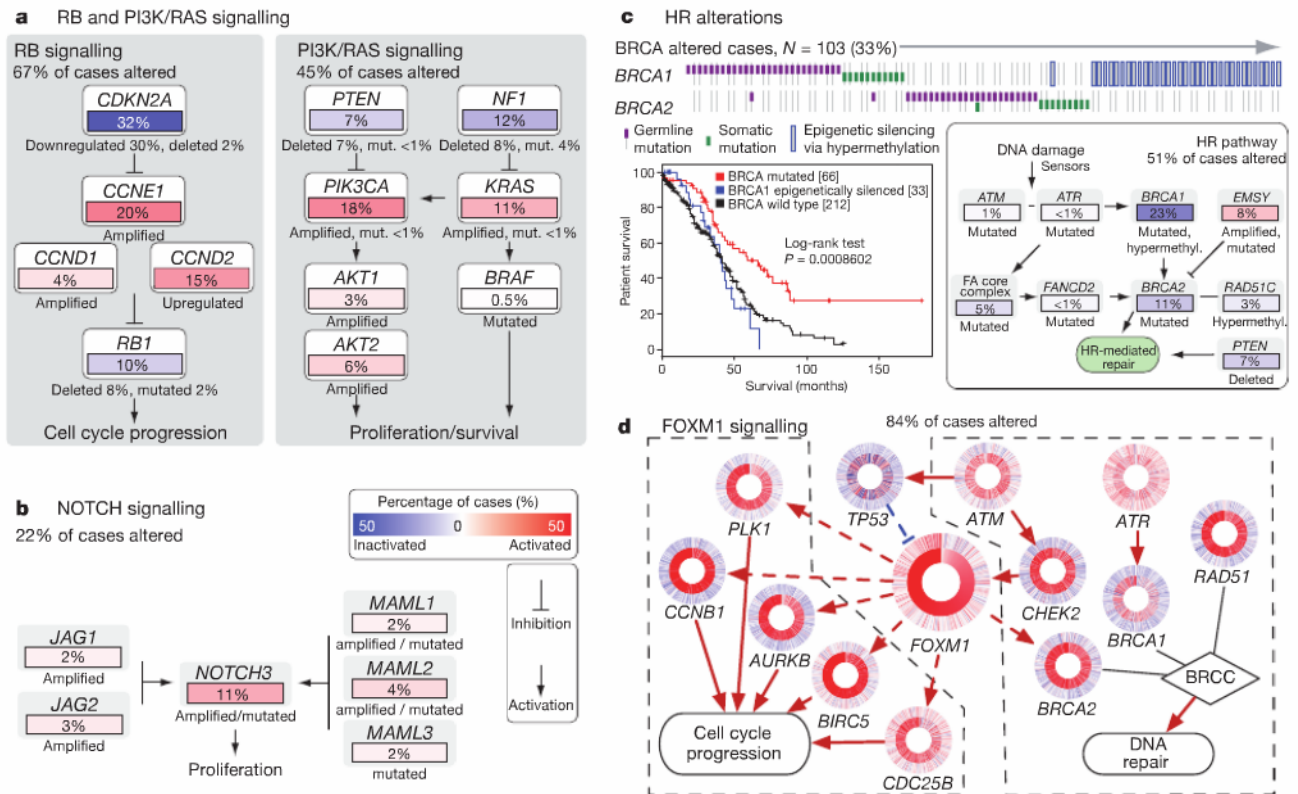


**Figure 1.9:** Pattern of genetic alterations in HGSOCs concerning the RB and RAS/PI3K pathway a); Notch pathway b); HR pathway c) and FOXM1 pathway d). Moreover, in panel c is reported the survival analysis of patients with different BRCA status (wildtype, epigenetically silenced and mutated). In panel d each gene is surrounded by an outer ring and an inner ring which indicate respectively the copy number and gene expression. Each line generating the rings represents a single patient sample. Rings are sorted in increasing order of FOXM1 expression. Dashed lines indicate transcriptional regulation [29].

## 1.3 Prognosis and Treatment of Ovarian Cancer

### 1.3.1 Prognosis

The Ovarian cancers (OCs) are a group of tumors characterized by high heterogeneity and complexity, as reported above. This hinders a clear interpretation of anatomopathological prognostic factors. Usually, the evaluation of OC patients prognosis is performed using three parameters:

- Histologic type and malignance grade of the disease.

- Volume of the residual tumoral mass after surgery.
- Tumoral stage at first diagnosis. This evaluation is performed according to the International Federation of Gynecology and Obstetrics (FIGO) staging system. The latter is based on the extension of tumoral mass (a parameter that indicates if the tumor is confined to the ovary or if it involves other neighboring organs), on lymphocytic infiltration and on the presence of metastasis [56] (**Table 1.2**).

FIGO stage	Description	Corresponding TNM stage
I	Tumour confined to ovaries or fallopian tubes	T1
IA	Tumour limited to one ovary (with ovarian capsule intact) or fallopian tube; no tumour on ovarian or fallopian tube surface; no malignant cells in the ascites or peritoneal washings	T1a
IB	Tumour limited to both ovaries (with ovarian capsules intact) or fallopian tubes; no tumour on ovarian or fallopian tube surface; no malignant cells in the ascites or peritoneal washings	T1b
IC	Tumour limited to one or both ovaries or fallopian tubes, with any of the following C substages: <ul style="list-style-type: none"> <li>• IC1: surgical spill intraoperatively</li> <li>• IC2: capsule ruptured before surgery or tumour on ovarian or fallopian tube surface</li> <li>• IC3: malignant cells in the ascites or peritoneal washings</li> </ul>	T1c
II	Tumour involves one or both ovaries, or the fallopian tubes with pelvic extension below the pelvic brim or primary peritoneal cancer (Tp)	T2
IIA	Extension and/or implants of tumour on uterus and/or fallopian tubes and/or ovaries	T2a
IIB	Extension of tumour to other pelvic intraperitoneal tissues	T2b
III	Tumour involves one or both ovaries, or the fallopian tubes, or primary peritoneal cancer with cytologically or histologically confirmed spread to the peritoneum outside the pelvis and/or metastasis to the retroperitoneal lymph nodes	T3
IIIA	Metastasis to the retroperitoneal lymph nodes with or without microscopic peritoneal involvement beyond the pelvis	T1, T2, T3aN1
	IIIA1: positive retroperitoneal lymph nodes only (pathologically proven)	
	• IIIA1(i): metastasis up to 10 mm in greatest dimension	T3a/T3aN1
	• IIIA1(ii): metastasis >10 mm in greatest dimension	
	IIIA2: microscopic extrapelvic (above the pelvic brim) peritoneal involvement with or without positive retroperitoneal lymph nodes	T3a/T3aN1
IIIB	Macroscopic peritoneal metastasis beyond the pelvis up to 2 cm in greatest dimension, with or without metastasis to the retroperitoneal lymph nodes	T3b/T3bN1
IIIC	Macroscopic peritoneal metastasis beyond the pelvis >2 cm in greatest dimension, with or without metastasis to the retroperitoneal lymph nodes (includes extension of tumour to capsule of liver and spleen without parenchymal involvement of either organ)	T3c/T3cN1
IV	Distant metastasis excluding peritoneal metastases	
	• IVA: pleural effusion with positive cytology	Any T, any N or M1
	• IVB: parenchymal metastases and metastases to extra-abdominal organs (including inguinal lymph nodes and lymph nodes outside of the abdominal cavity)	

**Table 1.2:** FIGO Staging system. TNM: TNM classification of malignant tumors [167].

According with FIGO system we can identify three groups of patients with different relapse risk in early stage: low risk (stage IA-IB grade 1), intermediate risk (stage IA-IB grade 2 and stage IC grade 1), high risk (stage IA-IB grade 3, stage IC grade 2-3, all stage II) [57].

### 1.3.2 Ovarian Cancer Treatments

Despite the advances in knowledge of ovarian cancer and its histological variants, which point out the need of different approach treatment for each subtype, the basic therapy of this tumor has remained almost the same in the last 40 years. The latter is based on a debulking surgery followed by an adjuvant chemotherapy with alkylating agents such as platinum analogs (e.g. cis-platinum and carbon platinum).

The aims of surgery are the complete macroscopic resection of the tumoral mass and the assessment of the tumor stage. An efficient debulking surgery is one of the most favorable prognostic factors for survival [58]. The surgery is based on a radical hysterectomy and a bilateral salpingo-oophorectomy, peritoneal surface examination and harvesting of ascitic fluids.

The adjuvant chemotherapy is performed after surgery in order to prevent possible recurrences. This step is required especially for patients with advanced stage disease (stage III or IV) or at early stage but with high risk of relapse (stage IA-IB grade 3, stage IC grade 2-3, all stage II). Women with diagnosis at early stage and with low or intermediate risk of recurrence (IA-IB grade 1-2 and stage IC grade 1) have a five-years survival rate of 90-95% after surgery and for this reason they don't need adjuvant chemotherapy [59].

The first agents used in adjuvant chemotherapy of OCs were platinum analogs, a class of molecules with an antineoplastic effect. These molecules are able to intercalate the DNA double strands binding the alkyl group on guanine. This leads to different DNA damage and subsequently to cellular apoptosis [60]. For this reason, the platinum-based treatment is particularly effective against tumors with deficient DNA repair mechanisms, such as HGSOC.

An improvement of this therapeutic approach is based on the use of a combination of antitumoral drugs with synergistic effects. A typical example of polychemotherapy in OC is the carboplatin-paclitaxel treatment. The paclitaxel is an antitumoral agent which induces mitotic arrest (and so cellular apoptosis) binding the beta-tubulin monomers altering the depolymerization/polymerization equilibrium of cellular microtubules [61].

Despite the advances provided by platinum analogous use in first line treatments, this chemotherapy is extremely debilitating and it is characterized by a remarkable percentage of recurrence within two years after treatment. The relapses are almost

resistant to first line treatment and so there is the need of a different second line therapeutic approach.

For this reason, the development of new therapeutic treatments targeting specific molecular markers and overcoming the side effects of typical chemotherapy drugs is a key point. The use of PARP inhibitors (PARPi) is an example of promising target therapy. These drugs inhibit the PARP enzymes, a class of proteins involved in reparation of single strand DNA breaks. Since double strand DNA breaks are repaired by homologous recombination repair pathway (HRR), tumors characterized by dysfunction in this pathway (e.g. HGSOc with BRCA mutations) are sensitive to PARPs inhibition. The latter, indeed, causes the accumulation of single strand DNA breaks, collapse of replication fork and accumulation of double strand breaks which can't be repaired by the altered HRR mechanism. This leads to accumulation of DNA damages and so to cellular death [62].

## **1.4 Biomechanics and Atomic Force Microscope**

### **1.4.1 Role of Mechanical Features in Biological Specimens**

The rheology is a branch of physics which deals with the deformation of materials in response to a force application on them. Since this response is related to the macroscopic structure of materials, the principal aim of rheology is to develop mathematical models able to correlate the stress response of materials to their structural features [63].

From a rheologic point of view, the biological specimens (e.g. tissue, cells, extra-cellular matrix) show a viscoelastic behavior. The latter is characteristic of materials that have both an elastic and a viscous component and so show a stress response intermediate between materials closely elastic and purely viscous.

Since biological specimens are in a physical environment where they are subjected to different mechanical stresses, the comprehension of the role played by the mechanical forces in basic life processes is paramount.

Despite the complexity and heterogeneity of biological specimens (characterized by different components with different mechanical properties), many studies have improved the knowledge on their mechanics. For example, it has been proved that the stiffness of a matrix influences the differentiation of mesenchymal stem cells

(MSCs). If these cells are on a rigid matrix that mimics collagen bones (25-40 kPa), they differentiate into skeletal-like polygonal cells; on a matrix with stiffness similar to muscles (8-17 kPa), MSCs transform into muscle-like spindle cells and finally on soft matrix that mimics the stiffness of brain tissues (0.1-1 kPa) they assume a nerve-like branched morphology [64] (**Figure 1.10**).

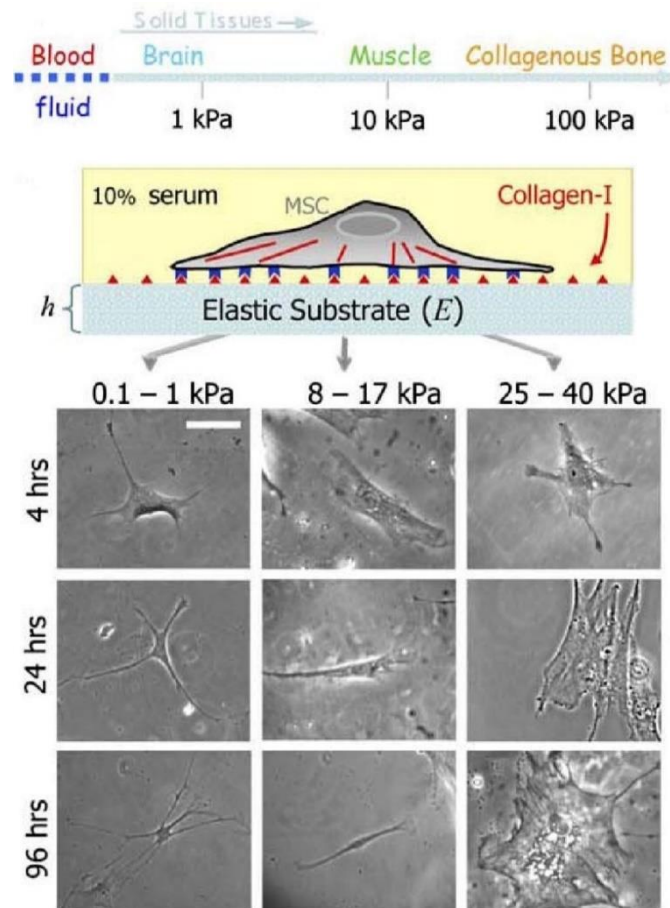


**Figure 1.10:** Differentiation of naïve MSCs on substrates with different stiffness. They can assume a neuron-like branched morphology (first column), a muscle-like spindle morphology (second column) or a skeleton-like polygonal morphology. Adapted from Engler [64].

The first cellular structure involved in the determination of the cellular mechanical features is the cytoskeleton. This is an extremely dynamic molecular network (mainly composed by actin, microtubule and intermediate filaments) that is involved in different cellular processes (organelle transport, determination of cell shape, movement, differentiation and signaling) [65]. Changes in cytoskeleton homeostasis are fundamental, for example, in different tumoral processes like uncontrolled proliferation, invasion and metastasis. It has been proved that tumoral cells are softer than the corresponding healthy ones [66], due probably to their higher proliferation rate. Cells in mitotic interphase, indeed, show a widespread distribution of actin

monomers in the cytoplasm instead of the typical well organized actin network of non-mitotic cells [67].

Moreover, tumoral cells with overexpression of vimentin and keratins (two components of intermediate filaments) have a higher stiffness and aggressiveness [68]. The cell stiffening is, indeed, an important step which allows the tumoral mass to expand against a rigid tissue matrix and so to invade the surrounding tissues [69]. Changes in cytoskeleton organization are involved also in the metastatic process. The cellular softening, for example, can improve the lamellipodial movement velocity of malignant fibroblast [70], while a depolymerization of cortical actin network can allow the microtubule filaments penetration and so the formation of micro-tentacles which are involved in the metastatic process of blood circulating breast tumor cells [71].

### **1.4.2 Atomic Force Microscope**

The mechanical characterization of biological specimens can be performed by using different tools, such as the atomic force microscope (AFM). The AFM is a scanning probe microscope (SPM) invented by Binnig, Quate and Gerber in 1986. Like other SPM, AFM is an instrument based on the use of a mechanical probe (a microlever called cantilever) which comes into contact with the sample and of a piezoelectric element that allows accurate and precise movements of the cantilever in the three spatial dimensions: x, y and z. The interaction between the sample and the cantilever leads to a deflection of the latter. The deflection is recorded by a laser beam pointed on the cantilever and then deflected on a photodiode, which acts as detector system (**Figure 1.11**). The deflection of the cantilever is determined by attractive and repulsive forces which occur when the microlever and the sample comes into contact. These forces are associated to the mechanical and molecular features of the sample and, for this reason, the cantilever deflection can be used to analyze them.

The AFM has a resolution in the order of nanometer (more than 1 000 times better of optical diffraction limit) and can apply and record forces in the order of 1 pN – 100 nN [72]. The high versatility and resolution of AFM make it a useful tool for different purposes (e.g. force measurement, topographic imaging, molecular manipulation). The AFM can be used for example to acquire high-resolution images of different materials. In imaging-mode, the sample is scanned by the cantilever which is deflected according to the topographic profile of the sample surface. The resulting

image is highly detailed and can provide information on the tridimensional features of the sample.

Another useful and versatile AFM mode is the force spectroscopy (FS), where the achieved forces are analyzed in function of the probe distance from the sample. In FS, the cantilever is initially brought into contact with the sample and then it is pulled toward its. This leads to the generation of a force-displacement curve characterized by the initial approach curve (associated to the first contact between the sample and cantilever) and the subsequent retract curve (inherent to retraction of cantilever). These curves provide information on mechanical and adhesion properties of the sample (from the approach curve and the retract curve respectively) (**Figure 1.11**). Moreover, by functionalizing the cantilever with different molecules (e.g. antibodies, receptors or DNA filaments) it is possible to analyze their interactions with other molecules on a substrate (e.g. antigens, ligands or complementary DNA filaments).

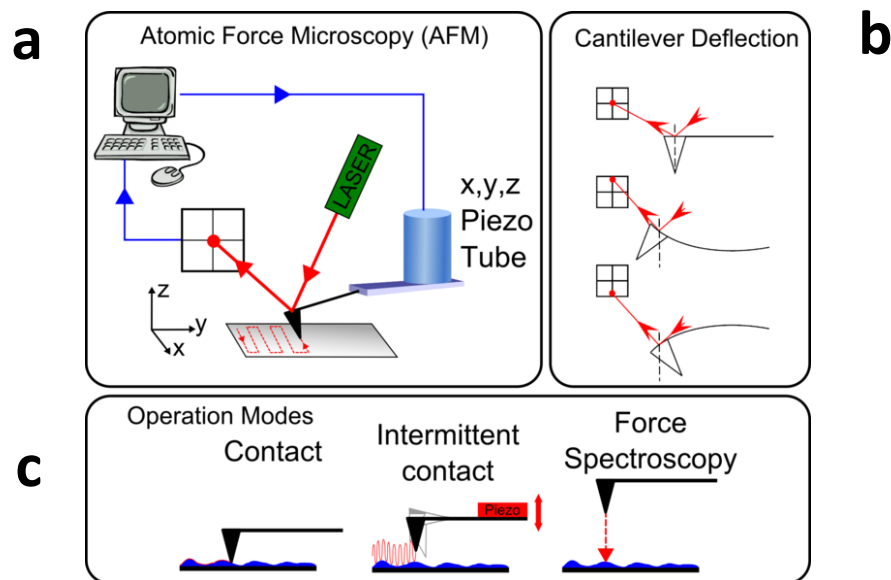


**Figure 1.11:** Scheme of AFM components (a), working principle (b) and modes (c). Contact and intermittent mode are two different AFM approaches to scan the sample. The contact mode provides images with higher resolution than intermittent mode but can damage the sample. For this reason, in imaging of biological samples it is better to use the intermittent mode [168].

### 1.4.3 Application of Atomic Force Microscope in Biology

Although the initial aim of AFM was the study of materials, in the last decades this instrument has widely been used in biomedicine and biology due to its high resolution and the possibility to work in physiological fluids (and so on living biological specimens).

For example, the AFM was used to obtain images of different virus morphologies, such as Tobacco virus [73] or HIV [74]. Viruses have very small size (20-400 nm) which is lower than the resolution limit of an optical microscope. Consequently, the AFM, with its high resolving power and poorly destructive effect on sample preparation, is a good choice in the analysis of viral morphologies. Moreover, the AFM has been also used to analyze some physiological processes involved in virus pathogenicity, such as the self-assembly of core proteins in HIV and Mason-Pfizer monkey viruses [75] or the formation of lipidic raft microdomains induced in infected cells by replication complex of the hepatitis C virus [76].

AFM is also used in the analysis of bacteria and their morphological properties. It was used for example to analyze the surface changes of *Streptomyces coelicolor* during the different steps of its life cycle [77] or to observe the structure of bacterial annexes like cilia or flagella [78]. The AFM can be used also to analyze the morphological changes of bacteria after the treatment with antibiotics [79] or antimicrobial peptides [80] in order to improve the comprehension of the physiological processes that underline the antibiotic resistance.

As concern eukaryotic specimens instead, AFM studies was mainly focused on morphology and mechanical properties of tumor cells. This instrument was used to analyze the morphological changes of tumoral cells induced by chemotherapy drugs. The treatment with paclitaxel, for instance, determines a higher superficial roughness and softness of HeLa cells [81]. In 2012, Plodinec and colleagues have demonstrated that invasive tumoral tissues were softer than the corresponding benign and healthy counterparts. Malignant tissues have also shown a broad range of stiffness distribution (due probably to tissue heterogeneity) with a main low stiffness peak associated to invasive cells [82] (**Figure 1.12**).

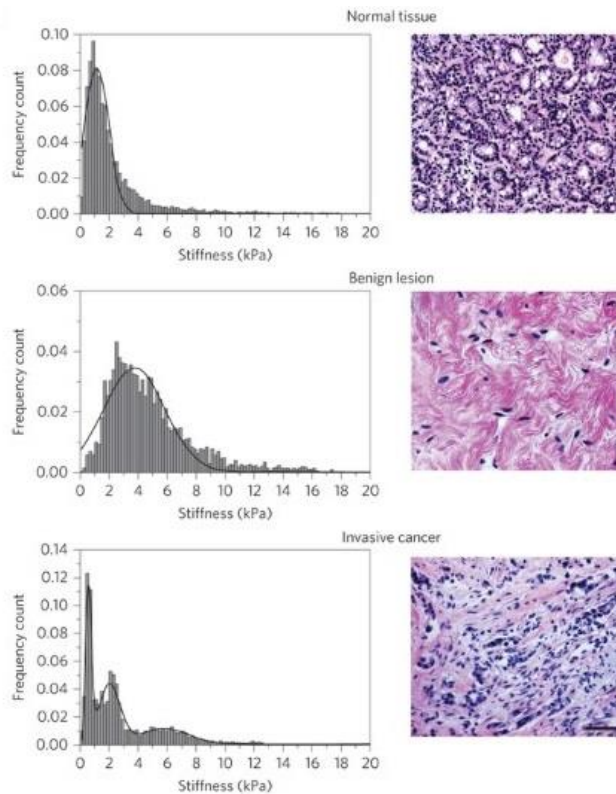


**Figure 1.12:** The left column shows the stiffness distribution of a normal mammary gland tissue, a benign breast lesion and an invasive breast carcinoma (from top to bottom). In the right column are reported the H&E-stained sections of the analyzed samples. Adapted from Plodinec [82].

The AFM represents a good tool to analyze phenomena at the molecular scale, such as molecular interactions. In this experimental setting, the cantilever is functionalized with a molecule and then it is brought into contact with a possible ligand placed on a substrate. After the bond formation between the two molecules, the cantilever is retracted in order to observe the force required to break the bond. This kind of analysis was performed to observe the bond strength between avidin and biotin [83]. The resolving power of AFM is high enough to observe the conformational changes of proteins. An example of these studies refers to OmpF, the most common porine in outer membrane of Gram negative. The porins are proteins that cross the cellular membrane and act as a pore, through which molecules can diffuse. In 1999, Muller and Engel have demonstrated by AFM imaging that voltage changes caused conformational variations of OmpF and so the opening or closing state of the channel [84].

Like proteins, also nucleic acids were submitted to several AFM studies. This instrument can be used to obtain high-resolution images of chromosome marked with the standard method of Giemsa-trypsin-Giemsa. These images have a higher resolution of chromosome banding than the electronic microscope making AFM a

good alternative for the construction of a karyotype and for the observation of possible structural alterations [85] (**Figure 1.13**).

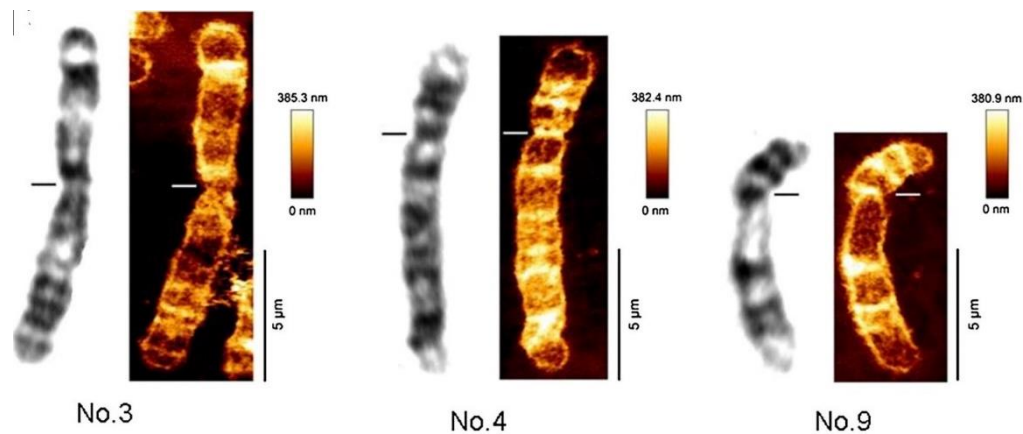


**Figure 1.13:** Comparison between electronic microscopic imaging and AFM imaging of Giemsa-trypsin-Giemsa treated chromosome. Adapted from Chang [85].

## 1.5 The Ubiquitin-Proteasome System

### 1.5.1 Proteolysis

The proteostasis is a fundamental network of competitive and integrated biological pathway the aim of which is the dynamic regulation of a balanced and functional proteome. These pathways are involved in biogenesis, folding, trafficking and degradation of proteins within cells. The proteostasis is essential to ensure a proper cellular function. The proteolysis, for example, is involved in the disruption of misfolded or aberrant proteins, the accumulation of which can be toxic for cells [86]. Wild-type proteins also need to be degraded after having accomplished their function or when they are involved in pathway where a rapid protein turnover is required. For this reason, the protein degradation pathway is essential for different cellular processes (e.g. proliferation, differentiation, stress response, DNA repair, transcriptional regulation) [87].

Eukaryotic cells have different proteolytic systems, the most important of which are the lysosome pathway and the proteasome-ubiquitin system (UPS). The latter is a cellular pathway which mediates a highly specific protein degradation. Unneeded or damaged proteins undergo a post-translational modification, where the ubiquitin, a

protein with low molecular weight, is covalently bound. This linkage marks the altered protein and drives it to the proteasome where it is degraded [88].

Disfunctions in UPS can lead to different pathological states, which include tumors and genetic or neurodegenerative diseases [89] [90].

### **1.5.2 Ubiquitination**

The first step in ubiquitin-proteasome degradation pathway is the binding of the ubiquitin to the protein to degrade. The ubiquitin (Ub) is a highly conserved protein of 76 amino acids with a total molecular weight of 8.6 kDa [91]. The covalent bond with target proteins occurs between the carboxyl group of ubiquitin's terminal glycine and the  $\epsilon$  amino-group of the substrate's lysine. Afterwards, other ubiquitins are added (at least four) to form a polymeric tail which directs the protein to proteasome-mediated degradation. The covalent bond with the substrate is reversible and allow the ubiquitins to be released during the protein degradation process and, so, to be used in other marking cycles [92].

It is important to stress that the monoubiquitination is involved, over the proteolysis, in other cellular processes, such as protein translocation, pathway activation and DNA damages signaling [93].

### **1.5.3 Proteasome**

The proteasome is a multicatalytic protein complex with high molecular weight (2,5 MDa and sedimentation coefficient of 26S), involved in the degradation of proteins marked by ubiquitin. It is characterized by two different functional compartments: the catalytic core 20S (or Core Particle, CP) and the two regulatory subunits 19S (or Regulatory Particle, RP). The CP is able to degrade unfolded and aberrant proteins by itself, but it can also catalyze the degradation of wildtype proteins associating with the two RPs, which are made up by two compartments, base and lid, composed by 19 subunits with different sizes (24-106 kDa). These two compartments are linked by subunit Rpn10, which additionally acts as a structure stabilizer. The base is composed by nine subunits and is involved in the direct link with the CP. The lid, instead, is composed by 10 subunits and is essential to recognize the polyubiquitin tail. Moreover, the subunit Rpn11 is a deubiquitinating enzyme of the JAMM/MPN

domain-associated metallopeptidases family and is involved in the removal of polyubiquitin tail from substrates [94] (**Figure 1.14**).

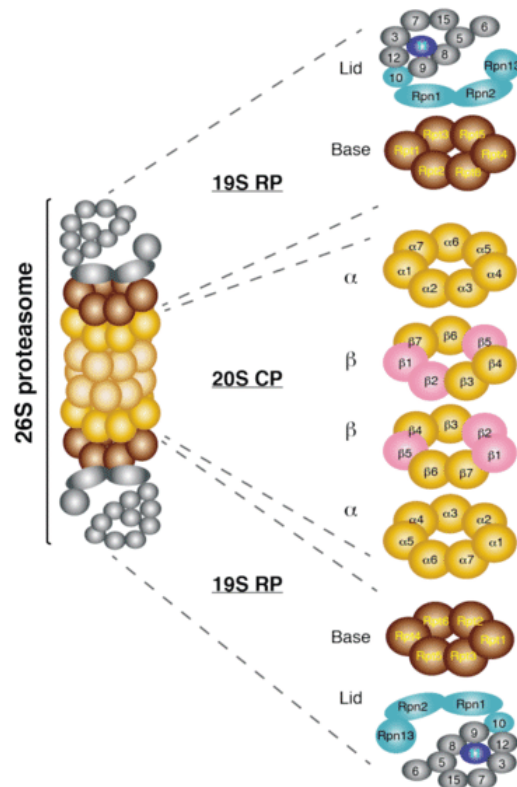


**Figure 1.14:** Schematic diagram depicting the proteasome 26S, the two compartments CP 20S and RP 19S and their subunits. Adapted from Turakhiya [169].

### 1.5.4 Deubiquitination

An important feature of the ubiquitin-proteasome system is the reversibility of ubiquitin-target protein link, which allows recycling the ubiquitin monomers for new proteins to degrade. The hydrolysis of the iso-peptide bond between the carboxyl group of ubiquitin's terminal glycine and the  $\epsilon$  amino-group of a target protein's lysine is catalyzed by deubiquitinating enzymes (DUBs), a class of cysteine proteases and metalloproteases [95]. Over the standard function, the DUBs are involved in the removal of ubiquitins from erroneously marked proteins and in modulation of the signal carried from the polyubiquitin tail [96].

The DUBs are involved in many cellular processes due to their precise control on the activity, location and stability of proteins. For this reason, mutations/deregulations of these enzymes can be recognized in different diseases, including tumors. The

overexpression of USP18, an isopeptidase, has been found to limit the apoptotic susceptibility of tumors to IFN- $\alpha$  or bortezomib treatment [97].

### **1.5.5 Inhibitors of Ubiquitin-Proteasome System for Tumor Treatment**

Despite the high potential of ubiquitin-proteasome system inhibitors (iUPSs) in tumors treatment, their use has remained limited due to their poor specificity and stability. For this reason, the efforts to develop new efficient iUPSs are focusing on the improvement of their selectivity.

The first iUPSs developed are called first-generation inhibitors. They are small natural or synthetic peptides with a functional group able to undergo a nucleophilic attack to a hydroxyl group on the proteasome's active site. This leads to the inactivation of the protein complex and consequently of the entire pathway. The most important first-generation inhibitor is the Bortezomid, a dipeptide with a modified leucine, carrying a boronic acid in substitution of the carboxylic group. It was approved for clinical use in 2003 [98]. The Bortezomid binds, and reversibly inhibits, the  $\beta 5$  subunits of proteasome 20S with high affinity and specificity. This leads to an intracellular accumulation of unfolded or misfolded proteins (especially immunoglobulins) with subsequent cell cycle arrest and activation of apoptosis.

The Bortezomid is used to treat different neoplasms, such as multiple myeloma and mantle cell lymphoma [99]. However, its serious side effects (including peripheral neuropathy, heart failure, neutropenia and thrombocytopenia) have highlighted the need of more efficient iUPSs [100].

The second-generation inhibitors are focused on other components of UPS, like the E1, E2 and E3 enzymes or the DUBs. Their inhibition, in particular, have many consequences: intracellular accumulation of protein-ubiquitin complexes and unfolded/damaged proteins, diminution in availability of ubiquitin monomers and proteotoxic stress. Some efforts have indicated that malignant cells are extremely dependent from functioning UPS due to their high proliferation rate and high amount of aberrant proteins. This makes the tumoral cells more sensitive to inhibitor of DUBs (iDUBs) than healthy ones [101].

According to their selectivity, it is possible to distinguish two different classes of iDUBs:

- Selective inhibitors: They act on DUBs and for this reason have a high therapeutic potential for tumors characterized by alteration in specific isopeptidases. An example is the RA-9 drug, a specific inhibitor of DUBs associated to the regulatory particles 19S of the proteasome 26S. Its effectiveness in ovarian cancer treatment was proved on both cell lines and murine models [102].
- Non-selective inhibitors (N-SIIs): They act on different isopeptidases and cellular pathway, which make them usable for several tumors. A promising class of N-SIIs includes drugs containing a  $\alpha$ - $\beta$  unsaturated di-enone cross-conjugated with two electrophilic carbons [103]. They act as Michael acceptors for the free thiol groups of cysteines on the DUBs's active sites. This leads to the formation of an irreversible bond which inactivates the proteases [104]. However, these inhibitors can interact with other molecules over the DUBs, and so, the presence of these competitor molecules can reduce the cytotoxic effects induced by N-SIIs. Glutathione (GSH) is an example of molecule with high affinity to N-SIIs. It has been shown, indeed, that glioblastoma cell lines previously treated with agents able to reduce the GSH cellular level, are more sensitive to N-SIIs than untreated ones [105].

### 1.5.6 The Inhibitors G5 and 2C

The 2C (also called DU-UC15) is a N-SIIs developed in the laboratory of bio-organic chemistry leaded by prof. Fabio Benedetti (Department of Chemical and Pharmaceutical Sciences of University of Trieste). It is a symmetrical bis-arylidencycloalkanone structurally related to the nonselective iso-peptidase inhibitor G5 [103]. The structure of 2C contains two possible binding sites for the catalytic cysteines of DUBs and a hydroxyl group which allows further structure modifications and/or the covalent conjugation with other molecules (e.g. peptides, carriers, fluorescent probes) (**Figure 1.15**).

Over the inhibition of DUBs, the G5 inhibitor and its derivatives trigger a non-specific necrotic pathway that involves the actin cytoskeleton reorganization. The treatment with these drugs indeed stabilizes and increases the activity of protein phosphatase PP2A, which stimulates in turn the dephosphorylation of serine 3 on cofilin-1, a

protein with actin depolymerization activity. As the activity of cofilin-1 is negatively regulated by the phosphorylation of the serine-3, the treatment with G5 and its derivatives triggers indirectly the depolymerization of the cellular cytoskeleton and subsequently the necrotic death [106].

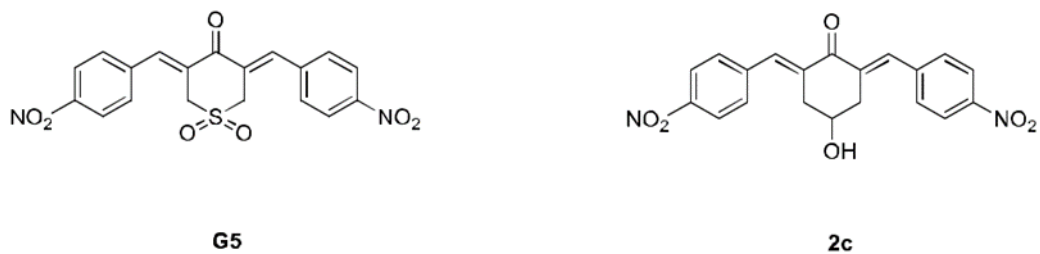


**Figure 1.15:** Chemical structure of inhibitors G5 and 2C.

## 2. Aim of the Study

The principal goal of this doctoral thesis is the assessment of the mechanical properties as new possible biomarkers of epithelial ovarian cancer (EOC) in association with the classic ones used in clinical routine. To do so, the Atomic Force Microscope (AFM) was used to perform the mechanical characterization of 9 ovarian cancer cell lines with different histological and morphological classification. An invasion assay was performed on the same cell lines to test the association between mechanical properties and the metastatic potential. Moreover, each cell line was treated with 2C, an anti-tumoral drug with cytoskeleton depolymerization activity, and then analysed to AFM in order to observe possible correlation between the mechanical properties and the drug responsiveness. The results of this analysis were validated with a fluorescence staining of F-actin and  $\beta$ -tubulin. To conclude, parallel AFM measurements aimed to observe the role of culture medium composition on achieved Young's moduli were carried out.

# 3. MATERIALS AND METHODS

## 3.1 Cell Lines

### 3.1.1 Culture Methods and Cell Lines Features

In this doctoral thesis nine different immortalized ovarian cancer cell lines have been analyzed, namely: CAOV3, HEY, IGROV1, OAW42, OVCAR4, OVCAR8, SKOV3, TYKNU and TYKNU CpR. The SKOV3 and IGROV1 were generously provided by Dr. A. Ricci (Burlo Garofolo Pediatric Institute, Trieste, Italy), while the other seven cell lines were provided by Prof. O.M. Carpen (University of Helsinki, Helsinki, Finland).

The HEY, OVCAR4 and OVCAR8 were cultured in RPMI 1640 medium (EuroClone S.p.A., Milan, Italy) supplemented with 10% fetal bovine serum (FBS, Sigma-Aldrich Co., St. Louis, USA), 1% Streptomycin-Penicillin 25X (EuroClone S.p.A., Milan, Italy) and 1% Gentamicin (EuroClone S.p.A., Milan, Italy). The SKOV3, CAOV3 and OAW42 were grown in high-glucose DMEM medium (Sigma-Aldrich Co., St. Louis, USA) supplemented with 10% FBS, 1% streptomycin-Penicillin 25X and 1% Gentamicin. Finally, the TYKNU and TYKNU CpR cell lines were cultured in EMEM medium (Sigma-Aldrich Co., St. Louis, USA) supplemented with 10% FBS, 1% streptomycin-Penicillin 25X and 1% Gentamicin, while the IGROV1 cells were grown in DMEM:F12 (1:1) medium supplemented (Sigma-Aldrich Co., St. Louis, USA) with 10% FBS, 1% streptomycin-Penicillin 25X and 1% Gentamicin.

All cell lines were incubated at 37 °C, in a humidified atmosphere of 5% CO<sub>2</sub> and were plated in flask (T25 or T75, Corning®, Corning, NY, USA) with filtered cap, which allows gas exchange and prevents contaminations.

#### 3.1.1.1 CAOV3

The CAOV3 cell line was isolated by J. Fogh in 1976 from a 54-year-old Caucasian female with serous adenocarcinoma (unpublished data). At the optical microscope, CAOV3 cells show an epithelioid morphology and a clustered growth characterized

by tightly packed colonies (**Figure 3.1a**). The doubling time of this cell line is around 65 hours, which indicate a relatively slow growth [107]. The analysis of chromosomal alterations display an aneuploid karyotype (generally triploid) and different structure alterations (e.g. [del(6)(q21-23)], a common chromosome aberration in ovarian cancer cell lines) [108].

#### 3.1.1.2 HEY

The HEY cell line was established from a xenografted ovarian tumor in immunologically deprived mice in 1980 [109]. The xenograft was derived from a peritoneal deposit of a moderately differentiated papillary cystadenocarcinoma of the ovary. The original patient's age is unknown.

The microscopic observation of HEY cells point out a mesenchymal-fibroblastic morphology with a certain degree of ramification. Moreover, the cells are usually poorly aggregated regardless of their cellular density (**Figure 3.1b**). The doubling time is of around 30 hours.

The HEY cell line is characterized by a highly aneuploid karyotype with common polyploid cells. The number of chromosomes vary from 43 to 113 and display an apparently bimodal distribution around 49 and 94 chromosomes (which can indicate two different clonal populations). There are different chromosome structure aberrations, like [del(3)(p12:)] (the short arm of chromosome 3 is frequently altered in ovarian cancer cell lines) and [del(6)(q21-23)] (found also in CAOV3 and SKOV3) [108].

#### 3.1.1.3 IGROV1

The IGROV1 cell line was derived from a 47-year-old woman with a stage III ovarian carcinoma extending to the cervix and rectum. The histological diagnosis classified the tumor as endometrioid carcinoma with serous clear cells and undifferentiated foci. This cell line was established in 1985 and has since become one of the most utilized cell lines in ovarian cancer research.

Morphological studies performed by electronic and optical microscope have highlighted polygonal epithelioid cells characterized by microvilli and tight junctions (**Figure 3.1c**). In particular, the observation at the electronic microscope has shown two different morphological populations: one with small cells with clear cytoplasm and

round nuclei and another one characterized by large cells rich in organelles with polyglobular nuclei. At confluence, a formation of foci has been observed. These foci can even lose adherence and float in culture medium in clusters of different size. The doubling time was estimated around 20 hours, which indicates a rapid growth. The IGROV1 cell line displays two clonal populations with different chromosome sets: pseudodiploid with 46 chromosomes and hypotetraploid with 92 chromosomes. The most common structural aberrations are the inversion at short arm of chromosome 3 (breakpoints located at 3p13 and 3p25) and the translocation between chromosomes 2 and 5 ( $t(2;5)(q33;q229)$ ). Finally, this cell line shows a microsatellite instability and sensitivity to cis-platin [110].

#### 3.1.1.4 OAW42

The OAW42 cell line was derived from an ascitic fluid of a 46-year-old patient relapsing after cis-platinum treatment. The tumor was diagnosed as a papillary serous cystadenocarcinoma.

The OAW42 cells show an epithelioid morphology (proved by presence of desmosomes), cellular and nuclear pleomorphism, prominent multiple nucleoli, occasional cilia and tendency to form hemi cysts at confluence (**Figure 3.1d**). This cell line has a doubling time of around 34 hours.

The OAW42 cell line has a complex karyotype characterized by different structural and numerical alterations. The chromosome set is hypotetraploid with aberrations in chromosome 1, 3, 4, 5, 12, 17, 18 and 20 [111].

#### 3.1.1.5 OVCAR4

The OVCAR4 cell line was isolated from ascites of a 42-year-old patient with a serous adenocarcinoma refractory to cyclophosphamide, cis-platinum, and Adriamycin treatment [112].

At the microscopic analysis, the OVCAR4 cells show a polygonal epithelioid morphology and a growth pattern characterized by tightly packed colonies (**Figure 3.1e**). The doubling time is of around 40 hours [107].

### 3.1.1.6 OVCAR8

The OVCAR8 cell line was isolated from a 64-year-old woman with serous adenocarcinoma previously treated with carboplatin chemotherapy.

Similarly to OVCAR4, the OVCAR8 cells are characterized by epithelioid morphology and clustered growth pattern (**Figure 3.1f**). The kinetics of growth instead is relatively quick, with a doubling time of around 24 hours [113].

### 3.1.1.7 SKOV3

The SKOV3 cell line was established in 1973 from the ascites of a 64-year-old Caucasian female with adenocarcinoma of the ovary. It is one of the most used ovarian cancer cell line in research.

The microscopic investigation reveals cells with fibroblastic morphology and different degrees of branching (**Figure 3.1g**). The doubling time is of around 40 hours [113]. The SKOV3 cells are resistant to tumor necrosis factor and to several cytotoxic drugs including cis-platinum and Adriamycin [114].

This cell line is characterized by two clonal populations with different karyotypes: hypodiploid and near-triploid. Several structural chromosome aberrations common in ovarian cancer cell line are recognized, such as deletions in short arm of chromosome 3 or in long arm of chromosome 6 [115] [108]. Moreover, the SKOV3 cells display a microsatellite instability.

### 3.1.1.7 TYKNU and TYKNU CpR

The TYKNU cell line was derived from a 38-year-old patient with undifferentiated adenocarcinoma of the ovary. Subsequently, a cis-platinum resistant subline named TYKNU CpR was developed by treatment of TYKNU cells with stepwise increasing concentration of cis-platinum.

From a morphological point of view TYKNU and TYKNU CpR cells show an elongated shape which suggests a fibroblastic-like morphology with a clustered growth at low density. At confluence, both cell lines form a monolayer with pavement-like arrangement characterized even by large cells (especially TYKNU CpR) (**Figure 3.1h-i**). The doubling time of these cell lines is similar, with 43 hours for TYKNU and 48 hours for TYKNU CpR.

Both cell lines show a hyperdiploid karyotype (56 chromosomes for TYKNU and 51 for the corresponding cis-platinum resistance subline) and similar chromosome aberrations, with an exclusive deletion of long arm of chromosome 7 in TYKNU CpR. This can suggest a possible involvement of genetic changes in the mechanisms underlining resistance to cis platinum [116][117].

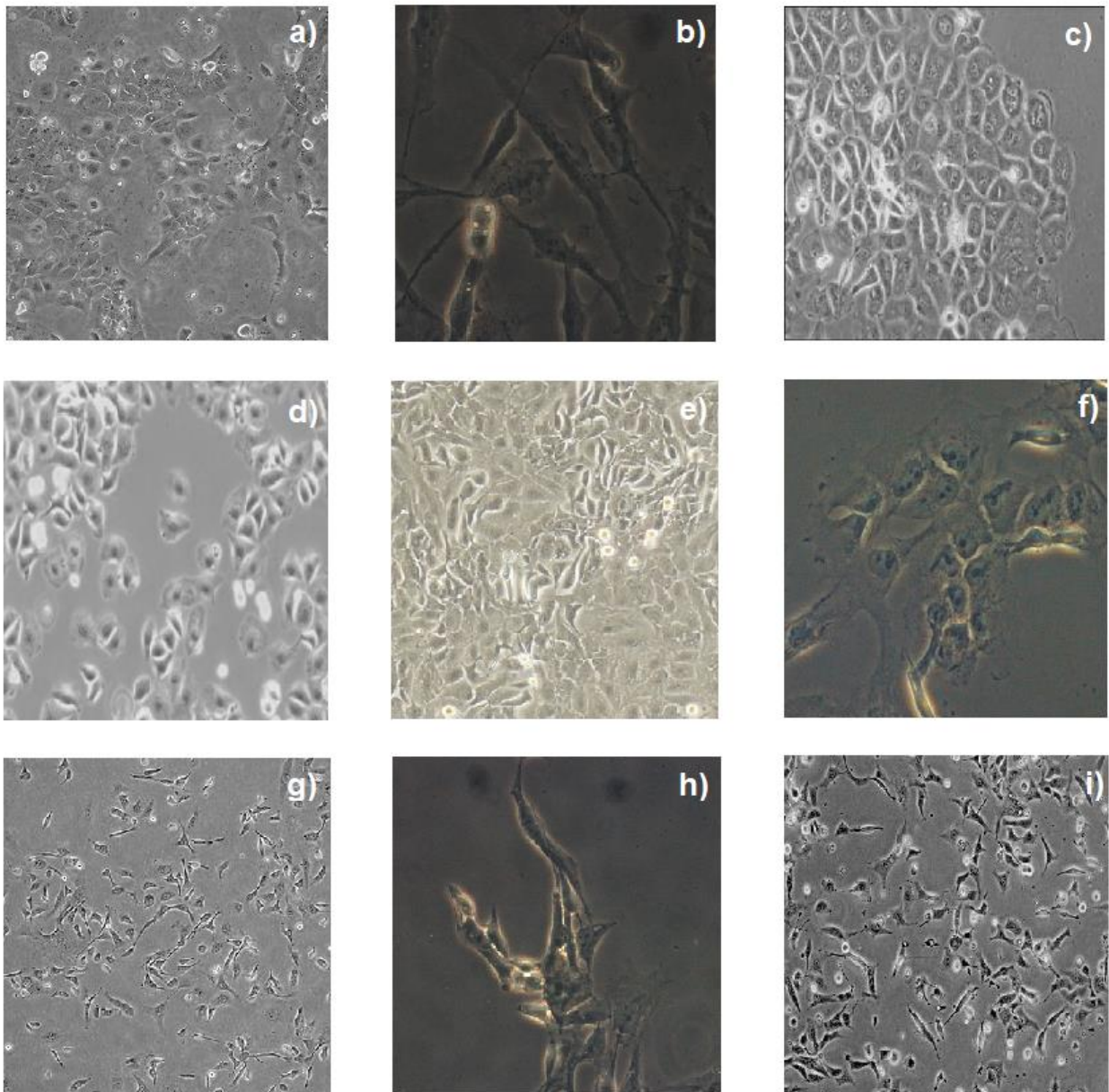


**Figure 3.1:** a) CAOV3, b) HEY, c) IGROV1, d) OAW42, e) OVCAR4, f) OVCAR8, g) SKOV3, h) TYKNU, i) TYKNU CpR. Adapted from ATCC, Kyeong A. So., CLS, EZ Biosystems, JCRB Cell Banks [170-175].

### 3.1.2 Histological Classification

Cell lines are the most frequently utilized models in cancer research, although genomic differences between them and tissue samples have been proved in several studies [118]. For this reason, the evaluation of cell lines molecular profiles is aimed to find the model that most closely resemble in vitro the molecular alterations of a given tumor subtype. As concern this thesis, the histological classification of the analyzed cell lines was based on the mutation status, expression levels and copy number alterations of genes usually reported in literature as biomarkers discriminating different EOC subtypes (see introduction chapters 1.1.4, 1.1.5, 1.1.6, 1.1.7 and 1.2.4) (**Table 3.1**). These data were collected from the database Broad-Novartis Cancer Cell Lines Encyclopedia (CCLE, <https://portals.broadinstitute.org/ccle>), which includes the genomic profiles of 1457 cancer cell lines commonly used in cancer research.

<b>EOC subtypes (Epithelial Ovarian Cancer)</b>	<b>Genetic Hallmarks</b>
<b>HGSOC (High Grade Serous Ovarian Cancer)</b>	<i>TP53 mut, BRCA1/2 mut, CDKN2A down/del, CCNE1 amp, RB1 del/mut, PIK3CA amp/mut, CCND2 over, PTEN del/mut, NF1 del/mut, Notch1-3 amp/mut, RAD complex mut, FANC complex mut, ATM mut, FOXM1 amp/over, C11orf30 amp/mut.</i>
<b>LGSOC (Low Grade Serous Ovarian Cancer)</b>	<i>ERBB2 mut, CHRNBA mut, PIK3CA mut, NRAS mut, KRAS mut, IGF1 high, BRAF mut, NF1 mut, TNK1 mut, NCK mut, PAK mut, RASSF1 mut, TSC1 mut, EIF1AX mut, USP9X mut.</i>
<b>CCOC (Clear Cells Ovarian Cancer)</b>	<i>ARID1A mut, ARID1B mut, ERBB2 mut/amp, KRAS mut, ERBB3 mut/amp, PIK3CA mut, PIK3R1 mut, PIK3R2 amp, AKT1-2 amp, SMARC4A amp, PTEN mut, PPP2R1A mut, TERT mut, HGFR amp.</i>
<b>ENOC (Endometrioid Ovarian Cancer)</b>	<i>TP53 mut, KRAS mut, ARID1A mut, PIK3CA mut, PIK3R1 mut, PTEN mut, CTNNB1 mut, KMT2B-D mut, PIK3R2 mut, AKT1 mut, POLE mut, ERBB2 mut, BCOR mut, SPOP mut.</i>
<b>MOC (Mucinous Ovarian Cancer)</b>	<i>TP53 mut, KRAS mut, BRAF mut, ARID1A mut, PIK3CA mut, ERBB2 mut/amp, CDKN2A mut/del/down, RNF43 mut, USH2A mut, HMCN1 mut, ZNF469, ABCA13 mut/amp, NEB mut/amp, FCGBP mut, DNAH14 mut.</i>

**Table 3.1:** Panel of genetic alterations hallmarks of most common EOC subtypes used for histological classification of cell lines. Mut: Mutated, Amp: Amplified, Del: Deleted, Down: Down-expressed, High: Over-expressed.

### 3.1.3 Morphologic Classification

Mammalian cells can be divided in three main groups according to their morphology:

- Fibroblast or fibroblastic-like: characterized by bipolar/multipolar and elongated shape. They grow attached to substrate and often form cluster in which they align in parallel strips (**Figure 3.2a**).

- Epithelial-like: shows polygonal shape and in general more regular dimensions. They grow attached to substrate usually in discrete clusters (**Figure 3.2b**). These cells exhibit a basal-apical polarity which divided the plasma membrane in two sub-areas with different structures and functions. In cultured cell lines, the apical membrane faces the culture medium, while the basolateral membrane spreads between the single cells and the culture vessel. Neighboring cells are connected by tight junctions.
- Lymphoblastic-like cells: cells are rounded and grow in suspension (**Figure 3.2c**). An example of lymphoblastic-like cells are the blood cells [119].

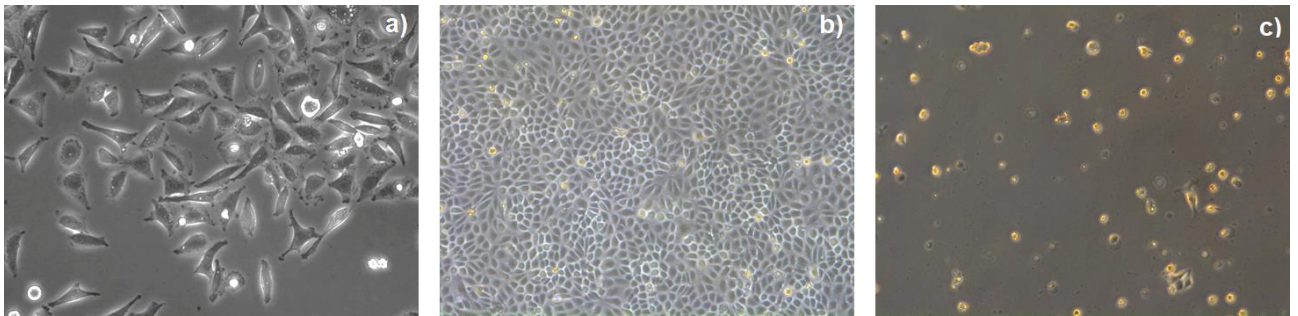


**Figure 3.2:** a) Fibroblastic Morphology; b) Epithelial Morphology; c) Rounded morphology. Adapted from Greb [119].

It has already been reported that the morphological features of cells can be related to their fundamental molecular and physiological properties, such as health status, cell cycle progression, responsiveness to drug, metastatic potential, and cytoskeleton organization [120] [121]. Consequently, to find a possible correlation between the morphological features of the cell lines and their mechanical properties, some shape parameters were obtained for each cell lines used in this thesis by ImageJ (U. S. National Institutes of Health, Bethesda, Maryland, USA), an open-source software commonly used for analyzing microscope images [122]. This software allows segmenting single cells and achieving different shape parameters, such as the cell perimeter and area. Since each cell line grows attached to a substrate, rounded morphology was automatically excluded, and the analysis was aimed to discriminate cell lines into fibroblastic-like and epithelial-like. To do so, single cells was analyzed by ImageJ to obtain the circularity (C) and the aspect ratio (AR), two markers of cell elongation degree. In particular, the circularity is a parameter indicating how much the cell profile resembles a perfect circle (with circularity equal to 1) and it is expressed by:

$$C = \frac{4\pi A}{P^2} \quad (1)$$

Where A is the area of cell and P its perimeter (**Figure 3.3b**). Instead, the AR is defined as the ratio between the length of major axis and of minor axis for the best-fitted ellipse of the cell. The latter is defined as an ellipse with the center in the cell centroid and the same area of fitted cell (**Figure 3.3a**) [123].

Since the fibroblast-like cells have a more elongated shape than epithelial-like ones, an AR higher than 2.5 and a C lower than 0.5 were established as hallmarks of cell lines with fibroblastic-like morphology.

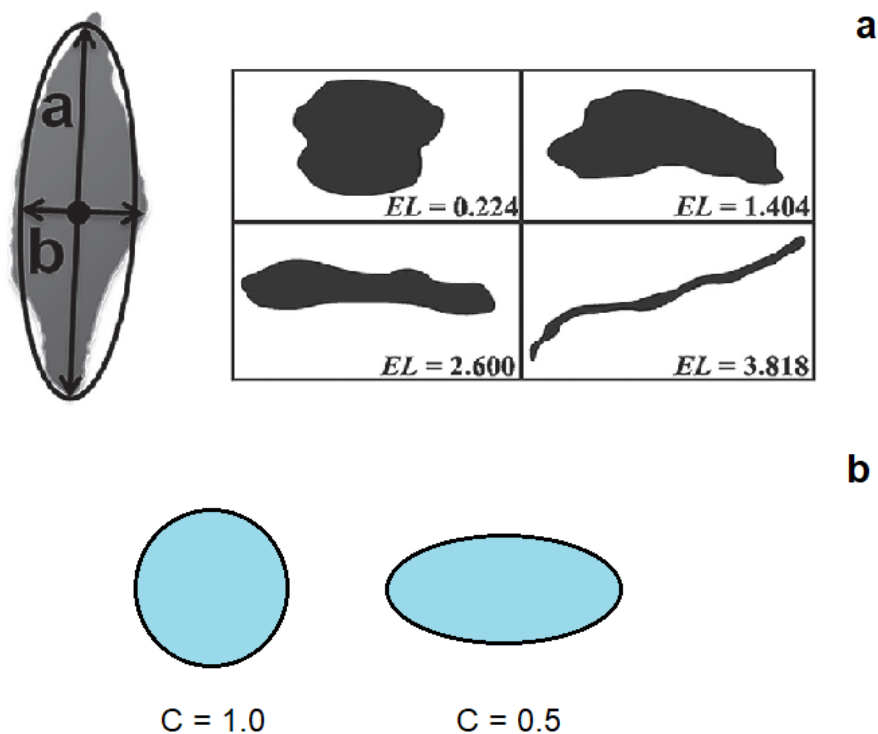


**Figure 3.3:** a) Schematic diagram of Aspect Ratio (AR) or Elongation (EL), that is the ratio between the major axis (a) and minor axis (b) of the best-fitted ellipse of the cell. In the right panel is possible to observe how the cell profile changes in function of the elongation; b) Circularity of a perfect sphere (left) and an ellipse (right). Adapted from Yu [123].

### 3.1.4 Cell Count and Viability Assay

In order to have healthy cells for subsequent measurements, cell lines were cultured for a number of passages ranged between 1-4 after their thawing. This allows recovering cell lines from freezing and avoiding possible modifications due to

excessive passages. Moreover, the viability of cell line was tested at each passage by the use of the Thoma cell counting chamber (Exacta-Optech Labcenter S.p.A., San Prospero, Modena, Italy). The latter is a tool which allows performing a cellular count by the use of a grid printed on its surface. This grid is basically structured in sixteen squares bordered by three parallel lines including smaller squares bordered inside in turn by two parallel lines. The application of a coverslip glass on the grid leads to the formation of a thin space which can be filled with the cell suspension by capillarity. In this way the cells are spread over the grid and can be counted separately in each square under an optical microscope (**Figure 3.4a**). After at least four independent counts, the number of cells in 1 mL of original cell suspension is derived as follows:

$$X_n = nm * CF * 10^4 \quad (2)$$

Where  $X_n$  is the number of cells in 1 mL of cell suspension,  $nm$  is the mean of independent counts,  $CF$  is the dilution coefficient of cell suspension aliquot load in Thoma chamber and  $10^4$  is the conversion factor for the latter.

The Thoma chamber can be used also to test the cell viability by the use of Trypan blue, a dye able to penetrate only damaged cellular membranes and so marking only the cytoplasm of dead cells. This provides an overview of general health status of cultured cell lines (usually a percentage of alive cells greater than 90 indicate a healthy cell line) (**Figure 3.4b**).

As concern this thesis, the viability assay was performed at each cell line passage by dilution of 10  $\mu$ l of cellular suspension in 10  $\mu$ l of Trypan blue 0.04% (Sigma-Aldrich Co., St. Louis, USA) in PBS 1X (Sigma-Aldrich Co., St. Louis, USA). Subsequently, 10  $\mu$ l of this solution was loaded in Thoma Chamber and the number of living (not

marked) and dead (marked) cells was counted under the optical microscope (Nikon Eclipse TS100, Nikon, Tokyo, Japan).

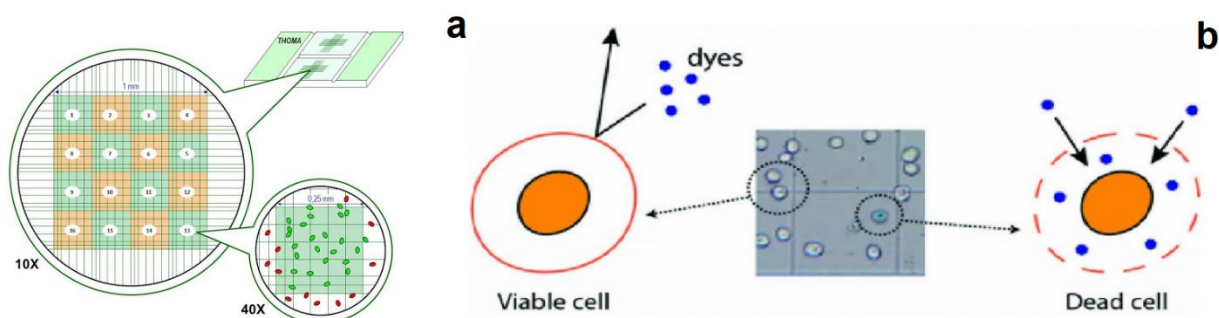


**Figure 3.4:** a) Grid of Thoma Chamber; b) Labelling of cells by Trypan Blue. Adapted from Rs'science [176].

## 3.2 AFM

The principal aim of this doctoral project is the mechanical characterization of nine cell lines described above in order to achieve a new possible characterization biomarker of EOC and a deeper comprehension of the latter by combination between the mechanical and the molecular properties. This characterization was performed by atomic force microscope (AFM), a scanning probe microscope (SPM) able to provide the mechanical properties of materials.

The working principle of AFM is based on use of a cantilever, a micro-lever with its own elastic constant which deflects when brought into contact with the sample. The cantilever is usually made up of silica or silicon nitride, it has a triangular or rectangular shape and a length of 100-200  $\mu\text{m}$ . Usually, the end of cantilever is functionalized with a pyramidal tip for high-resolution imaging.

The cantilever is covered up with a gold layer able to reflect a laser beam pointed on it on a photodiode, which acts as detector system. So, any deflection of the microlever leads to a movement of the laser on the photodiode and generates an electric signal proportional to the size of the cantilever deflection (**Figure 3.5**). This signal can provide the force which led the microlever deflection by Hooke's Law. The latter states that the force needed to compress or expand a spring is directly proportional to the elastic constant of the spring and the module of spring deformation:

$$\mathbf{F} = -\mathbf{k}\mathbf{s} \quad (3)$$

Where  $F$  is the force,  $k$  the elastic constant of spring and  $s$  the module of deformation. The minus sign (-) is required for cantilevers where the direction of deformation is opposed to the force one. Since the size of the deflection depends on material features, the achieved force can provide different information about the analyzed sample.

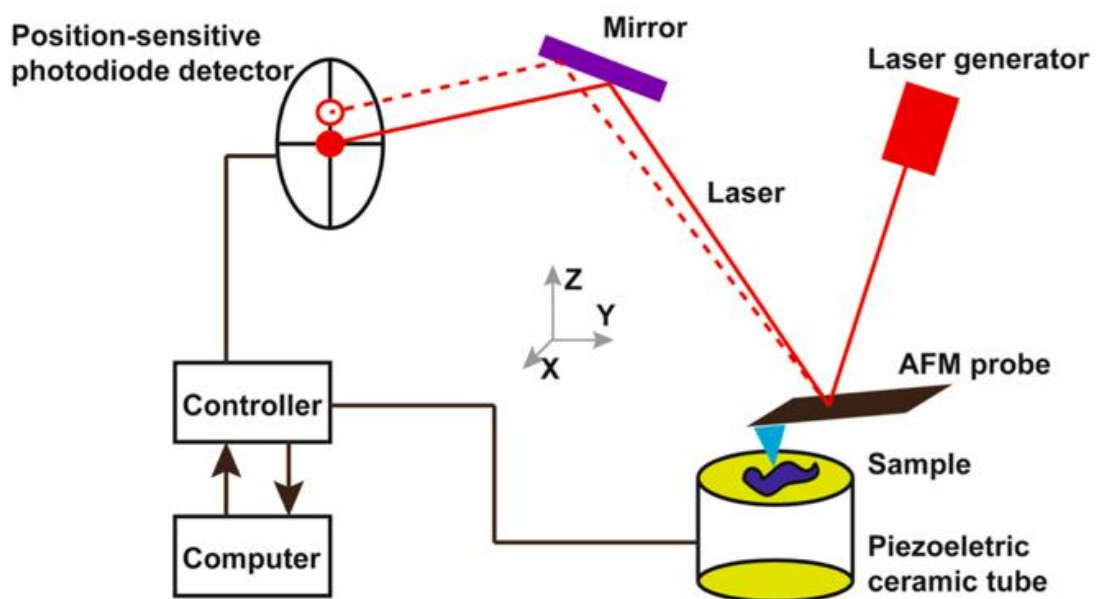


**Figure 3.5:** Schematic diagram of AFM working principles. Adapted from X. Deng [177].

To obtain the mechanical properties of cell lines, it was used a particular AFM mode called Single Cell Force Spectroscopy (SCFS), in which the achieved forces are analyzed in function of probe distance from the sample. In SCFS the cantilever is initially brought into contact with cell and then it is retracted towards it. This leads to a generation of a force-displacement curve which can be divided in two sections: an initial approach curve and a subsequently retract curve. The latter is inherent to retraction of cantilever from the cell and provide information on adhesive properties of the sample under test. In this project, it was used the approach curve, that is the section of force-displacement curve characterized by a force increase associated to the first contact between the cantilever and the cell. Since the force increase is determined by the sample stiffness, the analysis of approach curve is useful to obtain

the mechanical properties of cell under test. In SCFS the cantilever is functionalized with a tip of well-defined geometry to punch into the cell throughout the approach step (**Figure 3.6**). This microindentation allows a deeper and more accurate mechanical characterization of the cell by contact of its inner parts.

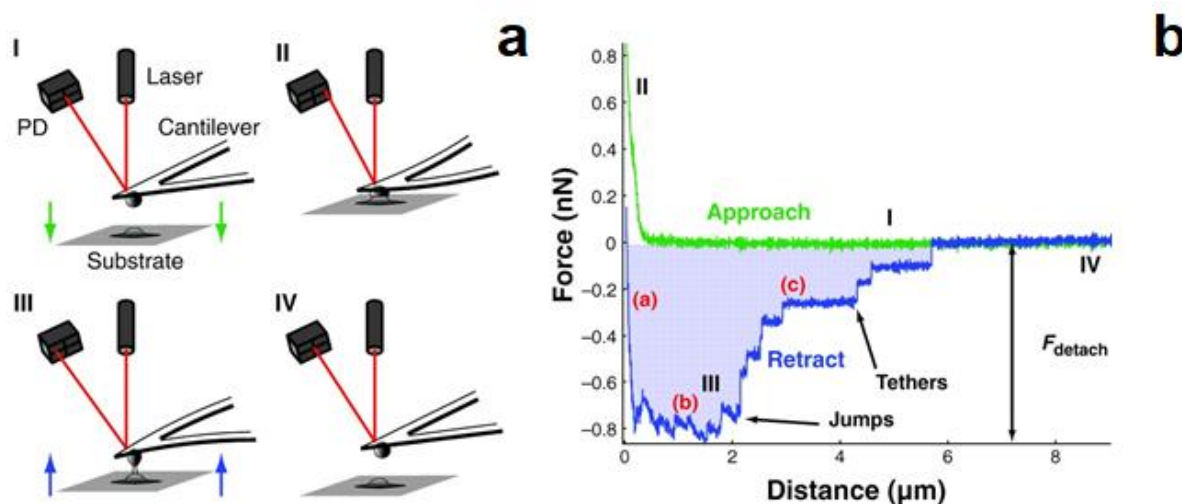


**Figure 3.6:** a) Schematic diagram of Force Spectroscopy working steps: I. Approach, II. Contact and indentation, III. Retraction, IV. Return of cantilever to initial position; b) Force-Displacement curve where are reported the different steps illustrated in panel a) to indicate the corresponding regions of the curve. Adapted from Soft Matter Wiki [178].

### 3.2.1 Cell Seeding

Before measurements, cells were seeded on a support which can be transferred in AFM. In this thesis, the cell seeding was carried out on a quadrangular glass coverslip with side of 1.8 cm (LLG®, Meckenheim, Germania). The latter was initially sterilized in autoclave and then put in ethanol 100% to maintain the sterility. Before the cell seeding, the coverslip was placed in a six-well cell culture plate (Costar, Corning®, Corning, NY, USA) and treated with 100  $\mu\text{l}$  of Poly-L-Ornithine 0.01% (Sigma-Aldrich Co., St. Louis, USA) to promote cell attachment on it. After two hours at 37 °C to stimulate the polymerization of poly-L-ornithine, an aliquot of cell suspension was spotted on the coverslip at a cellular density of around  $7.0 \cdot 10^3$  -  $8.0 \cdot 10^3$  cells for  $\text{cm}^2$ . AFM measurement was performed within three days after the seeding to allow the cellular growth and simultaneously to have well separated cells.

### 3.2.2 AFM Set-up

For AFM measurements a MF3D-Bio AFM (Asylum Research, Santa Barbara, CA) with inverted optical microscope (Nikon, Melville, NY) was used. The single cell force spectroscopy was performed using the cantilevers PNP-TR-TL-50 (Nano World, Neuchâtel, Switzerland) with triangular shape and nominal elastic constant of 0.32 - 0.08 N/m. Moreover, the cantilevers were functionalized with silica beads with diameter of 4.5  $\mu\text{M}$  to allow cell microindentation and decrease simultaneously the risks of sample damages.

#### 3.2.2.1 Cantilever Functionalization

To attach the silica bead on the cantilever end, a glue that cures when exposed to UV was used, namely NOA 73 (Norland products Inc., Cranbury, NJ, USA). In first place, the cantilever loaded on AFM head (The AFM component with all functional elements) was brought into contact with the glue placed on a microscope slide. This step was aimed at withdrawing with cantilever end a small glue droplet required for bead attachment. Subsequently, the cantilever was approached to several silica beads placed near the glue on the same microscope slide. Taking care to place the bead at cantilever end as closely as possible, the microlever was slowly retracted to pick up the silica bead (**Figure 3.7**). Finally, the functionalized cantilever was exposed to UV for at least 20 minutes and then left at room temperature for around one week to stabilize the glue [124].

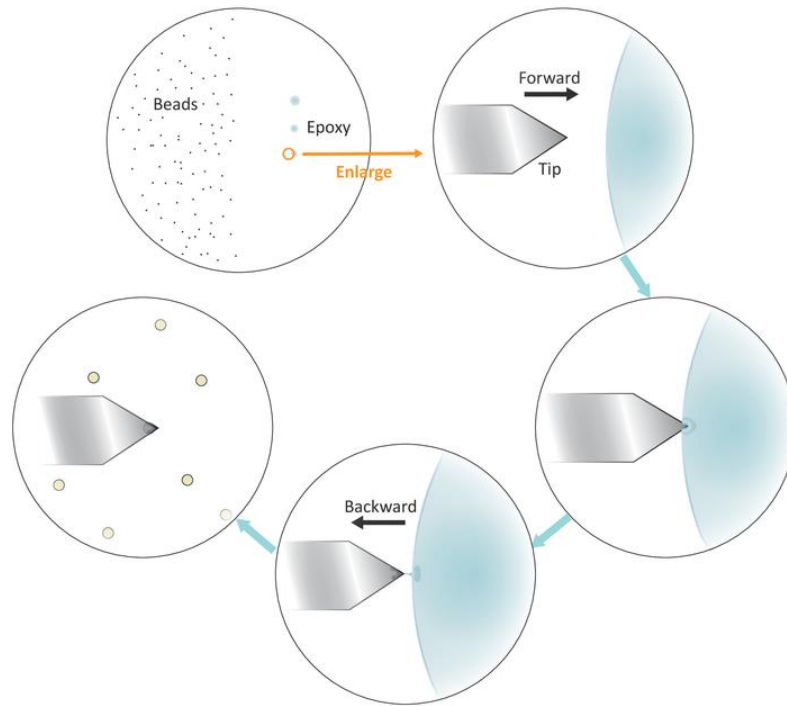


**Figure 3.7:** Steps of cantilever functionalization with bead.  
Adapted from Chen J [124].

### 3.2.2.2 Cantilever Elastic Constant Calibration

Although the nominal elastic constant of cantilever is reported in the manufacturer's instructions, it is a good practice to perform an elastic constant calibration at the beginning of each experimental section. Basically, the first step of cantilever calibration is aimed at obtaining the invOLS (inverse optical lever sensitivity), a parameter that describes the amount of photodiode response per nanometer of cantilever deflection. To do so, a force spectroscopy was performed on surface of a microscope slide with a drop of sterilized milliQ H<sub>2</sub>O. The calibration was in liquid environment because the subsequent AFM measurements were performed in culture medium. The contact region of the resulting force curve was fitted to obtain the slope (in nm/V), the reciprocal of which is the invOLS (in V/nm).

The next step was the determination of the spring constant by thermal noise, a method based on the continuous vibration of the cantilever in air or liquid. In this method, the thermal vibration of laser beam is recorder by the photodiode to obtain a force spectrum with different peaks. The fit of data segment centered at lowest-frequency peak provides the spring constant of the cantilever [125].

### 3.2.3 AFM Measurements

Once the cantilever was calibrated, it is possible proceed with AFM measurements. For each cell line around 100 different cells were analyzed by Force spectroscopy in three different experimental sections. To avoid unhealthy or apoptotic cells, an optical assessment of their state of health was performed before the indentation. Rounded and poorly attached cells were excluded from the analysis.

The measurements were carried out in complete medium warmed at 37 °C to keep cells healthy during the analysis. For the same reason, the AFM analysis was performed within two-three hours. For each analyzed cell at least five force-displacement curves at different locations in the cell peri-nuclear region were collected. The microindentation was performed at an indentation velocity of 2  $\mu\text{m/s}$  (slow enough to avoid hydrodynamic effects) and force distance of 5  $\mu\text{m/s}$  (large enough to ensure that the tip will be fully detached from the cell between indentation instances). Moreover, the deflection trigger point (indicating the maximum force of indentation) was settled at 2 nN to avoid cell damage [125].

### 3.2.4 Data Analysis

The recorded force-displacement curves were analyzed at the end of each experimental section to obtain the mechanical properties of the tested cells. To do so, the Hertz model, a mathematical model able to appropriately describe the interaction between cantilever and cell, was used. The latter approximates the sample to an isotropic and linear elastic solid occupying an infinitely extending half space. Furthermore, it assumes that the indenter is not deformable and that there are no additional interactions between indenter and sample (for this reason it is important to use clean cantilever). If these conditions are met, the Hertz model is able to fit the contact region of force-displacement curve achieved with force spectroscopy to obtain the Young's Modulus (E), a parameter that indicate the materials stiffness [126].

There are different variants of Hertz model according to the shape of the indenter: spherical, pyramidal, and conical (**Figure 3.8**) [127]. Since in this thesis the cantilever was functionalized with a bead, the Hertz model variant used to fit the achieved displacement-force curves was the following one:

$$F = \frac{4ER^{0.5}}{3(1-\nu^2)} \delta^{1.5} \quad (4)$$

Where  $\nu$  is the Poisson's ratio (assuming to be 0.5 for soft biological samples),  $R$  is the radius of bead,  $\delta$  is the indentation,  $F$  is the force recorded and  $E$  the Young's modulus.

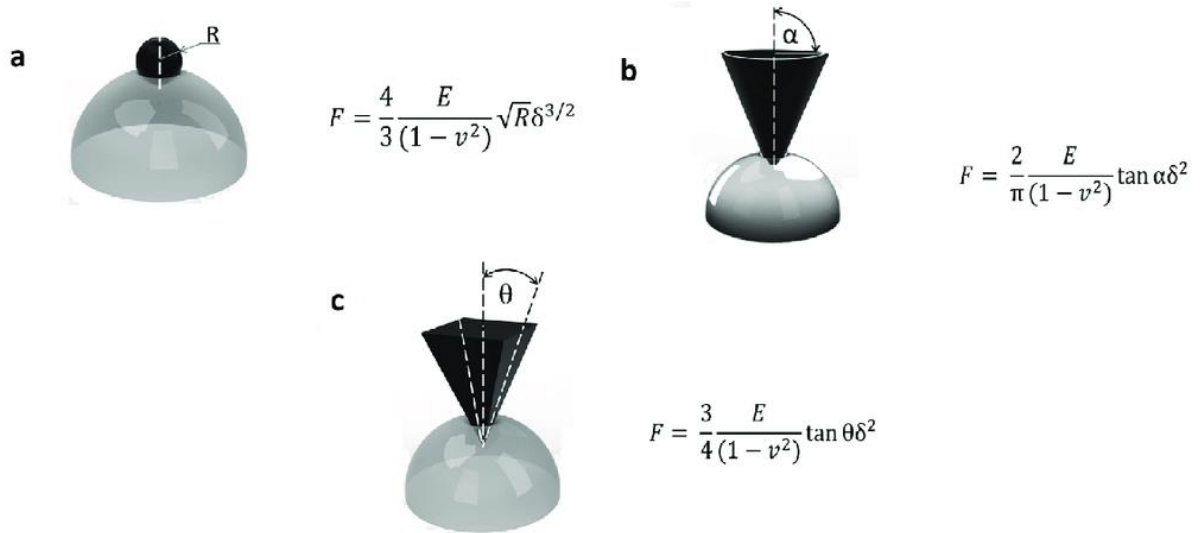


**Figure 3.8:** Schematic representation of Hertz model with different indenter geometry: a) Spherical; b) Conical; c) Pyramidal. Adapted from Perez S.C. [179].

The fitting of curves was performed using a custom Igor pro 8 (Wavemetrics, Lake Oswego, OR, USA) procedure integrated in the management software of AFM. The advance of the custom procedure is the automatic identification of contact point, which is the part of the curve inherent to the first contact between cantilever and sample. The correct identification of the contact point is essential to have a good fitting [125]. As concern this thesis, the force curves were fitted at a maximum indentation of 500 nm. This value allows significant indentation of cells with different heights and stretching remaining simultaneously within the linear viscoelasticity.

### 3.2.5 Variation in Experimental Set-up

Over standard measurements described above, the parallel AFM analysis was performed in order to investigate possible effects of experimental set-up variations on achieved Young's modulus.

The first aspect to be investigated, was the influence of culture methods on cell stiffness. The culture media differ in components concentration (e.g. calcium,

phosphate, glucose, nutrients) and this was reported to influence cell proliferation and cell viability [128]. Therefore, there is a possible role played by culture medium composition in the mechanical properties of cells [129]. These possible effects need to be taken into consideration when interpreting elasticity measurements in cell lines grown in different media.

To this aim, IGROV1 was cultured in DMEM:F12 (1:1) and RPMI 1640 (supplemented with equal concentration of FBS and antibiotics). These culture media differ in several parameters, such as amino acids and glucose concentration (higher in DMEM:F12). After 2-3 passages, around 30 cells from each subline were analyzed at AFM as described above.

An important component of a complete medium is the FBS, a complex mix of albumins, growth factors and growth inhibitors. It serves as source of molecules essential for cell proliferation and survival, such as amino acids, vitamins, proteins, lipids, hormones, growth factor and protease inhibitor [130]. A possible role played by FBS in the determination of cell stiffness should be considered.

Therefore, TYKNU CpR was split in two sublines and cultured in EMEM with two different concentrations of FBS: 10% and 20%. After 2-3 passages, around 30 cells for each subline were analyzed in AFM.

Finally, since some cell lines with epithelial morphology display a clustered growth which does not allow analyzing well-separated cells, the mechanical properties of IGROV1 cells from small cluster (with 3-4 cells) and from a continuous monolayer were compared. The aim of this analysis was to investigate if cells in confluence characterized by complex interactions with neighboring cells show different mechanical properties in comparison to the same ones in small colonies. According to this purpose, IGROV1 cells were seeded on two coverslip and analyzed with AFM after three days and one week. The cells analyzed after three days were characterized by certain well-separated small clusters, while the ones left in culture for one week reached the confluence and formed a continuous monolayer.

### **3.3 Invasion Assay**

An important step toward metastasis is the invasion through the extracellular matrix (ECM). The first step of invasion is the adhesion and spreading of tumoral cells along the blood vessel walls. Then, the expression of specific proteolytic enzymes, such as MMP collagenases, induce the formation of tiny holes in the basement membrane

surrounding the blood vessels allowing cancer cells to invade [131]. Before that, the tumoral cells undergo a particular transformation called epithelial-mesenchymal transition (EMT). As the name suggests, the EMT is a process by which epithelial cells lose polarity and cell-cell adhesion in order to assume a mesenchymal morphology and gain migratory and invasive properties. This transformation is involved in several biological processes, such as wounds healing and also the metastatic diffusion.

The EMT induces cytoskeletal structure changes and influences in this way the cell stiffness [132]. This suggests a possible use of mechanical properties as marker of malignancy.

Accordingly, the metastatic potential of the cell lines analyzed in this thesis was carried out by the use of the CHEMICON Cell Invasion Assay Kit (EMD Millipore Corp., Burlington, Massachusetts, USA). The working principle of this kit is based on an invasion chamber, a 24-well tissue culture plate with 12 cell culture inserts. The insert contains an 8  $\mu\text{m}$  pore size polycarbonate membrane, over which a thin layer of ECMatrix™ (which simulates the basement membrane) is dried. The ECM layer occludes the membrane pores, blocking non-invasive cells from migrating. The invasive cells instead can migrate and cling to the bottom of the polycarbonate membrane. Basically, by injecting a serum free cell suspension aliquot on insert and filling the well with complete medium it is possible to observe the invasion potential of cells using the FBS as chemoattractant (**Figure 3.9a**).

For each cell line, a cell suspension aliquot in serum free medium containing  $0.9 \times 10^6$  cells/ml was injected in the cell culture insert. After 72 hours of incubation, the non-invading cells were washed out from the insert while invading ones were colored using the kit's staining solution and counted through an optical microscope. The average invading cells number for each cell line was achieved by cell count of at least three optical fields at a magnification of 10X (**Figure 3.9b**).

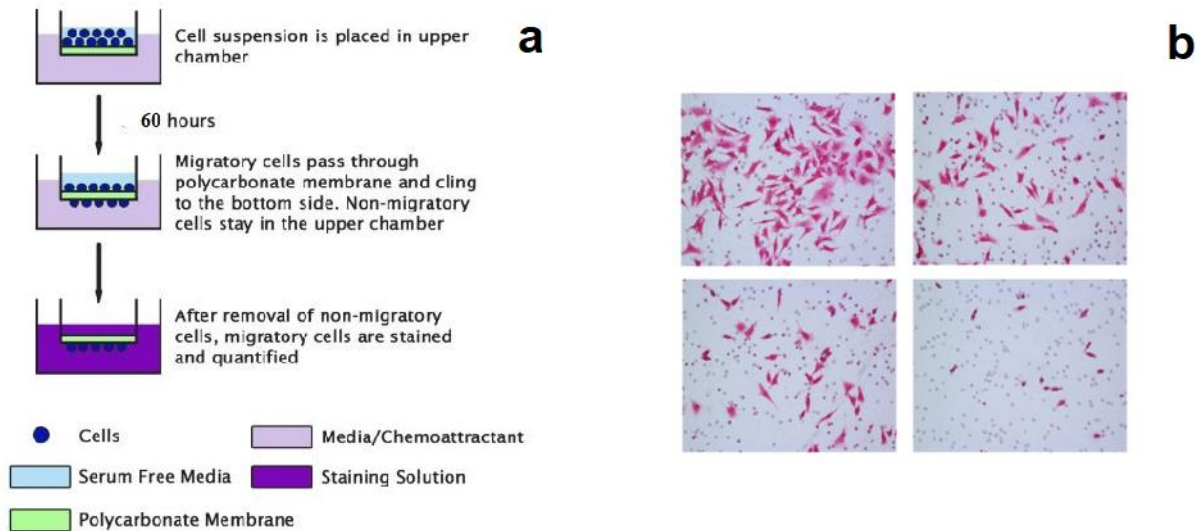


**Figure 3.9:** a) Schematic diagram of the invasion chamber working principle; b) Microscope images of stained invasive cells from cell lines with different metastatic potential. Adapted from Cellbiolabs and Wang Y. [180][181].

### 3.4 2C Treatment

The 2C is a new non-selective and irreversible inhibitor of isopeptidases used in tumor treatment. The inhibition activity of this drug is due to two possible binding sites on its structure for the catalytic cysteines of isopeptidases. Basically, the thiol group of cysteines is alkylated by 2C to irreversibly inhibit the catalytic activity. The principal target of this drug are the DUBs, a class of isopeptidases involved in the proteasome-mediated protein degradation pathway. The inhibition of DUBs leads to a proteo-toxic shock of tumoral cells, which are extremely dependent on the functional protein degradation pathway because of the high number of aberrated proteins.

Some efforts have indicated a parallel activity of this drug in triggering a cellular necrotic pathway that involves the cytoskeletal reorganization. This is due to the wide range of proteins which can be targeted by the inhibitory activity of 2C. For instance, it was proved that this drug stabilizes and increases the activity of protein phosphatase PP2A, which in turn stimulates the dephosphorylation of serine 3 on cofilin-1, a protein with actin depolymerization activity. As the latter is negatively regulated by the phosphorylation of the serine-3, the treatment with 2C triggers indirectly the depolymerization of the cellular cytoskeleton and subsequently the necrotic death (**Figure 3.10**) [106] [133].

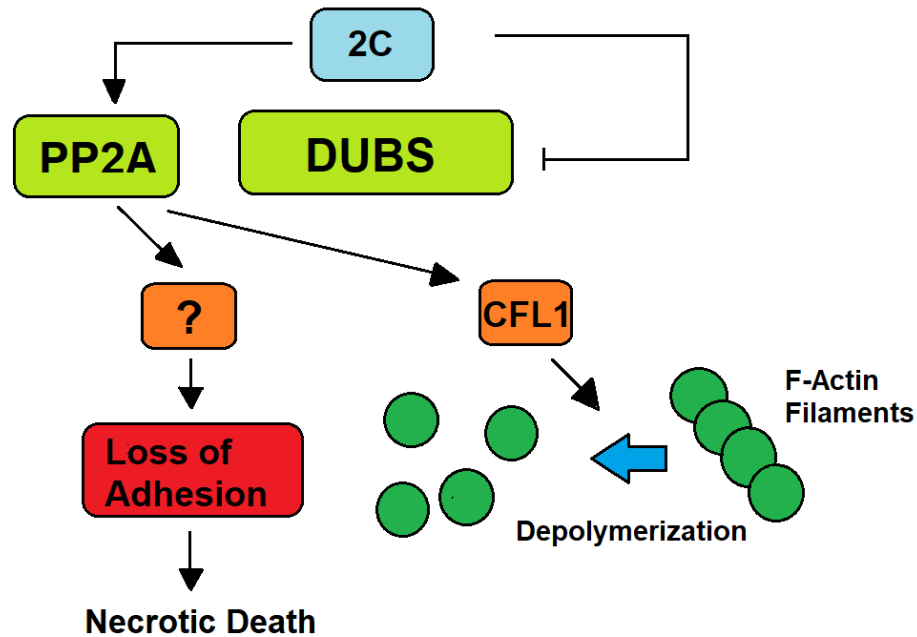


**Figure 3.10:** Summary of the necrotic pathway engaged by 2C. CFL1: Cofilin 1. Adapted from Ciotti [133].

According to this evidence, the cell lines were treated with 2C and then analyzed by AFM. The aim of this measurement was to investigate the mechanical properties as predictive markers of drugs effectiveness in the treatment of different tumor subtypes.

### 3.4.1 2C Sensitivity Assessment

Firstly, the IC<sub>50</sub> was achieved for each cell lines for 2C. The IC<sub>50</sub> indicates the concentration of a drug at which there is the 50% of its max inhibitory activity. This parameter is a measure of the potency of a substance in inhibiting a specific biological or biochemical function. The assessment of IC<sub>50</sub> was performed to observe the sensitivity of each cell line to 2C and the possible correlation between the drug resistance and the mechanical behavior.

To do so, each cell line was treated for 24 hours with increasing concentrations of 2C: 1-2-4-10-20-40-80 uM. Afterwards, an assessment of cell viability for each concentration was performed by MTT assay.

The MTT assay is a colorimetric analysis based on the enzymatic activity of the lactate dehydrogenase. In viable cells, this protein reduces the tetrazolium dye MTT 3-(4,5-dimethylthiazol-2-yl)-2,5-diphenyltetrazolium bromide to its insoluble formazan, which has a purple color (**Figure 3.11**). As a consequence, cell lines with

resistance to a specific drug will develop a high intense color after treatment because of the high number of living cells.

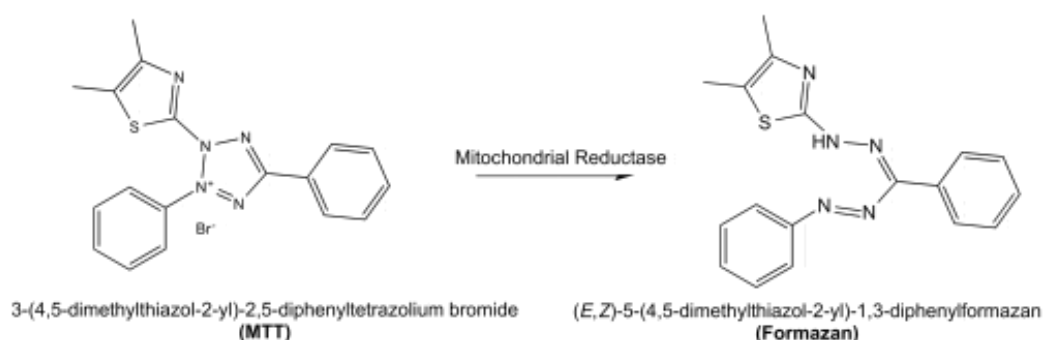


**Figure 3.11:** Reduction of MTT to formazan in Mitochondria.

In this thesis, the MTT (Sigma-Aldrich Co., St. Louis, USA) was initially administered to cell lines treated with 2C at a concentration of 0.4 mg/ml. After 4 hours in incubator at 37 °C, the cell lines were treated with DMSO (EuroClone, Milan, Italy) to solubilize the formazan crystals and then analyzed at the spectrophotometer at 570 nm (Spectra Max Plus 384, Molecular Devices, San Jose, California, USA). The percentage of viable cells was calculated as follows:

$$\%C = \frac{\text{OD treated cells}}{\text{OD untreated cells}} * 10 \quad (5)$$

Where %C is the percentage of viable cells and OD the optical density recorded at the spectrophotometer.

The calculation of IC50 from experimental data of MTT assays was performed by using a four-parameter logistic regression model, so called because it uses four key parameters in the equation as follows:

$$Y = \text{Max} - \frac{\text{Max} - \text{min}}{1 + \left(\frac{X}{\text{IC50}}\right)^{\text{Hill}}} \quad (6)$$

Where the four parameters are min (minimum inhibition response, assuming to be 0 because negative response are typically incoherent in biological contexts), Max (maximum inhibition response), Hill (Hill Coefficient, an indication of the steep of the

response curve) and IC50. X and Y indicate respectively the drug concentration and the corresponding percentage of dead cells after treatment (**Figure 3.12**) [134].

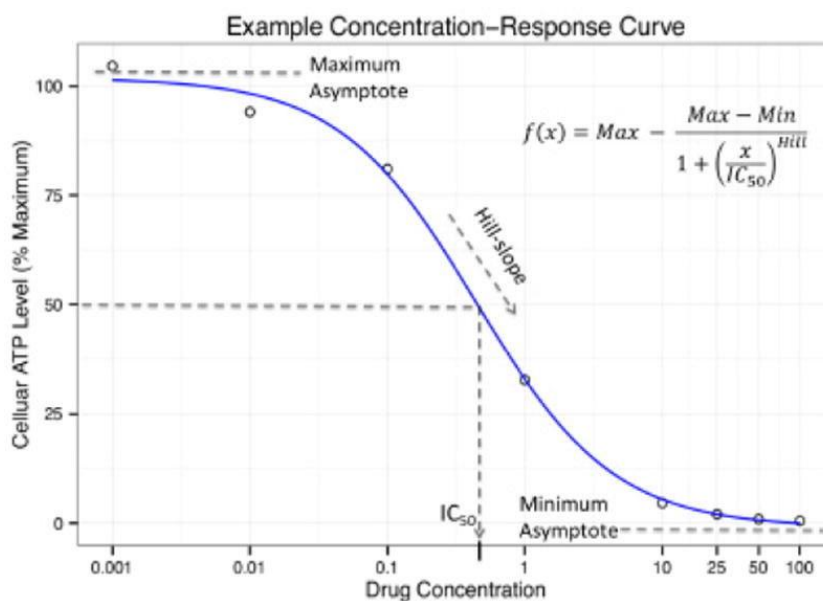


**Figure 3.12:** Example of the sigmoidal curve with four parameters: Min, Max, IC50 and Hill coefficient. Adapted from Beam A. [182].

### 3.4.2 2C Uptake Assay

The time-course AFM analysis of cell lines treated with 2C was performed in medium supplemented with the drug to observe the 2C effects on the mechanical properties in real-time. To do so, it is fundamental to know the 2C uptake kinetics in cells to understand the time required by the drug to be incorporated in the cellular population at appropriate levels.

The 2C uptake assay was performed by the use of the drug labelled with the fluorophore 4-propylamino-N-allyl-1,8-naphthalimide (F2,  $\lambda$  emission = 524nm, green). The 2C structure is indeed characterized by a hydroxyl group in position 4 of cyclohexane ring which allows the functionalization with several molecules, such as fluorophores. The evaluation of 2C uptake was performed at two different time steps after drug administration: 6 and 24 hours. The OVCAR4 and HEY cell lines were seeded on coverslips and left in culture for one day. Subsequently, they were treated with 2  $\mu$ M of 2C-F2 and fixed in 4% paraformaldehyde for 15-20 minutes after the two time checkpoints. After fixation, the coverslips were treated with DAPI and assembled on a microscope slide. Finally, images of the cell lines were obtained at the

fluorescence microscope (Leica DM2000, Leica Microsystems, Wetzlar, Germany) and the intensity of the fluorescence was achieved by ImageJ.

### **3.4.3 AFM Measurements of Treated Cell Lines**

Before AFM analysis, the cell lines were seeded on coverslips as described above and left in culture for two-three days. Afterwards, they were treated with 20  $\mu$ M of 2C and analyzed at AFM after seven hours. To have comparable results, the AFM experimental set-up was basically the same as the one used for untreated cells. For each cell line, around 70 cells were indented in different spots of their peri-nuclear region. Moreover, to observe possible time-depending effects of 2C on mechanical properties, around 30 cells for each cell line were analyzed in parallel by AFM keeping the 2C in the medium during the measurement.

The force-displacement curves were analyzed using the Hertz model with stricter fitting parameters since the 2C treatment leads to higher percentage of unhealthy and apoptotic cells. As concern the AFM analysis performed in medium supplemented with 2C, since it was carried out between 7 and 9 hours from the drug treatment, the achieved Young's Moduli were divided in four half-hour groups (7:00-7:30, 7:30-8:00, 8:00-8:30, 8:30-9:00) to better observe the changes in average stiffness with time.

### **3.4.4 Immunofluorescence Assay**

Since the 2C have a side effect on the cytoskeletal organization, an immunofluorescence assay for  $\beta$ -tubulin and a phalloidin fluorescence assay for F-actin were carried out on TYKNU, HEY and OVCAR4 cell lines before and after 2C treatment.

#### *3.4.4.1 $\beta$ -Tubulin*

The immunofluorescence stain of  $\beta$ -tubulin was aimed at observing the microtubule network organization after 2C treatment. Microtubules are important components of the cytoskeleton and are involved in several biological processes, such as cell shape determination and maintenance, vesicular transport, and spindle formation during mitosis. With this aim, OVCAR4, HEY and TYKNU cell lines were seeded on two different coverslips, one of which was used as negative control by treatment with 2

$\mu\text{M}$  of VV1, an inactive isomer of 2C. The other coverslip was treated with  $2\ \mu\text{M}$  of 2C and then fixed after 24 hours in 4% paraformaldehyde 0.15% and picric acid (the fixation was performed also for the negative control). After treatment with 0.1% Triton X 100 and 1% BSA to promote the membrane permeation, fixed cells were treated with the primary antibody for  $\beta$ -tubulin at a concentration of  $10\ \mu\text{g/ml}$  for one hour at room temperature. Subsequently, an anti-rabbit secondary antibody labeled with a green fluorophore (Alexa Fluor® 488,  $\lambda$  emission= 519 nm, Thermo Fisher Scientific, Waltham, Massachusetts, USA) was used at a concentration of  $2\ \mu\text{g/ml}$  for 45 minutes to detect the primary antibody/ $\beta$ -tubulin complex in fixed cells (**Figure 3.13**). After the treatment of cell lines with DAPI, the coverslips were assembled on microscope slides and left at  $4\ ^\circ\text{C}$  overnight. Finally, cell lines images were taken at the fluorescence microscope (Leica DM2000) at a magnification of 20X and 40X.

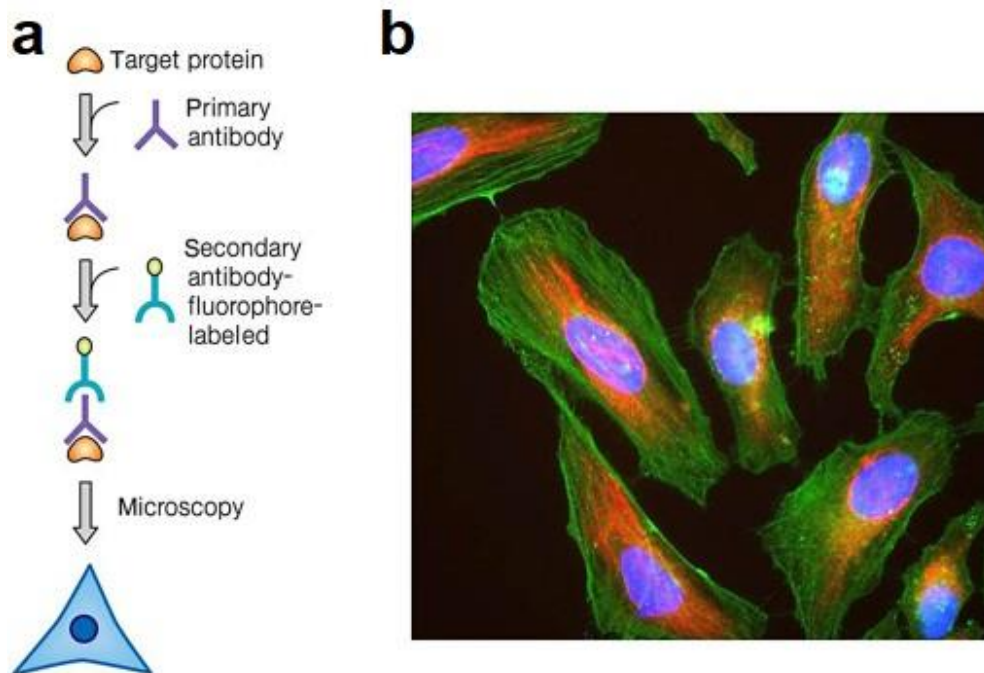


**Figure 3.13:** a) A diagram illustrating the procedure involved in the immunofluorescence assay (IFA). b) example of IFA on HeLa cells, in green the actin, in red the vimentin and in blue the DNA. Adapted from Wang-Shick Ryu [183].

#### 3.4.4.2 F-Actin

Since 2C indirectly activates Cofilin-1, a protein that binds and depolymerizes filamentous F-actin, a fluorescence staining of the Actin network was performed using phalloidin conjugated with the red-orange fluorescent dye tetramethylrhodamine (TRITC,  $\lambda$  emission= 565 nm, ActinRed™ 555, Thermo Fisher Scientific, Waltham, Massachusetts, USA). The phalloidin is a mycotoxin isolated from the deadly *Amanita phalloides* “death cup” mushroom, which binds with high affinity the F-actin. For this reason, this molecule is commonly used in biomedical research to visualize the Actin network [135].

Similarly for  $\beta$ -tubulin immunofluorescence, the OVCAR4, HEY and TYKNU cell lines were split in two populations for the treatment with 2  $\mu$ m of 2C and VV1. After 24 hours, the cell lines were fixed, permeabilized and treated with 2 drops of phalloidin-TRITC for ml of media. After an incubation of 30 minutes and washes with PBS 1X, cell lines images were taken at the fluorescence microscope (Leica DM2000) at 20X and 40X magnification.

#### 3.4.4.3 Analysis of Cytoskeleton Distribution

The analysis of F-actin/ $\beta$ -tubulin images were carried out by a Fiji Macro of ImageJ able to analyze the intensity and the distribution of fluorescence inside cells. As first step, the Macro segments cells to calculate the average fluorescence inside the selected area. Then, the Macro draws a line that passes for the cell centroid and calculates the fluorescence intensity over it. In this way it is possible to observe the F-actin/ $\beta$ -tubulin distribution in cross-sections. Moreover, the intensity data over the line are divided in 10 equal sections (called bins) and the average fluorescence was calculated for each of them. This renders the analysis independent from changes due to cell size and/or shape [136] (**Figure 3.14**).

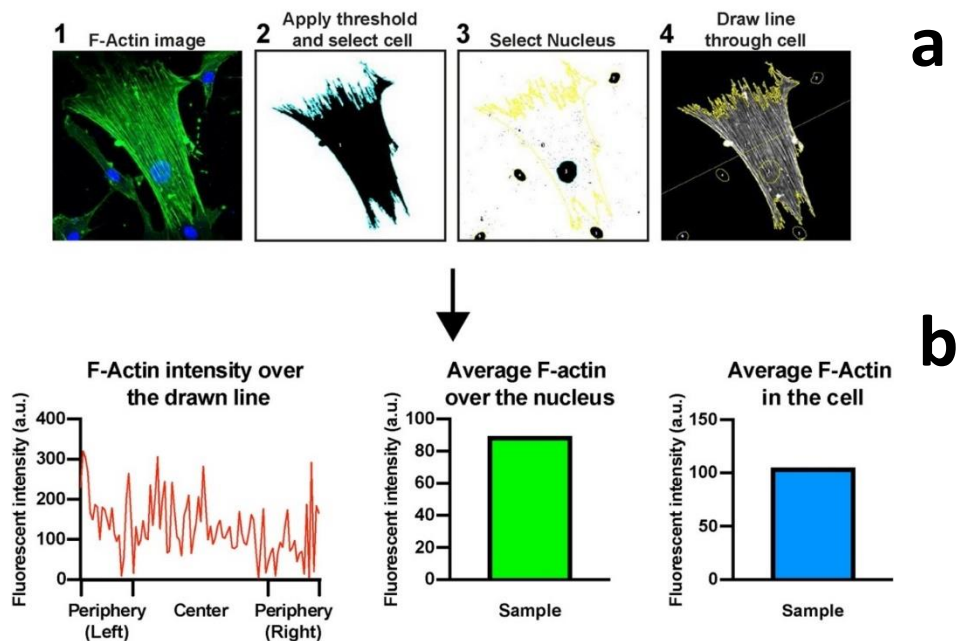


**Figure 3.14:** Schematic diagram of Macro working principle. a) different step of the cell image processing; b): output of macro's analysis for fluorescence intensity on intersecting line (left), nucleus (middle) and cell (right). Adapted from Zonderland J. [136].

### 3.5 Statistical Analyses

All data in this thesis were expressed as mean  $\pm$  standard deviation. Since the heterogeneous distribution pattern of tested samples, the distribution-free nonparametric Mann-Whitney and Kruskal Wallis tests were run to assess the statistical relevance [184]. Similarly, pairwise correlation analyses were carried out using the Spearman correlation coefficient  $r_s$  [185]. For each correlation analysis was reported also the 95% confidence interval with the lower and upper confidence limits. Data distribution was assessed by the Anderson-Darling test, a distribution-free omnibus test alternative to the Kolmogorov-Smirnov (one of the most used test for the normality distribution assessment). Regard the latter, which required a huge sample size, the Anderson-Darling test show a decent sensitivity also with a smaller sample size [186]. The analysis of time series trend was performed by the nonparametric Mann-Kendall test, which return an eventual statistically significant decreasing or increasing trend in a temporal data set [187]. The fluorescence intensity was reported as the mean pixel intensity (m.p.i.), that is the sum of the color intensity values of all pixels in the selected area divided by the number of pixels. All p-values values  $<0.05$  were considered statistically significant. Statistical analyses were

carried out using GraphPad Prism 9 (GraphPad Software, Inc., San Diego, CA, USA), R 4.04 and Origin 2021 (OriginLab Corporation, Northampton, Massachusetts).

## 4. Results

### 4.1 Cell lines Classification

#### 4.1.1 Histological Classification

The analysis of the molecular properties of the cell lines, aimed at finding the EOC subtype genomic profile resulted in the following classification.

##### 4.1.1.1 CAOV3

The molecular profile was characterized by different genetic alterations associated to HGSOC, such as mutations of TP53 (non-sense mutation p.Q136\*) and ATM (insertion with frame shift, p.K1903fs) and amplification of Notch3 and PIK3CA (see chapter 1.2.4) (**Table 4.1**). These features, the high copy number variation rate (CCLE reports 3236 genes with copy number alterations) and the low mutation burden (only 441 mutations have been recognized by CCLE) make the CAOV3 cell line a good model of HGSOC.

##### 4.1.1.2 HEY

The presence of TP53 wild-type, mutations of KRAS (missense mutation, p.G12D) and BRAF (missense mutation, p.G464E) and overexpression of IGF1 make the HEY cell line a model that well resemble the LGSOC (**Table 4.1**). This consideration was further proved by the high resistance of this cell line to cis-platin treatment and the relatively low copy number variation rate (652 genes with copy number variations have been reported in CCLE panel) (see chapter 1.1.4).

##### 4.1.1.3 IGROV1

The analysis of molecular features of IGROV1 cell line indicated a very heterogeneous profile including HGSOC hallmarks (TP53 mutated, BRCA2 mutated, disfunction in repair DNA pathway), ENOC hallmarks (ARID1A mutated, PIK3CA mutated, PTEN mutated, KMTB-D mutated) and CCOC hallmarks (ARID1A-1B

mutated, PIK3CA mutated, SMARCA4 mutated) (**Table 4.1**). Despite these features, the presence of microsatellite instability, mutation of POLE, low copy number variation rate (only 93 genes with copy number alterations) and high mutational burden (4224 mutations detected by CCLE panel) indicated the molecular profile of IGROV1 cell line as extremely similar to ENOC with hypermutated phenotype (see chapter 1.1.6).

#### *4.1.1.4 OAW42*

Despite the serous origin of OAW42 cell line, its molecular profile did not show any hallmark of HGSOC or LGSOC. The mutations of ARID1A (deletion with frameshift, p.P559fs; insertion with frameshift, p.F1118fs) and PIK3CA (missense mutation, p.H1047L) are prominent biomarkers of ENOC and CCOC (**Table 4.1**). Since these hallmarks have a high incidence in CCOC (50%) and considering the relapse and poor outcome of patient from which this cell line was established (she died 1 month after paracentesis, [111]), the OAW42 can be indicated as a good model of CCOC relapsed (see chapter 1.1.5).

#### *4.1.1.5 OVCAR4*

The most important molecular aberrations found in this cell line were amplification of CCNE1, mutations in TP53 (missense mutation, p.L130V), BRCA2 (missense mutation, p.P2505L), CDKN2A (missense mutation, p.S21T) and different disfunctions in DNA repair mechanisms (**Table 4.1**). Although mutated CDKN2A is a key biomarker of MOC, these features and the high copy number variation rate (2449 genes with copy number alterations according to CCLE panel) make the OVCAR4 an excellent model of HGSOC.

#### *4.1.1.6 OVCAR8*

The molecular profile of this cell line is not easy to interpret. Mutations in TP53 (Splice site alteration), in some genes of the DNA repair pathway and in Notch1 (missense mutation, p.P1486L) indicate OVCAR8 as a model of HGSOC, but the simultaneous mutation of TP53 and KRAS (missense mutation, p.P121H) did not allow excluding OVCAR8 cell line as a good model of MOC (**Table 4.1**). However, according to the prior classification of this cell line [137], to the high age at diagnosis of original patient

and to the high copy variation rate (1687 genes reported by CCLE) OVCAR8 cell line was more likely a model of HGSOC.

#### 4.1.1.7 SKOV3

The molecular profile of SKOV3 is quite similar to IGROV1 one. There were molecular hallmarks of HGSOC (mutations in TP53 and ATM), ENOC (mutations in ARID1A, PIK3CA, CTNNB1 and POLE) and CCOC (mutations in ARID1A, PIK3CA and TERT). Unlike IGROV1, the definitive establishment of this cell line as model of ENOC with hypermutated phenotype was more difficult due to its high copy number variation rate (1771 copy number alteration events in CCLE panel), relatively low mutational burden (912 mutations recognized in SKOV3 versus 4224 mutations in IGROV1) and poor alteration of DNA repair mechanism. However, the cis-platin resistance, TERT mutation and certain key hallmarks of ENOC and CCOC supported the SKOV3 cell line as a model of a ENOC associated to clear cells or a CCOC/ENOC mix (see chapter 1.1.5 and 1.1.6) (**Table 4.1**).

#### 4.1.1.8 TYKNU and TYKNU CpR

The molecular profile of TYKNU and TYKNU CpR cell lines was heterogeneous as concern the classical hallmarks of EOC subtypes. It was characterized, indeed, by mutations in TP53 (missense mutation, p.R175H), in NRAS (double missense mutation, p.Q61K – p.G12D) and in ARID1A (deletion with frameshift, p.GGGP91fs) (**Table 4.1**). The young age at diagnosis of the original patient, the relatively low copy number variation rate (778 genes have alterations in copy number according to CCLE panel) and the functional DNA repair pathway confirmed the prior classification of these cell lines as a poor HGSOC model [138]. These features and the double mutation in NRAS could suggest TYKNU and TYKNU cell lines as models of LGSOC, but the mutation of ARID1A and TP53 did not allow automatically excluding the hypothesis of a good MOC model, which seems to be more likely.

<b>Cell Line</b>	<b>Genetic Alterations</b>	<b>Histological Classification</b>
<b>TYKNU/TYKNU CpR</b>	<i>TP53 mut, NRAS mut, ARID1A mut, USH2A mut, HMCN1 mut</i>	<i>MOC</i>
<b>OAW42</b>	<i>PIK3CA mut, ARID1A mut</i>	<i>CCOC</i>
<b>SKOV3</b>	<i>TP53 mut, PIK3CA mut, NOTCH1 mut, ATM mut, NF1 mut, ARID1A mut, POLE mut, NEB mut</i>	<i>ENOC/CCOC</i>
<b>IGROV1</b>	<i>TP53 mut, EMSY mut, RB1 mut, PIK3CA mut, PTEN mut, RAD 50 mut, ATM mut, FANCA mut, CHRN4 mut, TNK1 mut, USP9X mut, ARID1A-B mut, ERBB3 mut, PIK3R2 mut, SMARC4A mut, CTNNB1 mut, KMT2B-D mut, POLE mut, BCOR mut, NEB mut, USH2A mut, HMCN1 mut, ZNF469, ABCA mut</i>	<i>ENOC with hypermutated phenotype</i>
<b>HEY</b>	<i>Notch 3 mut, KRAS mut, IGF1 high, BRAF mut</i>	<i>LGSOC</i>
<b>OVCAR4</b>	<i>TP53 mut, CDKN2A del, CCNE1 amp, Notch1 amp, RAD50 mut, ATM mut, POLE mut, SPOP mut, FCGB mut</i>	<i>HGSOC</i>
<b>OVCAR8</b>	<i>TP53 mut, Notch1 amp, ATM mut, ERBB2 mut, KRAS mut, KMT2B mut, USH2A mut, HMCN1 mut</i>	<i>HGSOC</i>
<b>CAOV3</b>	<i>TP53 mut, PIK3CA mut, Notch 3 amp, ATM mut, DNAH14 mut</i>	<i>HGSOC</i>

**Table 4.1:** Genetic alterations and histological classification of each cell lines. Mut: mutated, High: over expressed, Amp: amplified, Del: deleted.

#### 4.1.2 Morphological Classification

The morphological classification was carried out by achievement of the aspect ratio (AR), circularity and area of at least 30 cells for each cell line. The results showed an epithelial morphology for all HGSOC cell lines (OVCAR8, OVCAR4 and CAOV3), while the ENOC ones, SKOV3 and IGROV1 displayed respectively a fibroblastic-like and an epithelial-like morphology (**Table 4.2**). It was not possible to speculate about possible correlations between histology and morphology of CCOC, LGSOC and MOC cell lines since there was only one representative for these histological subtypes (TYKNU CpR is a subline of TYKNU).

The analysis of AR values showed a higher standard deviation for cell lines with fibroblastic morphology (**Table 4.2**), which suggests a high variability in elongation. This was probably due to the different degrees of branching and multipolarity characterizing these cell lines. The TYKNU CpR cells did not show relevant difference in elongation than TYKNU ones.

As concern the area of cell lines, the TYKNU CpR cells had a relevant higher average area than the TYKNU ones (**Table 4.2**), which was probably due to the highest percentage of large cells [116] [117].

<b>Cell Line (Histology)</b>	<b>Circularity</b>	<b>Aspect Ratio</b>	<b>Mean Area (<math>\mu\text{m}^2</math>)</b>	<b>Morphology</b>
<b>TYKNU (MOC)</b>	$0.43 \pm 0.21$	$3.44 \pm 1.49$	$753.05 \pm 384.59$	<i>Fibroblastic</i>
<b>TYKNU CpR (MOC)</b>	$0.44 \pm 0.17$	$3.11 \pm 1.07$	$2431.54 \pm 1161.54$	<i>Fibroblastic</i>
<b>OAW42 (CCOC)</b>	$0.89 \pm 0.03$	$1.37 \pm 0.16$	$450.45 \pm 58.77$	<i>Epithelial</i>
<b>SKOV3 (ENOC)</b>	$0.46 \pm 0.13$	$3.26 \pm 0.63$	$1049.93 \pm 307.88$	<i>Fibroblastic</i>
<b>IGROV1 (ENOC)</b>	$0.94 \pm 0.01$	$1.14 \pm 0.10$	$1051.79 \pm 155.32$	<i>Epithelial</i>
<b>HEY (LGSOC)</b>	$0.27 \pm 0.03$	$5.25 \pm 1.51$	$889.73 \pm 337.19$	<i>Fibroblastic</i>
<b>OVCAR4 (HGSOC)</b>	$0.81 \pm 0.15$	$1.41 \pm 0.20$	$855.14 \pm 246.73$	<i>Epithelial</i>
<b>OVCAR8 (HGSOC)</b>	$0.74 \pm 0.13$	$1.91 \pm 0.42$	$1269.08 \pm 279.54$	<i>Epithelial</i>
<b>CAOV3 (HGSOC)</b>	$0.86 \pm 0.08$	$1.43 \pm 0.37$	$652.23 \pm 141.21$	<i>Epithelial</i>

**Table 4.2:** Shape factors (Circularity, Aspect Ratio, Area) and Morphological classification of each cell line.

## 4.2 Mechanical Characterization

### 4.2.1 Average Young's Modulus

The average Young's Modulus (E) was obtained for each cell lines by the analysis of the mechanical properties of about 100 cells. These stiffness values are reported in a box-and-whisker plot to observe possible similarities or differences among cell lines (**Figure 4.1**). The average Young's Modulus and standard deviations are instead summarized in **Table 4.3**.

It was possible to observe a widespread distribution of the mean Young's Modulus among cell lines (from  $0.29 \pm 0.12$  kPa for TYKNU to  $1.84 \pm 0.67$  kPa for CAOV3) with a statistically significant overall difference, as established by Kruskal-Wallis test ( $p < 0.0001$ ). Moreover, the average Young's Modulus of TYKNU CpR cells was significantly higher than TYKNU ones (Mann-Whitney test,  $p < 0.0001$ ).

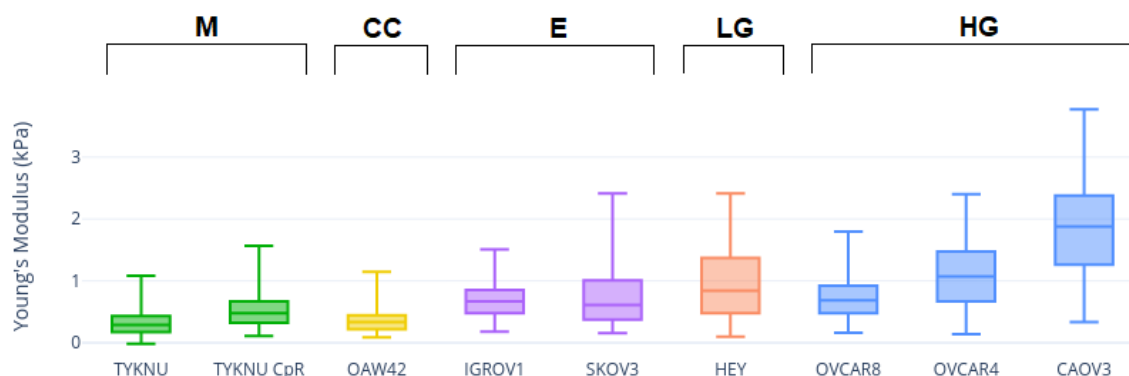


**Figure 2.1:** Box-and-whisker plots of stiffness of single cells for each cell lines. M: Mucinous, CC: Clear cells, E: Endometrioid; LG: Low grade serous; HG: High grade serous.

The mean Young's modulus of HGSOE cell lines was highly heterogeneous (OVCAR8:  $0.58 \pm 0.28$  kPa; OVCAR4:  $1.13 \pm 0.50$  kPa; CAOV3:  $1.84 \pm 0.67$  kPa), while as concern the ENOC cell lines the average stiffness was almost similar (SKOV3:  $0.69 \pm 0.40$  kPa; IGROV1:  $0.66 \pm 0.21$  kPa).

<b>Cell line (Sample size)</b>	<b>Average Young's Modulus (E) (kPa)</b>	<b>Standard Deviation (kPa)</b>
<b>TYKNU (100)</b>	<b>0.28</b>	<b>0.12</b>
<b>TYKNU CpR (102)</b>	<b>0.52</b>	<b>0.23</b>
<b>OAW42 (97)</b>	<b>0.37</b>	<b>0.13</b>
<b>IGROV1 (103)</b>	<b>0.66</b>	<b>0.21</b>
<b>SKOV3 (107)</b>	<b>0.69</b>	<b>0.40</b>
<b>HEY (117)</b>	<b>0.96</b>	<b>0.58</b>
<b>OVCAR8 (103)</b>	<b>0.58</b>	<b>0.28</b>
<b>OVCAR4 (105)</b>	<b>1.13</b>	<b>0.50</b>
<b>CAOV3 (94)</b>	<b>1.84</b>	<b>0.67</b>

**Table 4.3:** Average Young's Modulus and corresponding standard deviation of each cell line, with the number of analyzed cells in brackets.

The analysis of Young's Modulus in function of the histological classification showed statistically significant differences among each pair of histological subtypes, excepted for MOC vs CCOC and LGSOC vs HGSOC (Mann-Whitney test) (**Table 4.4**). Moreover, this analysis showed a higher stiffness for the serous cell lines (HGSOC and LGSOC) with respect of other EOC subtypes (**Figure 4.2**).



**Figure 4.2:** Box-and-whisker plot representing the stiffness of single cells for each EOC subtypes. MOC: Mucinous Ovarian Cancer, ENOC: Endometrioid Ovarian Cancer, CCOC: Clear Cells Ovarian Cancer, LGSOC: Low Grade Serous Ovarian Cancer, HGSOC: High Grade Serous Ovarian Cancer.

<i><b>EOC subtype pairs</b></i>	<i><b>Mann-Whitney test (p-value)</b></i>
<i><b>MOC vs ENOC</b></i>	<i><b>&lt;0.00001</b></i>
<i><b>MOC vs CCOC</b></i>	<i><b>0.9124</b></i>
<i><b>MOC vs LGSOC</b></i>	<i><b>&lt;0.00001</b></i>
<i><b>MOC vs HGSOC</b></i>	<i><b>&lt;0.00001</b></i>
<i><b>ENOC vs CCOC</b></i>	<i><b>&lt;0.00001</b></i>
<i><b>ENOC vs LGSOC</b></i>	<i><b>0.049</b></i>
<i><b>ENOC vs HGSOC</b></i>	<i><b>&lt;0.00001</b></i>
<i><b>CCOC vs LGSOC</b></i>	<i><b>&lt;0.00001</b></i>
<i><b>CCOC vs HGSOC</b></i>	<i><b>&lt;0.00001</b></i>
<i><b>LGSOC vs HGSOC</b></i>	<i><b>0.07</b></i>

**Table 4.4:** Results of the Mann-Whitney test for each EOC histological subtype.

Finally, cells with epithelial morphology had a tendentially higher Young's Modulus than ones with fibroblast morphology (Mann-Whitney test,  $p < 0.00001$ ).

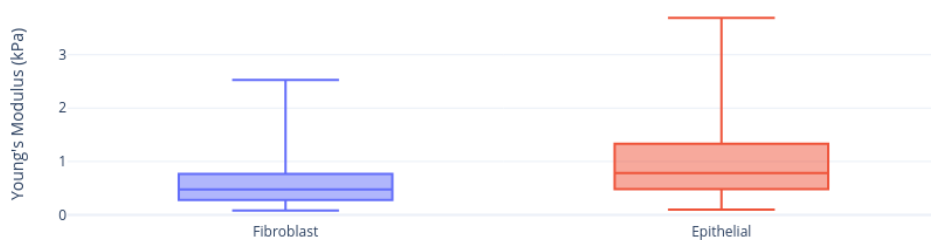


**Figure 4.3:** Box-and-whisker plot representing the stiffness of single cells for the epithelial and fibroblast morphology.

## 4.2.2 Young's Moduli Distribution

The distribution modality of Young's Moduli of single cells was obtained for each cell line by the Anderson-Darling test. The results indicated a Gaussian distribution for TYKNU, OAW42, IGROV1 and CAOVS3 cell lines and a non-normal distribution for SKOV3, TYKNU CpR, OVCAR8, OVCAR4 and HEY cell lines (**Table 4.5**). As concern the latter, a statistical deconvolution procedure [139] applied to their Young's Moduli distribution histograms has pointed up a bimodal pattern characterized by two different peaks (**Figure 4.4**). This could indicate the presence of two subpopulations with different mechanical properties. The analysis of this bimodal pattern highlighted a highest-stiffness population usually most widely distributed than the lowest-stiffness one (except for TYKNU CpR) (**Table 4.6**).

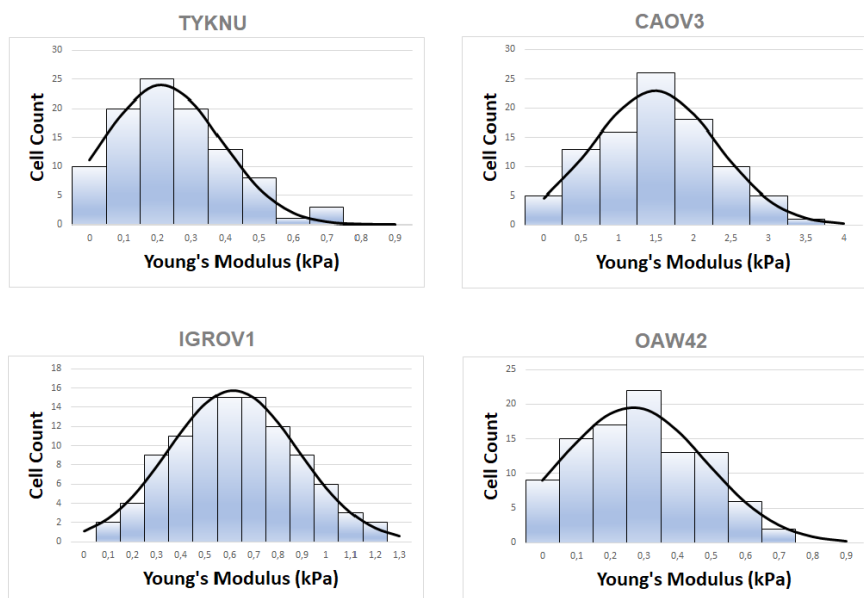
Cell line	Histology	Morphology	Anderson-Darling (p-value)	Distribution pattern
TYKNU	MOC	Fibroblastic	0.09	Gaussian
TYKNU CpR	MOC	Fibroblastic	0.01	Non-Gaussian
OAW42	CCOC	Epithelial	0.503	Gaussian
IGROV1	ENOC	Epithelial	0.321	Gaussian
SKOV3	ENOC	Fibroblastic	0.0003	Non-Gaussian
HEY	LGSOC	Fibroblastic	0.008	Non-Gaussian
OVCAR8	HGSOC	Epithelial	0.0002	Non-Gaussian
OVCAR4	HGSOC	Epithelial	0.01	Non-Gaussian
CAOV3	HGSOC	Epithelial	0.526	Gaussian

**Table 4.5:** Results of the Anderson-Darling test on Young's modulus of single cells for each cell line. In table are reported the morphology and the histological classification of each cell line.

The stiffness distribution patterns highlighted another difference between TYKNU and TYKNU CpR cell lines: the latter had indeed a bimodal pattern while TYKNU was characterized by a Gaussian distribution. Moreover, the mean Young's Modulus of TYKNU CpR lowest-stiffness peak was quite similar to the TYKNU one ( $0.24 \pm 0.12$  kPa for TYKNU CpR and  $0.29 \pm 0.12$  kPa for TYKNU). This could indicate the highest-stiffness peak presence as consequence of the treatment of the cis-platinum sensible cell line (TYKNU) with stepwise increasing concentration of cis-platinum to obtain the corresponding drug resistant subline (TYKNU CpR).

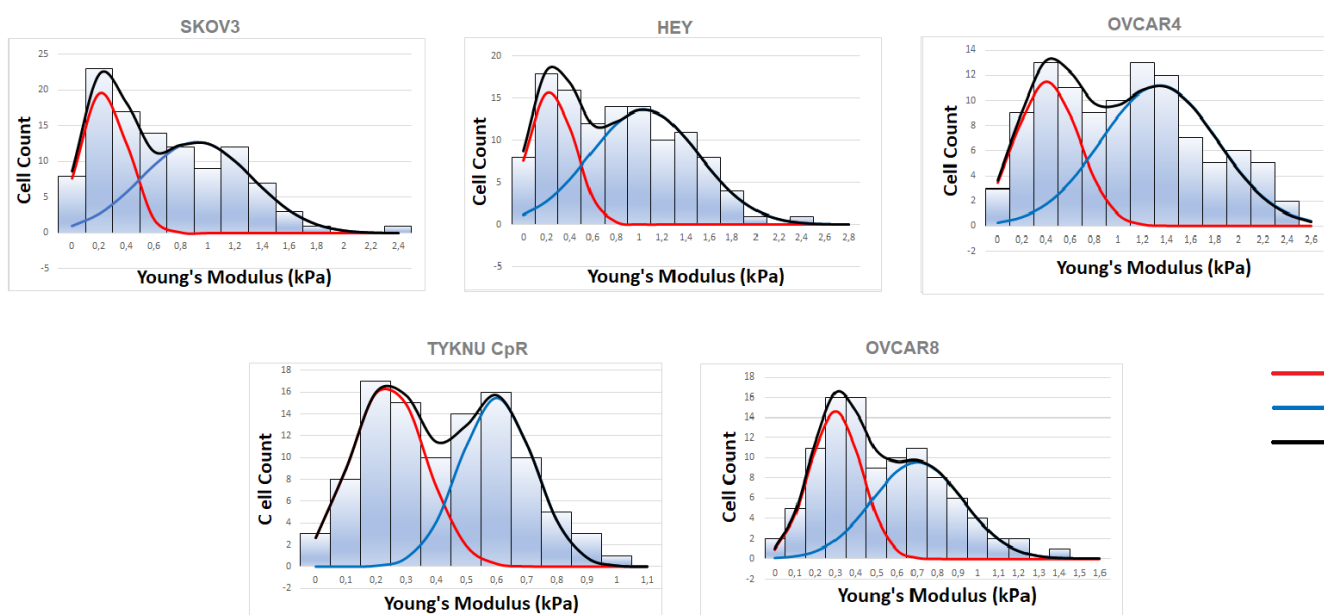
From a histological point of view, both HGSOC cell lines (OVCAR4 and OVCAR8 have a bimodal pattern, while CAOV3 has a Gaussian distribution) and ENOC cell lines (bimodal for SKOV3 and Gaussian for IGROV1) were heterogeneous. As concern the cell morphology, the fibroblastic cell lines had tendentially a bimodal distribution as three out of four fibroblastic cell lines (TYKNU CpR, HEY and SKOV3) were characterized by this stiffness distribution pattern.

a



— FIT

b



— Pop #1  
 — Pop #2  
 — FIT

**Figure 4.4:** a) Histograms of cell lines with Gaussian distribution; b) Histograms of cell lines with bimodal distribution. In red the population with the lowest-stiffness peak, in blue the population with the highest-stiffness peak. Pop#1: lowest-stiffness population, Pop#2: highest stiffness population. FIT: resulting fit curve of histogram.

Cell line	E Pop#1 (kPa)	E Pop#2 (kPa)	E Pop#2 – E Pop#1 (kPa)
SKOV3	$0.23 \pm 0.17$	$0.92 \pm 0.41$	0.69
HEY	$0.24 \pm 0.20$	$1.04 \pm 0.47$	0.8
OVCA4	$0.41 \pm 0.26$	$1.34 \pm 0.48$	0.93
TYKNU CpR	$0.24 \pm 0.12$	$0.60 \pm 0.12$	0.36
OVCA8	$0.3 \pm 0.13$	$0.70 \pm 0.22$	0.40

**Table 4.6:** Average Young's Modulus (E) and standard deviation of two populations of each cell line with bimodal distribution. The E Pop#2 – E Pop#1 values were calculated to observe the distance in term of stiffness between the two populations. Pop#1: lowest-stiffness population, Pop#2: highest stiffness population.

### 4.2.3 Effects of Variation in Experimental Set-up

The IGROV1 cell line was cultured in RPMI 1640 and DMEM:F12 1:1 (nutrients more concentrated) to observe the effects of different medium compositions on mechanical properties. The AFM analysis pointed out a significant higher mean Young's Modulus for IGROV1 cells cultured in RPMI 1640 than the same ones grown in DMEM:F12 (Mann-Whitney test,  $p = 0.01$ ) (**Figure 4.5**).

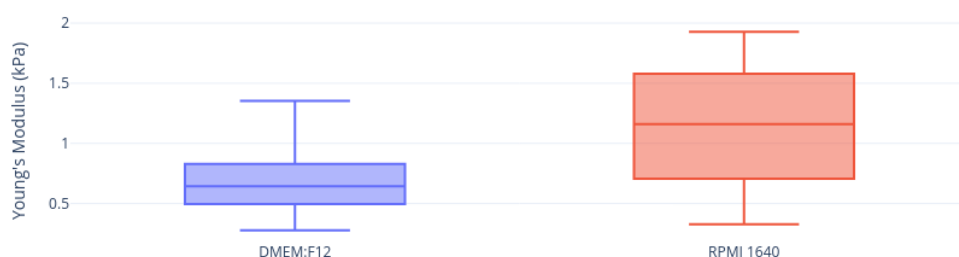


**Figure 4.5:** Box-and-whisker plot representing the stiffness of single cells for IGROV1 cultured in DMEM:F12 and RPMI 1640. Average Young's Modulus of IGROV1 in DMEM:F12 =  $0.75 \pm 0.25$  kPa; Average Young's Modulus of IGROV1 in RPMI 1640 =  $1.13 \pm 0.53$  kPa.

Then, TYKNU cells were culture in EMEM with two different concentrations of FBS: 10% and 20%. The analysis was aimed at observing the contribution of FBS components on the mechanical behavior. The results showed that cells grown in medium with higher FBS concentration have a higher mean stiffness than the one grown in 10% FBS (Mann-Whitney test,  $p = 0.00001$ ) (**Figure 4.6**).



**Figure 4.6:** Box-and-whisker plot representing the stiffness of single cells for TYKNU cultured with 10% FBS and 20% FBS. Average Young's Modulus TYKNU with FBS 10% =  $0.29 \pm 0.18$  kPa; Average Young's Modulus TYKNU with FBS 20% =  $0.65 \pm 0.22$  kPa.

To understand the effects of neighboring cells connections on mechanical properties of the tested cell (an important factor to consider in cell lines with epithelial morphology where it is not possible to have completely separated cells), IGROV1 cells were cultured for three days and one week to analyze cells from small cluster (after three days) and from a continuous layer (after one week). The mechanical characterization did not show any significant difference (Mann Whitney test,  $p = 0.08$ ) (**Figure 4.7**).



**Figure 4.7:** Box-and-whisker plot representing the stiffness of single cells for IGROV1 from small clusters and from a continuous layer. Average Young's Modulus IGROV1 from small cluster =  $0.6 \pm 0.24$  kPa; Average Young's Modulus IGROV1 from continuous layer =  $0.74 \pm 0.25$  kPa.

### 4.3 Metastatic Potential

Epithelial-mesenchymal transition (EMT) is an important step of the tumor invasion process, it is characterized by a cytoskeletal reorganization that can impact on the mechanical properties of cells. A migration assay was carried out for each cell line in order to associate the mechanical parameters to the metastatic potential of cell lines (see chapter 3.3) (**Figure 4.8**). The results of this assay are reported in **table 4.7** as average number of invasive cells for optical field.

Cell Line	Histology	Morphology	Distribution Pattern	Average Invasive Cells / Optical field
TYKNU	MOC	Fibroblastic	Unimodal	63 ± 22
TYKNU CpR	MOC	Fibroblastic	Bimodal	91 ± 22
OAW42	CCOC	Epithelial	Unimodal	17 ± 4
IGROV1	ENOC	Epithelial	Unimodal	8 ± 3
SKOV3	ENOC	Fibroblastic	Bimodal	125 ± 45
HEY	LGSOC	Fibroblastic	Bimodal	176 ± 26
OVCAR4	HGSOC	Epithelial	Bimodal	16 ± 4
OVCAR8	HGSOC	Epithelial	Bimodal	38 ± 24

**Table 4.7:** Mean number of an invasive cells / Optical field for each cell line with the corresponding histology, morphology and distribution pattern.

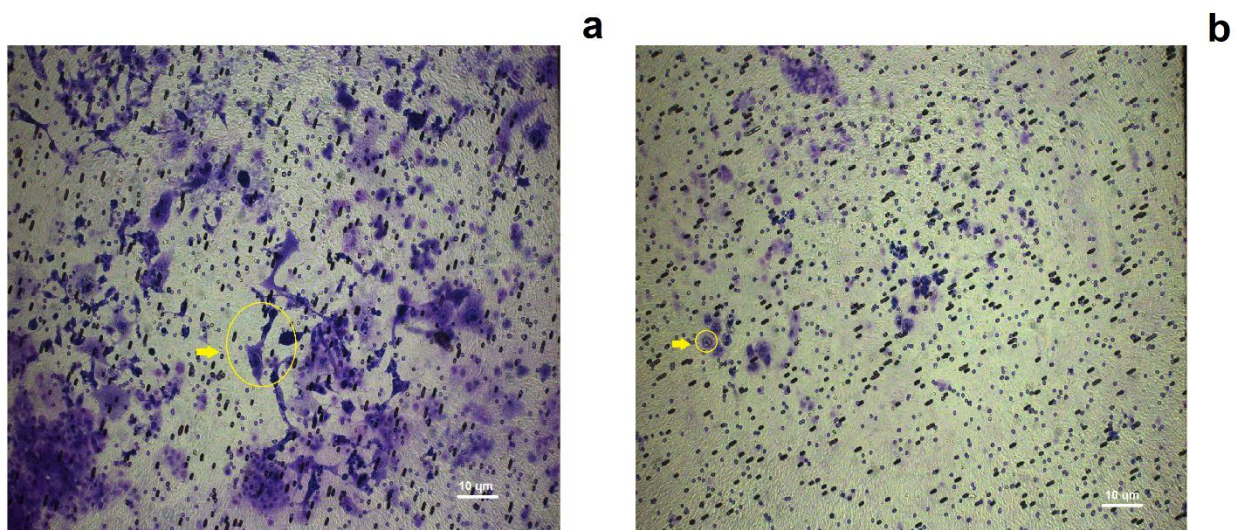


**Figure 4.8:** Representative images used for invasive cells count in TYKNU CpR (high metastatic potential) (a) and IGROV1 (low metastatic potential) (b). These images represent one of the three optical fields used for the count. In yellow circle, an example of the cell included in the count.

The analysis of invasion data in function of the mean Young's Modulus did not show any recognizable trend ( $rs: -0.05$ ;  $p: 0.45$ ;  $95\%CI [-0.68;0.73]$ ) (**Figure 4.9a**). On the contrary, considering only the lowest-stiffness population for cell lines with bimodal distribution, there was a strong negative correlation between the mean stiffness and the average number of invasive cells, as established by the Spearman's rank correlation coefficient ( $rs: -0.96$ ,  $p: 8.9 \cdot 10^{-5}$   $95\%CI [-0.99;-0.70]$ ) (**Fig 4.9b**). This suggests that the decrement stiffness was correlated to an increment of the metastatic potential.

With respect of the histological classification, the HGSOC cell lines had a lower average number of invasive cells (16 for OVCAR4 and 38 for OVCAR8) while the

ENOC ones resulted more variable (8 for IGROV1 and 125 for SKOV3) (**Figure 4.10a**).

From the morphological point of view, cell lines with fibroblast morphology were characterized by a remarkable higher number of invasive cells than ones with epithelial morphology. This was coherent with the EMT as a fundamental step of tumoral invasion as these cell lines had a mesenchymal-like morphology (**Figure 4.10b**).

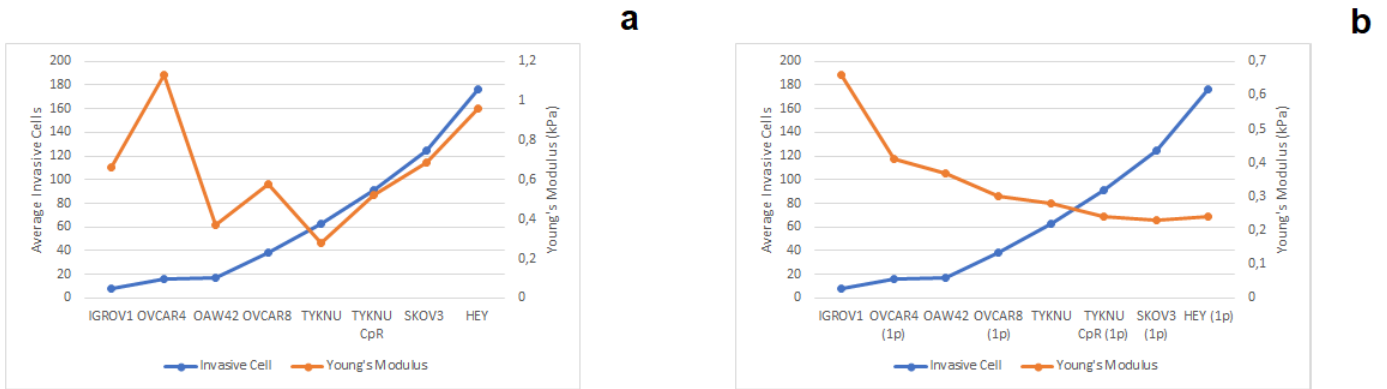


**Figure 4.9:** a) Average number of invasive cells in function of the average Young's Modulus; b) Average Number of Invasive cells in function of the average Young's Modulus, considering for cell lines with bimodal distribution only the lowest-stiffness population (indicated as 1p).

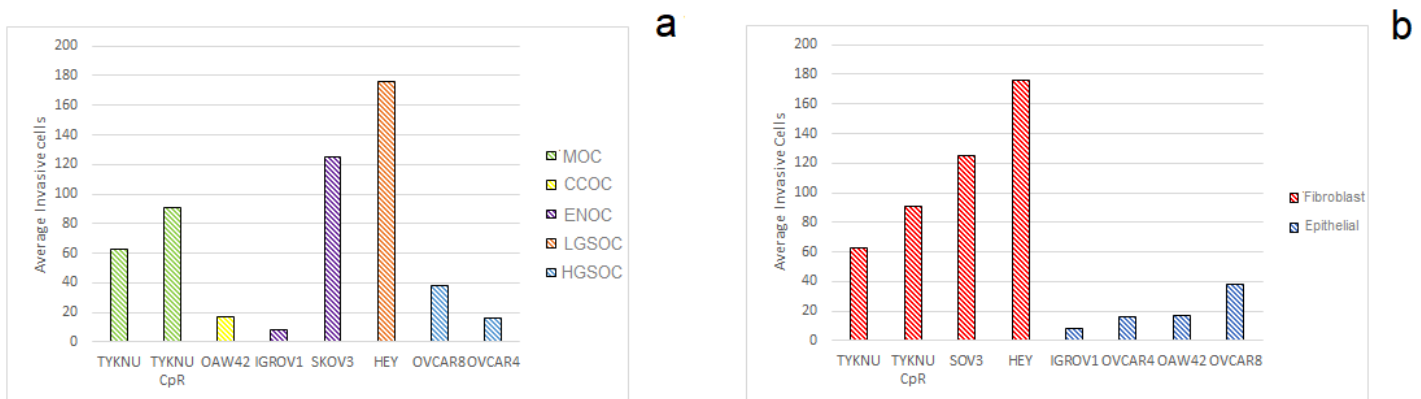


**Figure 4.10:** Average number of invasive cells of each cell lines in function of the histology (a) and the morphology (b).

## 4.4 2C Treatment

### 4.4.1 IC50 Assessment

To assess the mechanical properties as possible biomarker of drugs responsiveness, each cell line was treated with the 2C, an isopeptidase inhibitor used in tumor treatment, and then analyzed by AFM. Firstly, for each cell line the IC50 for the 2C was achieved. The analysis of this parameter showed a high difference in 2C sensitivity among cell lines (it ranged from 1.01  $\mu\text{M}$  for IGROV1 to 55  $\mu\text{M}$  for HEY) (**Table 4.8**). Moreover, the TYKNU CpR cell line was characterized by a higher resistance to 2C than the TYKNU one (IC50 was respectively 30.58  $\mu\text{M}$  and 7.86  $\mu\text{M}$ ). This could suggest a possible association between stiffness increment and 2C resistance. Despite this, the analysis of 2C in function of the average Young's Modulus did not return a remarkable correlation, as established by the Spearman's rank correlation coefficient (rs: 0.5, p: 0.08; 95%CI [-0.29;0.88]). Also considering only the highest-stiffness population for cell lines with bimodal distribution, the correlation remained weak (rs: 0.57, p: 0.04; 95%CI [-0.22;0.91]) (**Figure 4.11**).

Cell Line	Histology	Morphology	Distribution pattern	IC50 ( $\mu\text{M}$ )
TYKNU	MOC	Fibroblastic	Unimodal	7.86
TYKNU CpR	MOC	Fibroblastic	Bimodal	30.58
OAW42	CCOC	Epithelial	Unimodal	5.94
IGROV1	ENOC	Epithelial	Unimodal	1.01
SKOV3	ENOC	Fibroblastic	Bimodal	31.11
HEY	LGSOC	Fibroblastic	Bimodal	55
OVCAR8	HGSOC	Epithelial	Bimodal	12.69
OVCAR4	HGSOC	Epithelial	Bimodal	37.7
CAOV3	HGSOC	Epithelial	Unimodal	8.9

**Table 4.8:** IC50 for each cell line with the corresponding histology, morphology and distribution pattern.

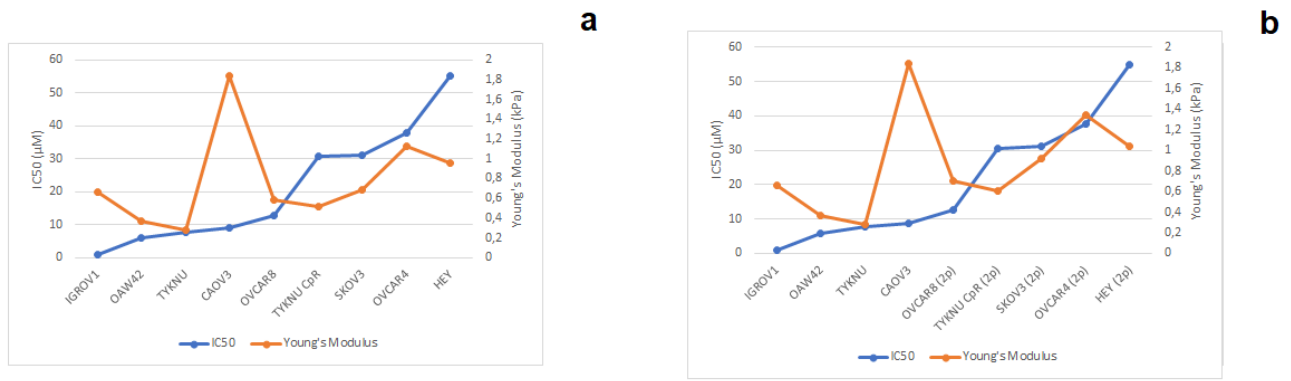


**Figure 4.11:** a) IC50 in function of the average Young's Modulus; b) IC50 in function of the average Young's Modulus, considering for cell lines with bimodal distribution only the highest-stiffness population (indicated as 2p).

In contrast, the analysis of IC50 in function of stiffness distribution pattern showed that the cell lines with bimodal distribution seem to be more resistant to 2C than those characterized by a Gaussian distribution. This can support for the presence of different cell populations with different stiffness properties and drug resistance (**Figure 4.12a**).

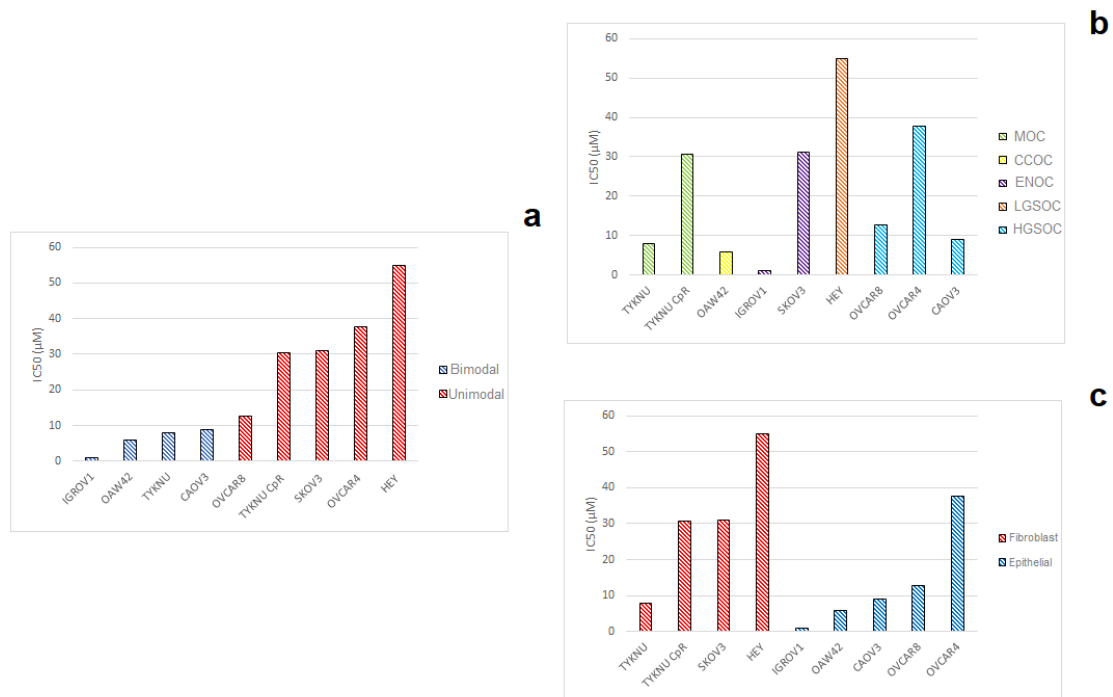


**Figure 4.12:** a) IC50 in function of the distribution patter. Cell lines with bimodal patter have a IC50 > 10 µM while the ones with Gaussian distribution have a IC50 < 10 µM; b) IC50 in function of histological classification; c) IC50 in function of cell morphology.

From a histological point of view, the sensitivity to 2C was heterogenous for both HGSOC cell lines (OVCAR8: 12.69 µM, OVCAR4: 37.7 µM, CAOY3: 8.9 µM) and ENOC ones (IGROV1: 1.01 µM, SKOV3: 31.11 µM) (**Figure 4.12b**). As concern the

morphology, cell lines with fibroblast morphology were tendentially resistant to 2C as three out of four cell lines have a high IC50 for this drug (**Figure 4.12c**).

#### 4.4.2 Average Young's Modulus after 2C Treatment

After the assessment of IC50, each cell line was dosed with 20  $\mu\text{M}$  of 2C and analyzed at AFM after 7 hours from treatment. The average Young's Modulus (E + 2C) was obtained by the analysis of at least 70 cells. The mechanical characterization showed that there is a decrease in the average Young's Modulus for all cell lines in comparison to untreated ones (**Figure 4.13**). This fits with the mechanism of action of 2C, which involves the depolymerization of F-actin network by activation of Cofilin-1 [106].



**Figure 4.13:** Box-and-whiskers representing the stiffness of single cells for each cell line before and after 2C treatment (in blue and red respectively).

The ratio between the average Young's Modulus before and after the 2C treatment ( $E - 2C / E + 2C$ ) was used to investigate the effects of this drug on cellular stiffness (**Table 4.9**). The analysis of this value in function of IC50 returned a moderate negative correlation as shown by Spearman's rank correlation coefficient (rs: -0.67; p: 0.02; 95%CI [-0.93;0.08]) (**Figure 4.14a**). Moreover, cell lines with bimodal pattern showed  $E - 2C / E + 2C$  values lower than the ones from cell lines with Gaussian distribution (**Figure 4.14b**).

Cell line	H	M	D	E - 2C	E + 2C	E - 2C / E + 2C	M-W test (p value)
TYKNU	MOC	F	U	0.28 ± 0.12	0.11 ± 0.02	2.54	<0.00001
TYKNU CpR	MOC	F	B	0.52 ± 0.23	0.28 ± 0.09	1.86	<0.00001
OAW42	CCOC	E	U	0.37 ± 0.13	0.16 ± 0.04	2.31	<0.00001
IGROV1	ENOC	E	U	0.66 ± 0.21	0.34 ± 0.16	1.94	<0.00001
SKOV3	ENOC	F	B	0.69 ± 0.4	0.41 ± 0.17	1.68	0.01
HEY	LGSOC	F	B	0.96 ± 0.58	0.53 ± 0.35	1.81	<0.00001
OVCAR8	HGSOC	E	B	0.58 ± 0.28	0.48 ± 0.18	1.16	0.04
OVCAR4	HGSOC	E	B	1.13 ± 0.50	0.76 ± 0.25	1.49	<0.00001
CAOV3	HGSOC	E	U	1.84 ± 0.67	0.82 ± 0.44	2.24	<0.00001

**Table 4.9:** Average Young's Modulus of each cell line before and after 2C treatment, ratio between these two values and results of Mann-Whitney test on the statistical significance of stiffness decrement after drug treatment. H: Histology, M: Morphology, D: Distribution patter, E - 2C (average Young's Modulus before 2C treatment), E + 2C (average Young's Modulus after 2C treatment), M-W test: Mann-Whitney test, F: Fibroblast, E: Epithelial, U: Unimodal, B: Bimodal.

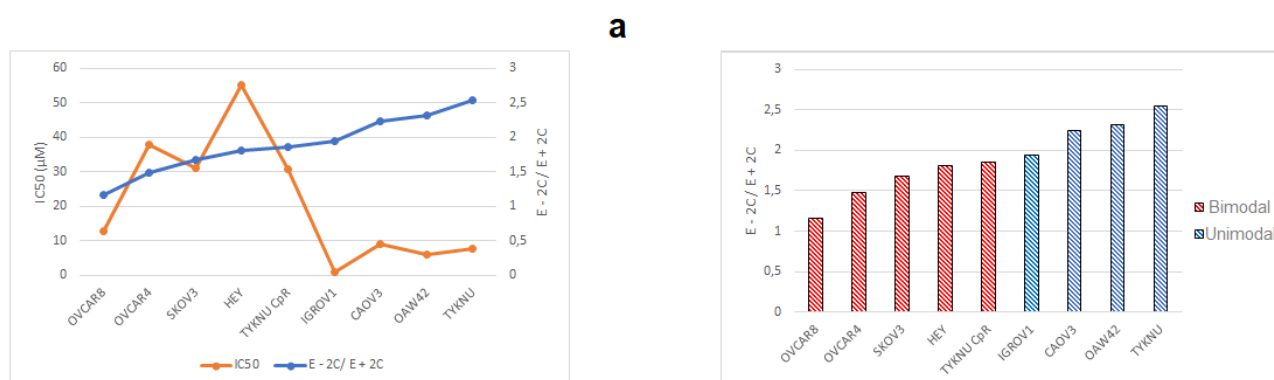


**Figure 4.14:** a) Ratio  $E - 2C / E + 2C$  in function of IC50, b) Ratio  $E - 2C / E + 2C$  in function of stiffness distribution pattern.

There did not seem to be a relationship between the stiffness decrement after 2C treatment and the histological and morphological classification of cell lines (**Figure 4.15**).

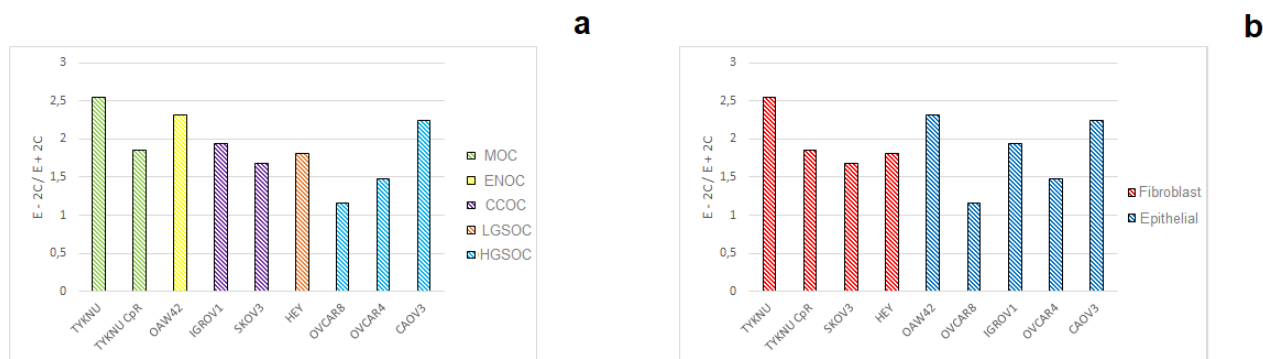


**Figure 4.15:** a) Ratio  $E - 2C / E + 2C$  in function of the histological classification, b) Ratio  $E - 2C / E + 2C$  in function of the cell morphology.

### 4.4.3 Young's Moduli Distribution after 2C Treatment

The distribution of Young's modulus of single cells was tested for each cell line treated with 2C (statistical test was the same used for not-treated cells; see chapter 4.2.2). The results showed the maintenance of Gaussian distribution after drug treatment for cell line characterized by unimodal pattern. For cell lines with bimodal distribution, for HEY, OVCAR4 and TYKNU CpR the distribution remained non-normal after 2C administration, while SKOV3 and OVCAR8 lost their bimodality assuming a Gaussian distribution (**Table 4.10**).

Statistical deconvolution procedure applied to the stiffness distribution histograms of HEY, OVCAR4 and TYKNU CpR cell lines treated with 2C pointed out the presence of the populations found in corresponding untreated ones (**Figure 4.16**). The analysis of distribution pattern of cell lines with bimodal distribution without 2C treatment, showed that untreated SKOV3 and OVCAR8 cell lines have a ratio between the peak height of lowest-stiffness and highest-stiffness population higher than the HEY, OVCAR4 and TYKNU CpR ones (**Table 4.11**). This suggests that the variation of the highest-stiffness population could impact on the response to 2C treatment.

Cell line	H	M	Distribution pattern – 2C	Anderson-Darling (p-value)	Distribution pattern + 2C
TYKNU	MOC	F	Gaussian	0.155	Gaussian
TYKNU CpR	MOC	F	Non-Gaussian	0.006	Non-Gaussian
OAW42	CCOC	E	Gaussian	0.118	Gaussian
IGROV1	ENOC	E	Gaussian	0.114	Gaussian
SKOV3	ENOC	F	Non-Gaussian	0.269	Gaussian
HEY	LGSOC	F	Non-Gaussian	0.0001	Non-Gaussian
OVCAR8	HGSOC	E	Non-Gaussian	0.558	Gaussian
OVCAR4	HGSOC	E	Non-Gaussian	0.002	Non-Gaussian
CAOV3	HGSOC	E	Gaussian	0.190	Gaussian

**Table 4.10:** Results of Anderson-Darling test on Young's Modulus of single cells for each cell line treated with 2C. H: histology, M: morphology, F: Fibroblast, E: Epithelial.

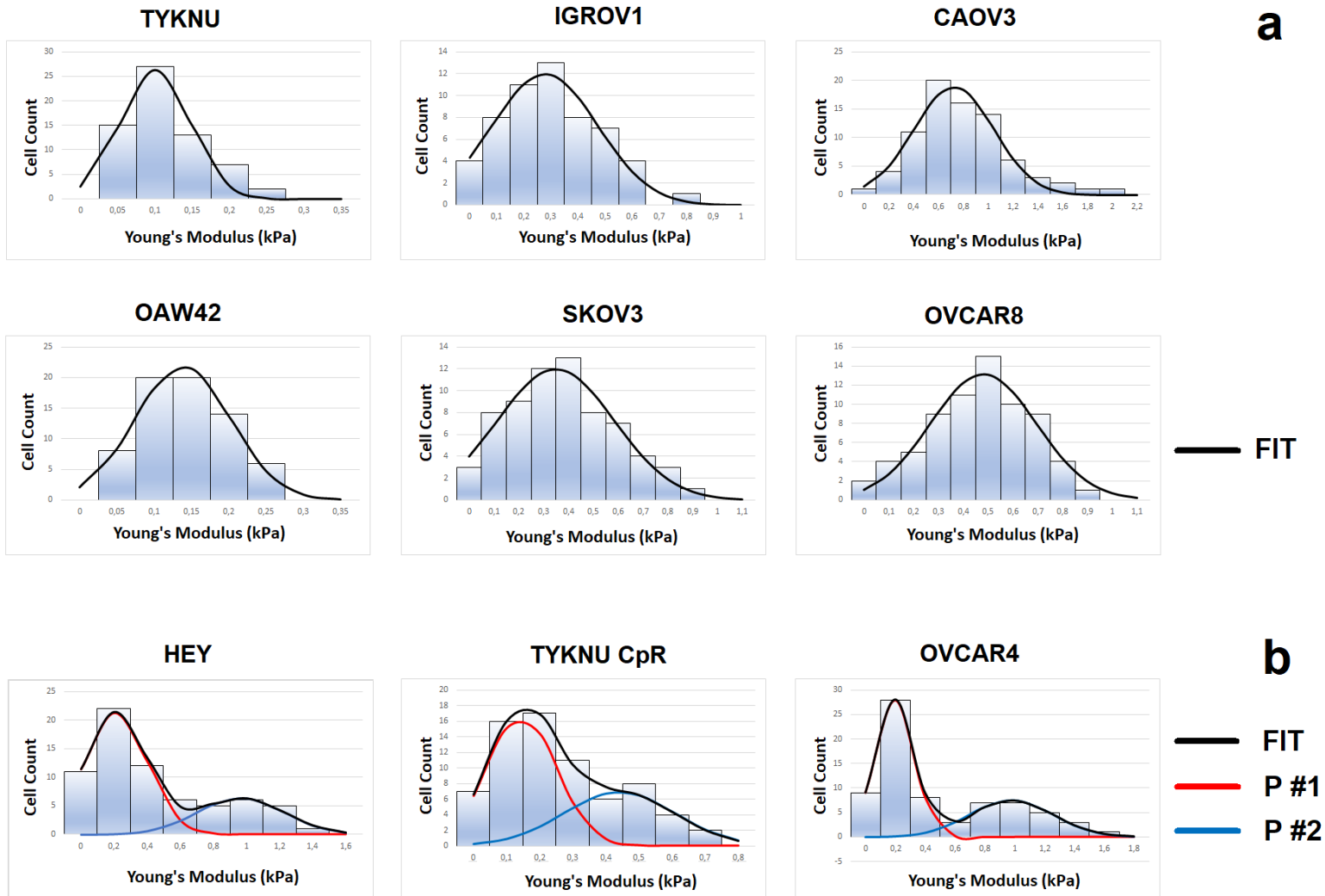


**Figure 4.16:** a) Histograms of cell lines with Gaussian distribution after 2C treatment; b) Histograms of cell lines with bimodal distribution after 2C treatment. In red the population with the lowest-stiffness peak, in blue the population with the highest-stiffness peak. FIT: resulting fit curve of histogram.

Cell line	Height Peak Pop #1 – 2C	Height Peak Pop #2 – 2C	Height Pop #1 / Height Pop #2	Distribution pattern + 2C
SKOV3	19.94	12.76	1.56	Gaussian
OVCAR8	14.61	9.64	1.51	Gaussian
TYKNU CpR	16.77	15.48	1.08	Bimodal
OVCAR4	11.47	11.16	1.03	Bimodal
HEY	15.99	13.65	1.17	Bimodal

**Figure 4.11:** Peak height for cells' populations characterizing cell lines with bimodal pattern. In table are reported also the ratio between two populations heights and the resulting distribution pattern after 2C treatment. Pop#1: lowest-stiffness population, Pop#2: Highest-stiffness population.

For TYKNU CPR, OVCAR4 and HEY cell lines, an increase in the ratio between the peak height of lowest-stiffness and highest-stiffness population after 2C treatment was observed (**Table 4.12**). Nevertheless, on average the Young's modulus related to the "softer" population of cells in the bimodal distribution decreased more than the one related to "stiffer" cells (**Table 4.12**). This observation further supports the "stiffer" population as prominent in response to 2C treatment. Moreover, in HEY also the lowest-stiffness population had a reduced decrement in average Young's Modulus, supporting for a possible contribution of both populations to 2C resistance (**Table 4.12**). Noteworthy, HEY cell line had the highest IC50 among the cell lines analyzed in this thesis.

		TYKNU CpR	OVCAR4	HEY
Height peak Pop #1	- 2C	16.77	11.47	15.99
	+ 2C	16.56	27.97	21.34
Height peak pop # 2	- 2C	15.48	11.16	13.65
	+ 2C	6.92	7.46	6.37
Average E Pop #1 (kPa)	- 2C	0.24 ± 0.12	0.41 ± 0.26	0.24 ± 0.20
	+ 2C	0.14 ± 0.10	0.19 ± 0.13	0.21 ± 0.19
Average E Pop #2 (kPa)	- 2C	0.60 ± 0.12	1.34 ± 0.48	1.04 ± 0.47
	+ 2C	0.44 ± 0.17	0.98 ± 0.28	0.96 ± 0.26
Height peak pop #1/ pop #2	- 2C	1.08	1.03	1.17
	+ 2C	2.39	3.75	3.35
Average E pop #1 -2C / + 2C		1.71	2.16	1.14
Average E Pop #2 -2C / + 2C		1.36	1.37	1.08

**Table 4.12:** Report of Height peak and average Young's modulus (E) for the two populations of TYKNU CpR, OVCAR4 and HEY before and after 2C treatment. In table are reported also the ratio between the peak height of two populations with and without 2C and the ratio between the average Young's Modulus of two populations before and after 2C treatment. Pop #1: lowest-stiffness population, Pop#2: highest-stiffness population.

#### 4.4.4 Time-depending Effects on Young's Modulus of 2C Treatment

In order to observe the time-related effect of 2C on mechanical properties, around 30 cells for each cell line were analyzed by AFM in a medium supplemented with 20  $\mu\text{M}$  of 2C. The measurement was carried out between 7 and 9 hours from drug administration and the single cell Young's Moduli were analyzed in function of the time (**Figure 4.16**). The Mann-Kendall test did not highlight any positive or negative trend in any cell line after 2C treatment (**Table 4.13**).

Cell Line	IC50 ( $\mu\text{M}$ )	Mann-Kendall test (p-value)
IGROV1	1.01	0.234
OAW42	5.94	0.102
TYKNU	7.86	0.977
CAOV3	8.9	0.524
OVCAR8	12.69	0.747
TYKNU CpR	30.58	0.843
SKOV3	31.11	0.243
OVCAR4	37.7	0.186
HEY	55	0.417

**Table 4.13:** Results of Mann-Kendall test for the time series of single cell Young's Modulus after 2C treatment.

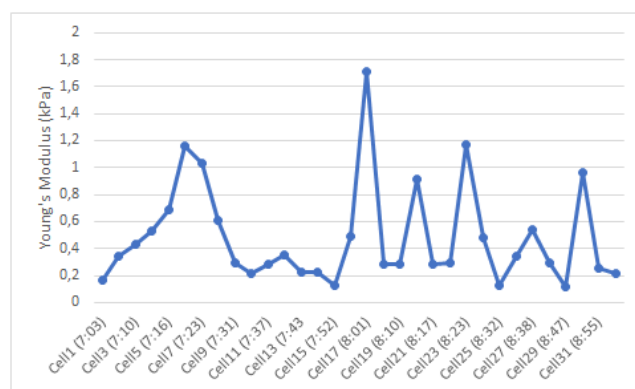


**Figure 4.16:** Example of a time course of single cell Young's modulus for TYKNU cell line treated with 2C. In X axis are reported the time points (in hours) from 2C administration when the cell was submitted to AFM measure.

To have a wider view of the time-depending effects of 2C on mechanical properties, the single cell Young's moduli were divided in four half-hour group and compared. The first half-hour group showed that the 2C-induced decrease of Young's modulus had already occurred after 7 hours from treatment for each cell line (**Table 4.14**). Nonetheless, the Kruskal-Wallis test applied to the half-hour groups did not return any significant difference among them (**Table 4.14**). These results can be due to an analysis time range (two hours) not so wide to appreciate significant time-depending changes induced by 2C in Young's Modulus. Another explanation can be the choice of the start time point at 7 hours, that could be too late for a real-time analysis. The ubiquitin-proteasome system inhibitors like the 2C have indeed a remarkable fast activity (e.g: the proteasome inhibition activity of bortezomib, the most used drug in this class, is already recognizable after 2 hours from drug administration, [140] [141]).

Cell Line	IC50 ( $\mu\text{M}$ )	Average E Half-Hour Group (kPa)				Kruskal-Wallis test (p-value)
		7:00-7:30	7:30-8:00	8:00-8:30	8:30-9:00	
<b>IGROV1</b>	1.01	0.46 $\pm$ 0.16	0.43 $\pm$ 0.20	0.44 $\pm$ 0.22	0.26 $\pm$ 0.07	0.150
<b>OAW42</b>	5.94	0.17 $\pm$ 0.04	0.14 $\pm$ 0.04	0.19 $\pm$ 0.11	0.19 $\pm$ 0.03	0.07
<b>TYKNU</b>	7.86	0.12 $\pm$ 0.03	0.12 $\pm$ 0.04	0.14 $\pm$ 0.05	0.12 $\pm$ 0.02	0.831
<b>CAOV3</b>	8.9	0.8 $\pm$ 0.44	0.79 $\pm$ 0.5	0.77 $\pm$ 0.49	0.82 $\pm$ 0.37	0.385
<b>OVCAR8</b>	12.69	0.43 $\pm$ 0.16	0.52 $\pm$ 0.14	0.52 $\pm$ 0.18	0.44 $\pm$ 0.18	0.249
<b>TYKNU CpR</b>	30.58	0.26 $\pm$ 0.13	0.29 $\pm$ 0.13	0.28 $\pm$ 0.15	0.22 $\pm$ 0.09	0.731
<b>SKOV3</b>	31.11	0.45 $\pm$ 0.17	0.29 $\pm$ 0.10	0.44 $\pm$ 0.18	0.46 $\pm$ 0.15	0.08
<b>OVCAR4</b>	37.7	0.70 $\pm$ 0.35	0.54 $\pm$ 0.40	0.68 $\pm$ 0.31	0.64 $\pm$ 0.32	0.498
<b>HEY</b>	55	0.62 $\pm$ 0.31	0.27 $\pm$ 0.10	0.68 $\pm$ 0.50	0.36 $\pm$ 0.26	0.06

**Table 4.14:** Average Young's modulus and standard deviation of each half-hour group for cell lines treated with 2C. In table are reported the results of Kruskal-Wallis test for the four half-hour groups. No: Accept H0 hypothesis (not significant difference), Yes: Accept H1 hypothesis (significant difference), E: Young's Modulus.

## 4.5 Fluorescence Assay

### 4.5.1 Uptake Assay

The 2C cellular uptake and its kinetics was assessed in HEY and OVCAR4 cell lines treated with 2  $\mu$ M of 2C conjugated with the fluorophore F2 ( $\lambda$  emission: 524 nm). Treatment lasted 24 hours and images were taken at 6 and 24 hours in order to observe 2C internalization and distribution inside cells. Images were analyzed by ImageJ to detect the average fluorescence intensity inside cells and in background. Images showed a consistent internalization of 2C-F2 inside the cells at 6 hours from drug administration. Fluorescence intensity inside cells for both cell lines resulted on average at least 2-fold higher than the one measured in background (2.76 for OVCAR4 and 3.63 for HEY) after 6 hours from the treatment.

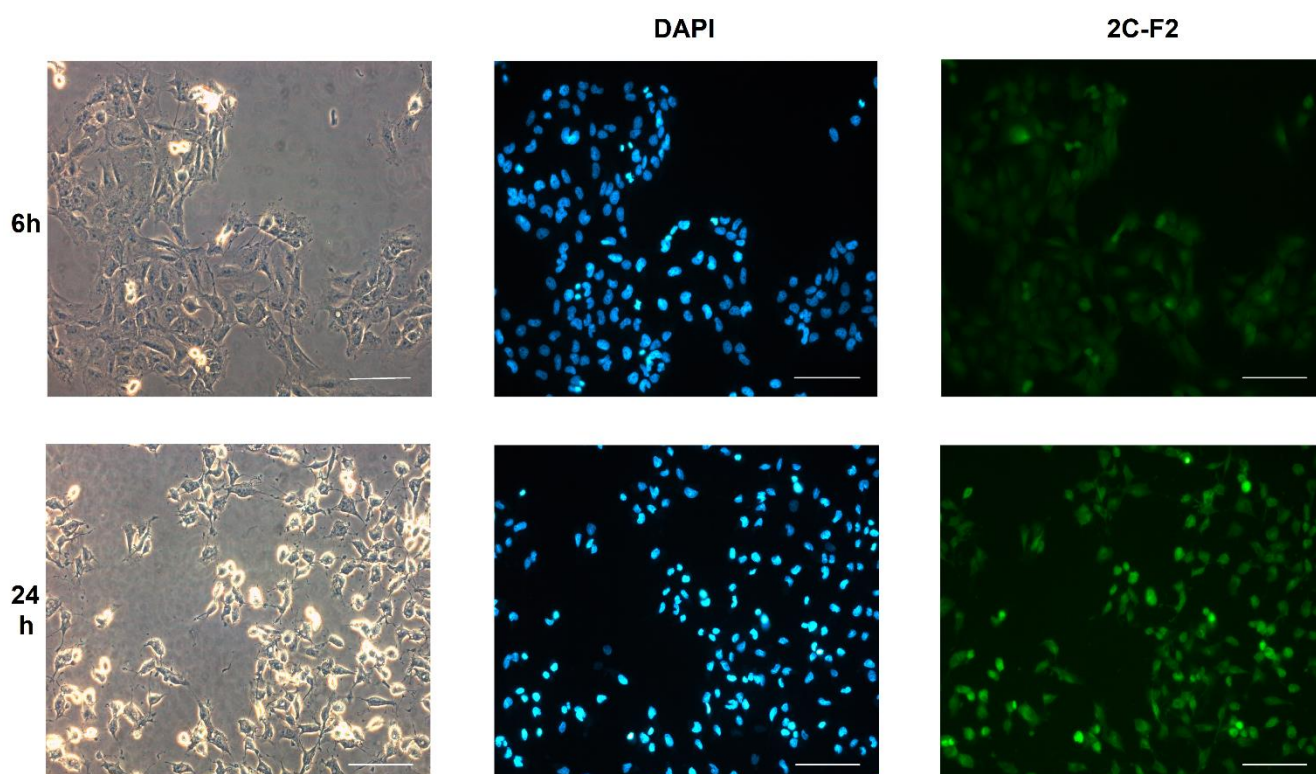


**Figure 4.17:** Fluorescent images of OVCAR4 after 2C-F2 treatment at 6 and 24 hours from treatment (3<sup>rd</sup> column). In figure are reported the raw images (1<sup>st</sup> column) and the DAPI-marked nuclei images (2<sup>nd</sup> column). All images were taken at a magnification of 20X. The scale bar corresponds to 100  $\mu$ m.

Cell line	IC50 ( $\mu\text{M}$ )	Average Fluorescence intensity inside cells / Background	
		6 hours	24 hours
OVCAR4	37.7	$2.90 \pm 0.97$	$3.75 \pm 0.97$
HEY	55	$3.63 \pm 0.81$	$7.41 \pm 2.05$

**Table 4.15:** Ratio between the average fluorescence intensity inside cells and background at 6 and 24 hours.

In HEY cells, which had the highest IC50, there was a linear relationship between the fluorescence intensity related to 2C-F2 and the time, indicating a possible accumulation in the cell. For OVCAR4, the intensity increment was faster in the first 6 hours and then slowed down. However, the detection of two time points only did not allow drawing any conclusions about the kinetics of uptake.

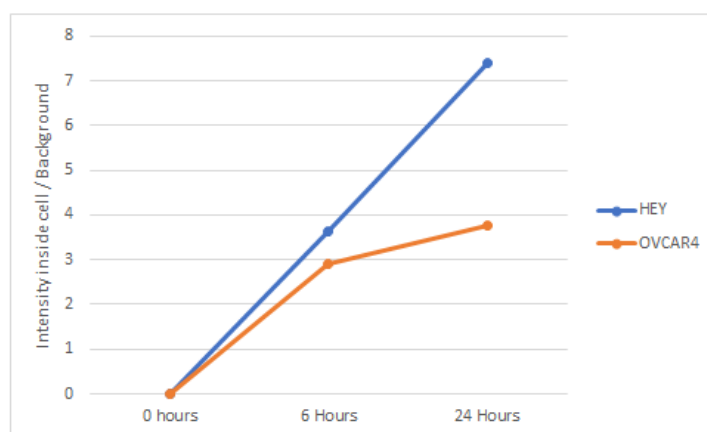


**Figure 4.18:** Ratio between the average fluorescence intensity inside cells and background in function of time. For time 0, it was supposed that the ratio value was 0 as 2C was not present inside cells at that time.

#### 4.5.2 F-actin Staining

As 2C has a side effect on Actin network organization by activation of Cofilin-1, a fluorescence assay based on F-actin staining by phalloidin was carried out on TYKNU, OVCAR4 and HEY cell lines. Cells were treated with 2  $\mu\text{M}$  of 2C and VV1 (the inactive isoform of the drug used as negative control) for 24 hours and then

stained with the phalloidin conjugated with the fluorophore TRITC. Finally, the area and the average fluorescence intensity of about 80 single cells for each cell line were recorded from fluorescent images by ImageJ. The aim of this assay was at observing the Actin network organization before and after the 2C treatment.

Actin stress fibers were detectable in each cell line treated with VV1, while in cells treated with 2C there were high-intensity spots suggesting for F-actin monomer clusters presumably caused by 2C-induced disruption of F-actin filaments. Moreover, there were also several high-intensity rings in the cell periphery or around the nuclei (**Figure 4.19**). This effect is in line with the mechanism of action of 2C, which leads to the depolymerization of the Actin network. In HEY cells treated with VV1 the Actin stress fibers were faint with occasional high-intensity spots, which increased in

number after 2C treatment (**Figure 4.19**). This can support for a different cytoskeleton organization of HEY cell line.

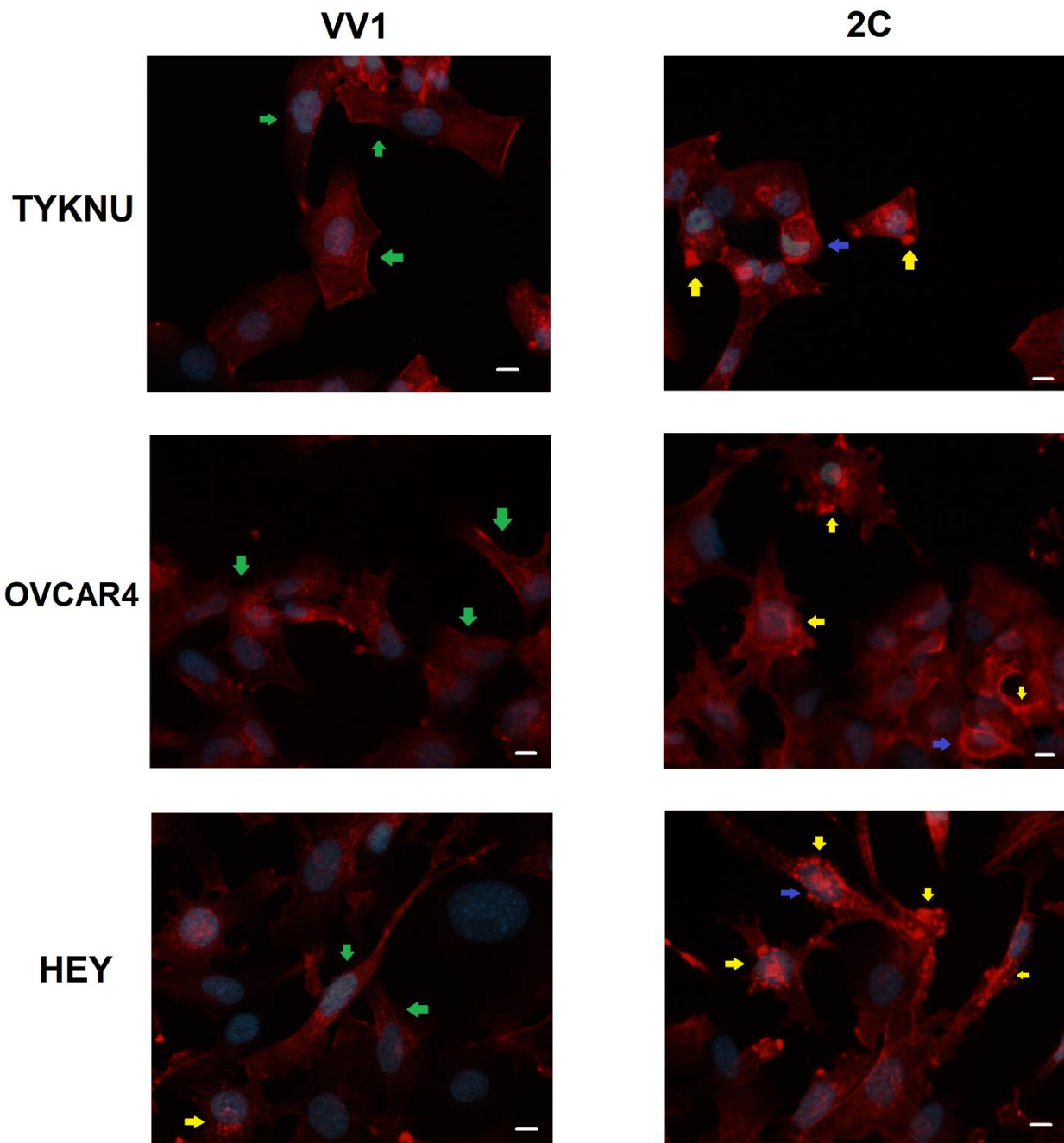


**Figure 4.19:** Images of F-actin staining by phalloidin for TYKNU, OVCAR4 and HEY cell lines treated with VV1 (negative control) and 2C. In blue the DAPI-marked nuclei. Green arrow: stress Actin fibers, Yellow arrow: high-intensity spots, Blue arrow: high-intensity rings. Scale bar: 10  $\mu$ m.

The analysis of the single cell area showed for each cell line a significant decrement after 2C treatment, as confirmed by Mann-Whitney test (TYKNU p: 0.04, OVCAR4 p: 0.02, HEY p: 0.01). Likewise, the average fluorescence increased significantly in each cell line after 2C administration, as confirmed by Mann-Whitney test (TYKNU p: 0.01,

OVCAR4 p: <0.00001, HEY: 0.008). The area decrement was similar for each cell line as well as the average fluorescence increment (**Table 4.16**). To search for a possible correlation between these variables, the Spearman's correlation test was run. This test returned a significant correlation between area decrement and fluorescence increment in every cell line after treatment with 2C, but not VV1 (**Table 4.17**), suggesting on a possible dependence between the two variables.

Cell line	Treatment	Area ( $\mu\text{m}^2$ )	A.F.I. (p.i.)	Area VV1 / 2C	A.F.I. 2C / VV1
TYKNU	VV1	753.05 $\pm$ 384.59	18.65 $\pm$ 5.49	1.22	1.42
	2C	619.26 $\pm$ 250.72	26.43 $\pm$ 11.77		
OVCAR4	VV1	855.14 $\pm$ 246.73	17.63 $\pm$ 9.29	1.21	1.61
	2C	706.64 $\pm$ 264.41	28.47 $\pm$ 11.32		
HEY	VV1	889.73 $\pm$ 337.19	15.79 $\pm$ 7.78	1.27	1.61
	2C	700.06 $\pm$ 251.69	25.48 $\pm$ 9.28		

**Table 4.16:** Average area and fluorescence intensity of single cells for TYKNU, OVCAR4 and HEY cell lines. In table are reported the ratio between the area of cells treated with VV1 and 2C and the ratio between the average fluorescence intensity of cells treated with 2C and VV1. A.F.I. : Average Fluorescence Intensity, p.i. : pixel intensity.

Cell line (treatment)	Spearman (area-A.F.I)		
	rs	p-value	95% CI
TYKNU (VV1)	-0.06	0.37	-0.42;0.31
OVCAR4 (VV1)	-0.21	0.13	-0.53;0.17
HEY (VV1)	0.22	0.11	-0.15;0.54
TYKNU (2C)	-0.54	0.001	-0.77;-0.19
OVCAR4 (2C)	-0.40	0.01	-0.67;-0.03
HEY (2C)	-0.43	0.01	-0.69;-0.06

**Table 4.17:** Results of Spearman correlation test for area and average fluorescence intensity of TYKNU, OVCAR4 and HEY cell lines treated with VV1 and 2C. In table are reported the p value and the 95% CI with the lower and upper confidence limits. rs: Spearman correlation coefficient, A.F.I. : Average Fluorescence Intensity.

To investigate on possible associations between the Young's moduli distribution and the fluorescence assay data, the Anderson-Darling test was run using the area and average fluorescence intensity of cell lines treated with VV1. The distribution analysis of the single cell area showed a Gaussian distribution for OVCAR4 cells and a non-normal distribution for HEY and TYKNU ones (**Table 4.18**). This can be related to the shape of TYKNU and HEY cells which had a fibroblastic morphology. Interestingly,

the distribution pattern of the average fluorescence intensity of the three cell lines treated with VV1 was equal to their stiffness distribution (non-normal for OVCAR4 and HEY and Gaussian for TYKNU) (**Table 4.18**).

Cell line (VV1)	Morphology	Anderson-Darling (p-value)	Distribution pattern
<b>TYKNU (Area)</b>	Fibroblastic	0.03	Not-Gaussian
<b>TYKNU (A.F.I.)</b>	Fibroblastic	0.133	Gaussian
<b>OVCAR4 (Area)</b>	Epithelial	0.351	Gaussian
<b>OVCAR4 (A.F.I.)</b>	Epithelial	0.001	Non-Gaussian
<b>HEY (Area)</b>	Fibroblastic	0.011	Non-Gaussian
<b>HEY (A.F.I.)</b>	Fibroblastic	0.0001	Non-Gaussian

**Table 4.18:** Results of Anderson-Darling test on area and average fluorescence intensity data of single cells for each cell line treated with VV1. A.F.I. : Average Fluorescence Intensity.

### 4.5.3 $\beta$ -Tubulin Staining

To deeply investigate on 2C effects on cytoskeletal organization, an immunofluorescence staining of  $\beta$ -tubulin (an important component of microtubules) was carried out in TYKNU, OVCAR4 and HEY cell lines. Cellular cytoskeleton is a complex and heterogeneous network of different and closely interconnected components (such as actin filaments, microtubules and intermediate filaments), where variation in one of its components can impact on the other ones. Accordingly, 2C effects on Actin network can influence all the components of cellular cytoskeleton. Therefore, an analysis of microtubules organization after 2C treatment can be useful. TYKNU, OVCAR4 and HEY cell lines were treated with 2  $\mu$ M of VV1 and 2C for 24 hours and then the  $\beta$ -tubulin was stained. The area and the average fluorescence intensity of about 80 cells for each cell line were recorded from fluorescent images by ImageJ.

Cell lines treated with VV1 showed a “bush” organization characterized by microtubules filaments departing from the cell center to its periphery. This organization was barely detectable in VV1 treated HEY cells. The 2C treatment led to the disruption of the microtubules network which spread in disorganized filaments

over the cell. In HEY cells, occasional high-intensity points over the nucleus were observed. This further proves the side effects of 2C on cytoskeleton network integrity (Figure 4.20).

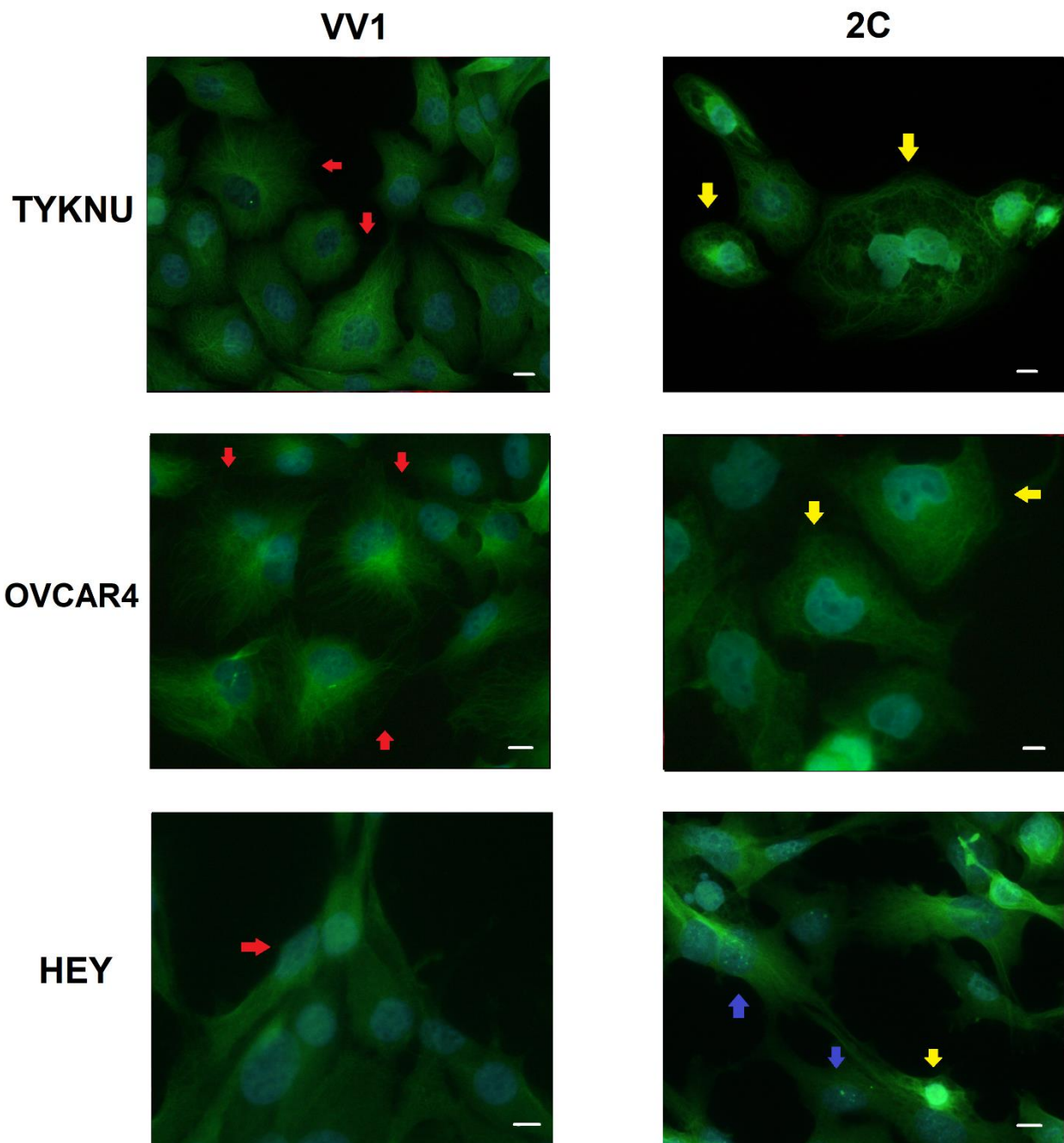


**Figure 4.20:** Images of  $\beta$ -tubulin immunofluorescence staining for TYKNU, OVCAR4 and HEY cell lines treated with VV1 (negative control) and 2C. In blue the DAPI-marked nuclei. Red arrow: “bush” microtubules network, Yellow arrow: disrupted microtubules, Blue arrow: nuclear high-intensity points. Scale bar: 10  $\mu$ m.

Similar to the previous fluorescence assay, a significant decrement of cell area (Mann-Whitney test TYKNU p: 0.037, OVCAR4 p: 0.049, HEY p: 0.043) and an increment of average fluorescence intensity (Mann-Whitney test TYKNU p: 0.0002,

OVCAR4  $p < 0.00001$ , HEY  $p: 0.0002$ ) after 2C treatment were observed. The extent of both variations was similar for each cell line (**Table 4.19**). There was a significant correlation between the area and the average fluorescence intensity for both treatments (VV1 and 2C), as established by Spearman's test (**Table 4.20**), suggesting a possible correlation between the cell size and the microtubules organization independently from the drug treatment.

Cell line	Treatment	Area ( $\mu\text{m}^2$ )	A.F.I. (p.i.)	Area VV1 / 2C	A.F.I. 2C / VV1
TYKNU	VV1	763.44 $\pm$ 280.18	22.22 $\pm$ 2.86	1.26	1.60
	2C	607.33 $\pm$ 224.02	35.67 $\pm$ 13.54		
OVCAR4	VV1	845.30 $\pm$ 285.25	24.24 $\pm$ 5.19	1.19	1.59
	2C	708.77 $\pm$ 242.72	38.45 $\pm$ 10.45		
HEY	VV1	852.61 $\pm$ 333.47	10.38 $\pm$ 2.78	1.25	1.65
	2C	683.33 $\pm$ 247.98	17.17 $\pm$ 4.25		

**Table 4.19:** Average area and fluorescence intensity of single cells for TYKNU, OVCAR4 and HEY cell lines. In table are reported the ratio between the area of cells treated with VV1 and 2C and the ratio between the average fluorescence intensity of cells treated with 2C and VV1. A.F.I. : Average Fluorescence Intensity, p.i. : pixel intensity.

Cell line (treatment)	Spearman (area-A.F.I)		
	rs	p-value	95% CI
TYKNU (VV1)	-0.58	0.0008	-0.79;-0.23
OVCAR4 (VV1)	-0.35	0.0009	-0.66;-0.06
HEY (VV1)	-0.57	0.004	-0.79;-0.23
TYKNU (2C)	-0.57	0.003	-0.79;-0.22
OVCAR4 (2C)	-0.49	0.0005	-0.73; -0.13
HEY (2C)	-0.37	0.02	-0.65;-0.36

**Table 4.20:** Results of Spearman correlation tests for area and average fluorescence intensity of TYKNU, OVCAR4 and HEY cell lines treated with VV1 and 2C. In table are reported the p-value and the 95% CI with the lower and upper confidence limits. rs: Spearman correlation coefficient, A.F.I. : Average Fluorescence Intensity.

The distribution test of the area and the average fluorescence intensity of single cells showed the same results achieved in the F-actin fluorescence assay for each cell line treated with VV1 (**Table 4.21**).

Cell line (VV1)	Morphology	Anderson-Darling (p-value)	Distribution pattern
TYKNU (Area)	Fibroblastic	0.034	Non-Gaussian
TYKNU (A.F.I.)	Fibroblastic	0.077	Gaussian
OVCAR4 (Area)	Epithelial	0.504	Gaussian
OVCAR4 (A.F.I.)	Epithelial	0.0001	Non-Gaussian
HEY (Area)	Fibroblastic	0.004	Non-Gaussian
HEY (A.F.I.)	Fibroblastic	0.0001	Non-Gaussian

**Table 4.21:** Results of Anderson-Darling test on area and average fluorescence intensity data of single cells for each cell line treated with VV1. A.F.I. : Average Fluorescence Intensity.

#### 4.5.4 Analysis of Cytoskeleton Distribution

Since the variations of structure and organization of cytoskeleton are involved in many tumoral processes, such as metastasis and drug responsiveness, an analysis of the F-actin and microtubules network distribution inside cells was performed on fluorescent images achieved by the previously described assays. The analysis was carried out using an ImageJ tool that provides a view of cytoskeleton filaments organization within the cells. This tool was able to measure the staining intensity along an automatically draw line over the cell. In this way, it was possible to obtain a fluorescence intensity profile which provides hints on cytoskeleton distribution inside cells. Moreover, the division of the intensity data in 10 equal bins makes this analysis insensible to changes in cell size and shape.

As concern the F-actin staining assay, in cell lines treated with VV1 was possible to observe how the fluorescence intensity tended to be higher in cell center of TYKNU cells and more distributed for the OVCAR4 and HEY ones. This could suggest a possible correlation between the intensity distribution and the IC50 for 2C and the average Young's modulus. After the 2C treatment, the F-actin intensity was

tendentially higher at the cell border than in the cell center for each cell line. In HEY cells there was a further intensity peak in innermost bins (**Figure 4.21**).

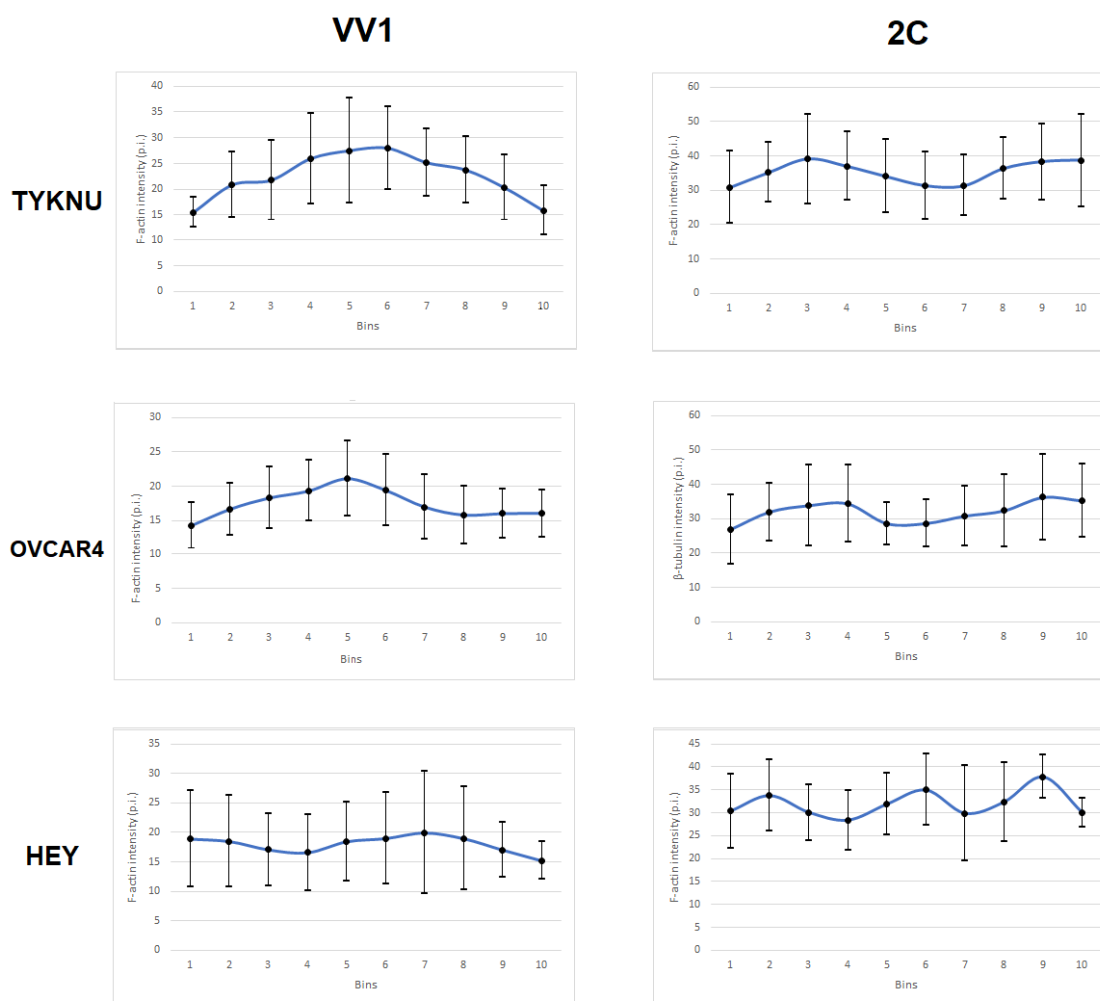


**Figure 4.21:** F-actin fluorescence intensity profile of each cell lines treated with VV1 and 2C. For each bins is reported the average F-actin fluorescence intensity plus the 95% confidence interval (CI). The 3 most external bins (1-3 and 8-10) indicate the cell periphery. p.i.: pixel intensity.

These considerations can be seen also in  $\beta$ -tubulin-stained cell lines treated with VV1. On the contrary, TYKNU cells showed a peak of  $\beta$ -tubulin intensity in cell center after the 2C treatment, while as concern the OVCAR4 and HEY cells, the intensity was higher at the cell border than the center, similarly to the corresponding F-actin intensity profile after drug administration (**Figure 4.22**).

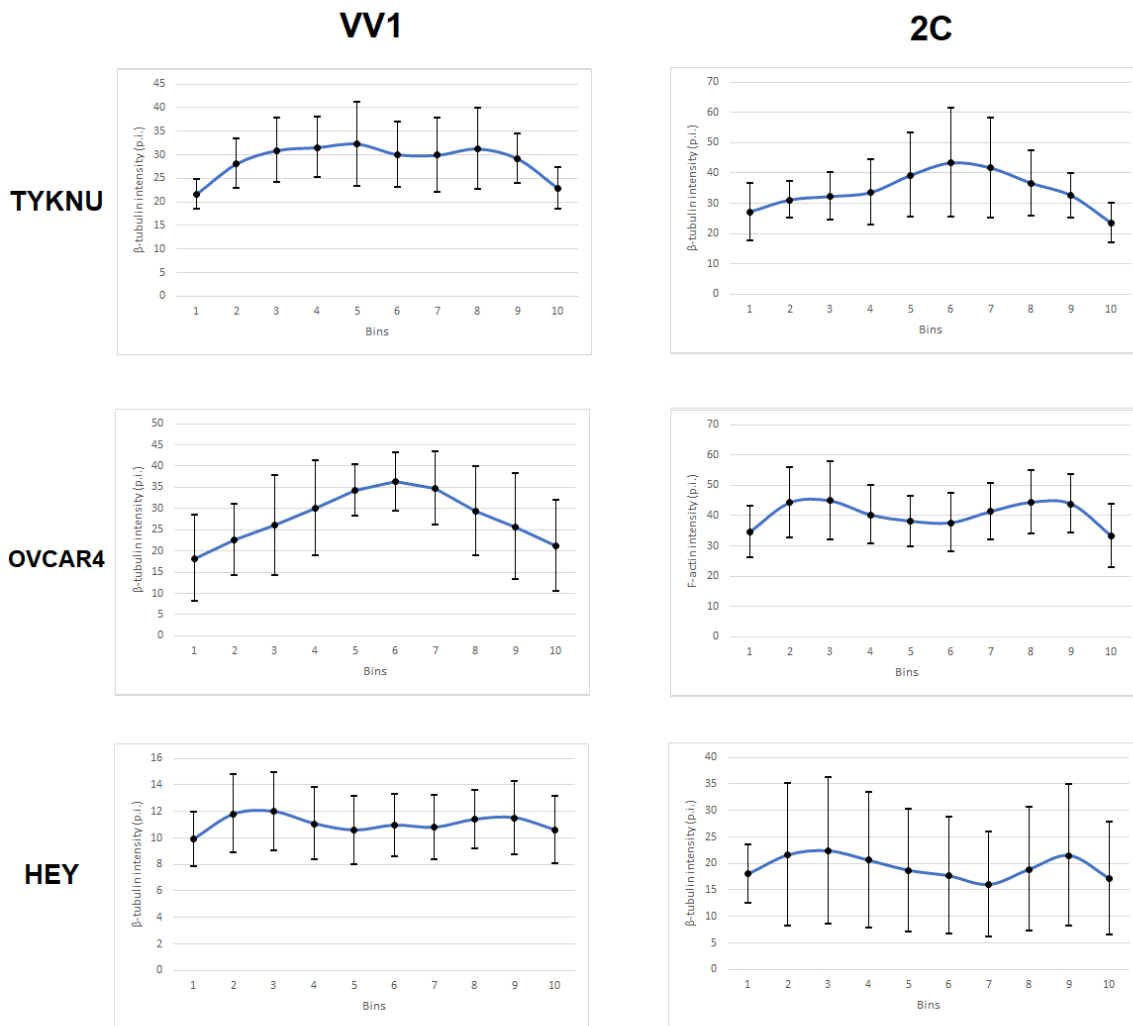


**Figure 4.22:**  $\beta$ -tubulin fluorescence intensity profile of each cell lines treated with VV1 and 2C. For each bins is reported the average F-actin fluorescence intensity plus the 95% confidence interval (CI). The 3 most external bins (1-3 and 8-10) indicate the cell periphery. p.i.: pixel intensity.

## 5. Discussion

The epithelial ovarian cancer (EOC) is the most common and deadly form of ovarian cancer [5]. It encompasses a collection of neoplasms with distinct clinical-pathological, molecular features and prognosis; among them the most common are the clear cells (CCOC), the mucinous (MOC), the endometrioid (ENOC), the low grade serous (LGSOC) and the high grade serous ovarian cancer (HGSOC) [8] [5]. A correct diagnosis of these subtypes is prominent in EOC management, because each one needs an appropriate and specific treatment [49]. This is a key point especially for the HGSOC, the deadliest form of gynecological malignancy, with 295'000 new cases diagnosed annually worldwide and 185'000 related deaths [2]. The high intratumor heterogeneity and late stage at diagnosis of HGSOC, indeed, lead to a high mortality: the 5-years survival rate is around 46% and has not significantly changed over the past 20 years. Considering this, the tumoral mechanical properties can be useful to further characterize those tumors, obtaining possible predictive and/or prognostic information to be used in addition to classic biomarkers used in clinical routine. The role played by the mechanical forces in different tumoral processes, such as the metastatic invasion and the responsiveness to the chemotherapy drugs have been already proven [66] [81] [82].

The main goal of this thesis was the mechanical characterization by Atomic Force Microscope (AFM) of nine ovarian cancer cell lines with distinct histological and morphological characterization in order to test the possible utility of the mechanical properties as characterization biomarker. Further, an invasive assay was carried out on the cell lines to investigate on possible associations between the mechanical properties and the metastatic potential. On the possible utility of biomechanical properties, each cell line was treated with 2C, a drug for possible tumor treatment, which involves the cytoskeleton reorganization, and then it was analyzed by AFM to investigate the possible use of mechanical properties as markers of drug sensitivity. Finally, an evaluation of the possible effects of the culture medium composition on mechanical properties was performed in parallel measurements.

## 5.1 Histological, Morphological and Mechanical Characterization

The molecular analysis of the cell lines used in this thesis showed at least one representative for each EOC subtype, namely CCOC (OAW42), ENOC (IGROV1, SKOV3), MOC (TYKNU, TYKNU CpR), LGSOC (HEY) and HGSOC (OVCAR8, OVCAR4, CAOV3). Morphologically, the cell lines were divided in two different groups: cell lines with fibroblastic morphology (TYKNU, TYKNU CpR, SKOV3, HEY) and with epithelial morphology (OAW42, IGROV1, OVCAR8, OVCAR4 and CAOV3). This analysis showed that all the HGSOC cell lines had an epithelial morphology, that could be due to their epithelial origin site (ovarian surface epithelium, OSE or fallopian tube serous epithelium, FTSE) [45] [46].

The mechanical characterization displayed a wide variation of Young's Moduli (E) (from  $0.28 \pm 0.12$  kPa for TYKNU to  $1.84 \pm 0.67$  kPa for CAOV3), which indicated a remarkable difference in cellular stiffness among the cell lines. Moreover, the distribution analysis of single cell Young's moduli showed two different patterns: unimodal or Gaussian (TYKNU, OAW42, IGROV1, CAOV3) and bimodal pattern (TYKNU CpR, OVCAR8, SKOV3, HEY, OVCAR4). The latter distribution pattern indicated the presence of two different cell populations characterized by distinct stiffness. In particular, we observed that the higher stiffness population was characterized by a higher variability than the softer one (except for TYKNU CpR). The presence of two distinct cell stiffness phenotypes was probably related to different molecular mechanisms which could underline other cell features [142]. The comparison of the mechanical properties of TYKNU and the corresponding cisplatin resistant subline TYKNU CpR showed two differences: a higher stiffness and bimodal distribution for the TYKNU CpR and a lower stiffness and Gaussian distribution for TYKNU. These evidences were suggestive that an increase in the average Young's modulus and its bimodal distribution could be related to cis-platinum resistance [143]. In particular, the passage from a Gaussian distribution to a bimodal one characterized by two different populations could be a consequence of a clonal selection due to the treatment of cis-platinum sensitive cell line (TYKNU) with stepwise concentration of cis-platinum to obtain the resistant one (TYKNU CpR). The similar average Young's moduli of TYKNU and TYKNU CpR lowest-stiffness population ( $0.28 \pm 0.12$  kPa and  $0.24 \pm 0.12$  kPa respectively) can further support this hypothesis.

The analysis of average Young's Modulus in function of the histological classification showed a high variability for HGSOC cell lines, which could reflect the heterogeneity that characterized this tumor [144]. This heterogeneity was observable also in the Young's moduli distribution patterns related to HGSOC cell lines: the OVCAR4 and OVCAR8 had a bimodal distribution while CAOV3 showed a Gaussian one. Nevertheless, heterogenous patterns were observed also in ENOC cell lines (bimodal for SKOV3 and unimodal for IGROV1) supporting a weak correlation between this parameter and the histological classification. These patterns could be due to other factors, such as the drug resistance/treatment of the original tumor from which the cell lines were isolated. The OVCAR4 and OVCAR8 were indeed derived from a tumor refractory at Adriamycin/cis-platinum [112] and a tumor treated with carbonplatin [113] respectively, while for CAOV3 was not reported drug resistance/treatment of the original tumor. Similar observations were also found in ENOC cell lines (original tumor of SKOV3 was resistant to cis-platinum/Adriamycin, [114], while IGROV1 derived from a tumor sensible to cis-platinum, [110])

Overall, from our data series, mechanical data (Young's moduli) were able to discriminate among the different ovarian cancer histological subtypes, except for MOC vs CCOC and LGSOC vs HGSOC. However, as a possible limitation, in this study only one cell line as representative of CCOC, MOC and LGSOC subtypes was analyzed. Serous cell lines, including both LGSOC and HGSOC, resulted to be stiffer than the other ones, maybe because of their cytoskeleton organization [145] [146].

To conclude, three out of the four cell lines with fibroblastic morphology had a bimodal distribution (TYKNU CpR, SKOV3 and HEY), supporting in these cell lines the presence of different stiffness populations. Moreover, cells with epithelial morphology resulted stiffer than the ones with fibroblastic morphology. This is in agreement with a possible epithelial mesenchymal transition (EMT) in cell line with fibroblastic morphology. EMT has been already associated to higher cell deformability, therefore metastatic potential [147] [148]. This difference could be due to the different cytoskeleton organizations which characterized this two cell morphology *in vivo* and *in vitro* [149] [150] [151].

## 5.2 Invasion Assay

The results of invasion assay showed different metastatic potentials among the cell lines analyzed in this thesis. Several studies have indicated that a low stiffness was

associated with an increase in invasion capacity [82] [152] [153]. Notwithstanding, the analysis of invasion data of cell lines in function of their average Young's modulus did not show a significant correlation. On the contrary, considering only the low-stiffness population for cell lines with bimodal pattern, the correlation between stiffness and invasion capacity was strong. This indicated that in a stiffness-heterogeneous cell line only the softer population had eventually the metastatic potential to invade. Anyway, it is important to consider that OVCAR4 and OVCAR8 cell lines, which had a bimodal distribution of the Young's moduli, had a relatively low invasion capacity, suggesting that the metastatic potential was not only associated to the stiffness distribution pattern, but also to the absolute value of the Young's modulus. The average stiffness of the softer population of OVCAR8 and OVCAR4 (low invasivity) was higher than the one from the other cell lines with bimodal distribution pattern (high invasivity).

The HGSOC cell lines had a low metastatic potential, as reported previously in literature [154]. This finding would be unexpected considering the high clinical aggressiveness of HGSOC, but those tumors are progressing invading the peritoneal cavity without the need to seed in other organs. Even very large tumor masses invade the superficial layers of the bowel and omentum, but not deeper layers. It is rare to find HGSOC metastases to the bone or brain, contrarily to other carcinomas, such as breast and colon cancers [155].

The invasion data showed a strong association between the cell morphology and metastatic potential. Cell lines with fibroblastic morphology were remarkably more invasive than the one with epithelial morphology. The ability of cancer to invade depends indeed on the degree of epithelial differentiation within the tumor: poorly differentiated tumors are more invasive than well-differentiated ones. From this reason, cancer cells need undergoing an epithelial-mesenchymal transition (EMT) to lose adhesion and epithelial morphology and to assume, in this way, mobility with a mesenchymal-fibroblast morphology [156]. Taken this evidence, our results on invasion assay in function of morphological classification are in agreement with the fundamental processes underlining the metastatic diffusion.

## 5.3 2C Treatment

### 5.3.1 Mechanical Properties and 2C Sensitivity

The analysis of IC<sub>50</sub> for the 2C showed different degrees of sensitivity to this drug among the cell lines (it ranged from 1.01  $\mu$ M for IGROV1 to 55  $\mu$ M for HEY). This parameter indicated a higher 2C resistance for TYKNU CpR than TYKNU (the IC<sub>50</sub> was respectively 30.58  $\mu$ M and 7.86  $\mu$ M), similarly to cis-platinum [157]. Accordingly, it was possible to speculate about a possible relationship between the stiffness increase and the bimodal distribution of Young's modulus in 2C resistant cells. Although the correlation between the mean Young's moduli and IC<sub>50</sub> was weak, considering only the stiffer populations in cell lines with bimodal pattern, the correlation was significant, as shown by the Spearman's test ( $r_s$ : 0.57,  $p$ : 0.04; 95%CI [-0.22;0.91]). In agreement with this finding also the Young's moduli distribution patterns and the IC<sub>50</sub> resulted associated: cell lines with bimodal pattern were more resistant to 2C than the ones with unimodal pattern.

The treatment with 2C led to a significant decrease of the average Young's modulus in each cell line. This is in agreement with the depolymerization by 2C of the F-actin filaments, as already reported [106] [158]. The degree of stiffness decrease depended on both the IC<sub>50</sub> and the distribution pattern: cell lines with high IC<sub>50</sub> (> 10  $\mu$ M) and bimodality had a tendentially lower stiffness decrease than the ones with low IC<sub>50</sub> (< 10  $\mu$ M) and unimodality, as shown by the fluorescent staining of F-Actin. Over the average stiffness, the 2C treatment had effects also on the single cell Young's moduli distribution patterns. The distribution pattern of untreated cell lines was usually maintained after 2C treatment, except for SKOV3 and OVCAR8 cell lines which lost their bimodality, assuming a Gaussian distribution. In comparison to the other cell lines with bimodal distribution, the SKOV3 and OVCAR8 had a higher ratio between the lowest-stiffness peaks height and highest-stiffness population, indicating that a possible prevalence of the softest population against the stiffer one, which had also a wider distribution of the Young's moduli indicating more likely a broader stiffness heterogeneity. It is possible that 2C treatment killed preferentially one cell population. As concern the TYKNU CpR, OVCAR4 and HEY, although the two subpopulations were observable after the 2C treatment, the stiffer ones resulted remarkably underrepresented. Nevertheless, the stiffer populations decreased their stiffness on average less than the "softer" cells, except for HEY. This suggested that

the highest-stiffness population had a higher 2C resistance than the lowest-stiffness one. From this point of view, the small stiffness decreases of both sub-populations observed in HEY after the 2C treatment can explain its highest IC50 (55  $\mu$ M) among the analyzed cell lines.

In the end, the analysis of the mechanical properties in function of 2C responsiveness has confirmed the role played by the stiffness increase and the stiffness population heterogeneity in drug resistance, in agreement with published observations for other chemotherapy drugs [143] [157] [159].

These results did not show a significant association between 2C sensitivity and the morphological or histological classification of the analyzed cell lines.

### **5.3.2 Kinetics of 2C Uptake and Action**

The results of the 2C uptake assay performed on HEY and OVCAR4 showed for both cell lines a consistent drug internalization after 6 hours from the drug administration, in agreement with the kinetics uptake data reported in literature for this drug as well as other 2C-like proteasome system inhibitors [133] [158].

The time-course AFM analysis indicated that the 2C-induced stiffness decrease was observable already after 7 hours from the drug treatment, independently from the IC50 or the average Young's modulus of untreated cell lines. This was likely due to the remarkable fast activity characterizing the proteasome system inhibitors [140] [141]. This result was also confirmed by the kinetics uptake data previously discussed.

The analysis of single cell Young's moduli in function of the time (achieved between 7 and 9 hours from 2C treatment) did not show any recognizable trend. This could be due to an analysis time range not sufficiently long to appreciate the time-dependent effects of 2C on mechanical properties. Another explanation can be the chosen time starting point (7 hour), that could be too late for a time-dependent analysis.

### **5.3.3 2C Effects on Cytoskeleton**

The F-actin staining assay of TYKNU, OVCAR4 and HEY before and after 2C treatment showed the presence of the Actin stress fibers in each untreated cell line. The fibers organization reflected the morphological classification of the analyzed cell lines: parallel bundles for the TYKNU and HEY (fibroblastic morphology) and tangled

network for OVCAR4 (epithelial morphology) [150] [152]. The three cell lines treated with 2C showed a disruption of the Actin stress fibers, which accumulated in high-intensity spots and rings in the cell periphery, in agreement with the mechanism of action of 2C. After the treatment, each cell line showed an increase of fluorescence intensity correlated to the 2C-induced decrease of cell area [158]. The size of both variations was similar for each cell line. The analysis of F-actin intensity profile before the treatment with 2C showed that the fluorescence intensity tended to be more concentrated in cell center for TYKNU (low stiffness and IC50) and more distributed over the cell for OVCAR4 and HEY (high stiffness and IC50). This result indicated a possible association between the degree of Actin cytoskeleton distribution and the cell stiffness/2C sensitivity. However, although this analysis was independent from the cell size and shape, a possible contribution of cell stretching on achieved fluorescence intensity profile should be taken in consideration. Instead, in cell lines treated with 2C the F-actin fluorescence intensity tended to diffuse to the cell periphery from the cell center, as already seen for other drugs with cytoskeleton destabilizing activity [136]. This effect was particularly evident for TYKNU and OVCAR4, while in HEY the intensity profile resulted more heterogeneous. The single cell fluorescence intensity data and the single cell Young's moduli displayed a similar distribution pattern: unimodal for TYKNU and bimodal for HEY and OVCAR4. Despite this observation could lead to hypothesize on the presence of subpopulations with different Actin network organization and mechanical properties, it has not been possible to draw any conclusion about a possible association between these two parameters without an appropriate stiffness-based sorting of the cell lines and a fluorescence independent analysis of the resulting subpopulations.

As concern the  $\beta$ -tubulin staining assay, the fluorescent images for untreated cell lines showed a "bush" organization characterized by microtubule filaments departing from the cell center to the cell periphery. This organization was barely recognizable in HEY cells. After 2C treatment the microtubules filaments broke out and spread over the cells, with high-intensity cluster accumulation in cell center, similarly to what happens with other cytoskeleton destabilizing drugs [160]. This result proved that the 2C effects on Actin filaments involved indirectly also the other components of cellular cytoskeleton. Also in this case, the increase in  $\beta$ -tubulin fluorescence intensity after the 2C treatment was correlated to the 2C-induced cell contraction. The fluorescence intensity profiles of untreated cell lines showed a higher intensity in cell center than cell border for OVCAR4 and a more diffuse intensity over the cell in HEY and TYKNU. These distributions could be associated to the morphological classification of the cell

lines (epithelial for OVCAR4 and fibroblastic for HEY and TYKNU) rather than the cell stiffness or the IC50. The disruption or chemical stabilization of microtubules did not affect cell elasticity [164]. After 2C treatment, the fluorescence intensity profile of TYKNU showed a higher intensity in cell center with respect to the cell border, while as concern the OVCAR4 and HEY the intensity was concentrated in the cell periphery, as seen in F-actin staining assay.

## **5.4 Effects on Mechanical Properties of Culture Medium Composition**

IGROV1 cells cultured in the medium DMEM:F12 1:1 (the recommended medium) were significantly softer than the same cells cultured in the more generic medium RPMI 1640. This result was in accordance with previous reports [129].

The TYKNU cells cultured in EMEM supplemented with FBS 20% showed a higher mean Young's modulus than ones grown in the same medium with FBS 10%. It has already been proven that serum components such as lysophosphatidic acid (LPA) activate the small GTP-binding protein Rho, which subsequently promotes focal adhesions and actin stress fiber formation [161] [162], that impact the overall cellular elasticity [163] [164].

These results pointed out the importance to develop an optimized protocol for mechanical characterization of cell lines in order to level the effects of medium composition on mechanical properties.

## 6. Conclusions

In this thesis, mechanical properties were investigated to characterize epithelial ovarian cancer. The assessment was carried out using 9 ovarian cancer cell lines with different histological and morphological classification. According to our findings it is possible to conclude as follows:

- The average Young's modulus of HGSOC cell lines was highly heterogeneous. The serous cell lines (including both HGSOC and LGSOC) were stiffer than the other EOC subtypes.
- The analysis of single cell Young's moduli resulted to have a discrete capacity to discriminate about ovarian cancer cell lines with different histological classification.
- In cell lines with bimodal distribution of the stiffness the "stiffer" population was tendentially more variable and underrepresented than the "softer" one.
- The TYKNU cell line (sensible to cis-platinum) was significantly softer than the TYKNU CpR one (subline resistant to cis-platinum). Since they were characterized by two different Young's moduli distribution patterns (unimodal for TYKNU and bimodal for TYKNU CpR), the increase of the average stiffness in TYKNU CpR seemed to be the consequence of a clonal selection induced by the treatment of TYKNU with stepwise concentration of cis-platinum to obtain the resistant subline.
- The cells with epithelial morphology were stiffer than the ones with fibroblastic morphology. Moreover, the cell lines with fibroblastic morphology had usually a bimodal distribution of the stiffness.
- The decrease of stiffness was associated to an increase of invasion capacity. This association was significant only when considering the softer population for the cell lines with bimodal pattern. Accordingly, only the "softer" population in a stiffness-heterogeneous cell line had eventually the metastatic potential to invade.
- The cell lines with fibroblastic morphology were remarkably more invasive than the ones with epithelial morphology.
- There was a moderate positive correlation between the mechanical properties and 2C sensitivity among the analyzed cell lines. This correlation was

particularly evident considering the Young's moduli distribution patterns: cell lines with bimodal pattern have a higher IC50 for 2C than ones with unimodal pattern.

- The 2C treatment led to a decrease of the average Young's modulus, the size of which depended from the IC50 and the stiffness distribution pattern.
- The cell lines tendentially maintained their Young's Moduli distribution pattern after 2C treatment, except for the OVCAR8 and SKOV3. They lost their bimodality to assume a Gaussian distribution because they were characterized by a more variable "stiffer" population in comparison to the other cell lines with bimodal distribution.
- The 2C-induced stiffness decrease was lower for the highest-stiffness population than the lowest-stiffness one in cell lines that maintained their bimodality after the treatment. This indicated the "stiffer" population as prominent in 2C treatment response. In HEY, the stiffness decrease size was low for both populations, justifying its highest IC50 among the analyzed cell lines.
- The 2C had a good internalization after 6 hours from administration. After 7 hours from treatment the 2C-induced stiffness decrease had already occurred.
- The 2C treatment led to depolymerization of F-actin filaments in TYKNU, OVCAR4 and HEY. The organization of Actin cytoskeleton was related to 2C sensitivity and stiffness: the OVCAR4 and HEY (high stiffness and IC50) had a more distributed Actin cytoskeleton over the cell than TYKNU (low stiffness and IC50).
- The 2C had an indirect impact also on Microtubules network, which disaggregated after the drug treatment.
- The composition of the culture medium (nutrients and FBS concentrations) had an influence on mechanical properties.

## 7. References

- [1] Siegel, Rebecca, Miller and Ahmedin Jemal. "Cancer Statistics, 2019". CA: A Cancer Journal for Clinicians, 2019. 69 (1): 7-34.
- [2] Bray et al. "Global cancer statistics 2018: GLOBOCAN estimates of incidence and mortality worldwide for 36 cancers in 185 countries." CA: A Cancer Journal for Clinicians, 2018. 68(6): 394-424.
- [3] Stewart, Christine, Christine Ralyea and Suzy Lockwood. "Ovarian Cancer: An Integrated Review". Seminars in Oncology Nursing, 2019. 35(2): 151-156.
- [4] Testa, Ugo et al. "Ovarian Cancers: Genetic Abnormalities, Tumor Heterogeneity and Progression, Clonal Evolution and Cancer Stem Cells". Medicines, 2018. 5(1): 16.
- [5] Brett, Reid et al "Epidemiology of ovarian cancer: a review". Cancer Biology & Medicine, 2017. 14(1): 9-32.
- [6] Chen, Vivien et al "Pathology and classification of ovarian tumors". Cancer, 2003. 97(S10): 2631-42.
- [7] Boussios, Stergios et al. "Non-epithelial Ovarian Cancer: Elucidating Uncommon Gynaecological Malignancies" Anticancer Research, 2016. 36(10):5031-42.
- [8] Prat, Jaime, Emanuela D'angelo, and Espinosa "Ovarian Carcinomas: at least five different diseases with distinct histological features and molecular genetics". Human Pathology, 2018. 80:11-27.
- [9] Meinhold-Heerlein, Fotopoulou, Harter et al. "The new WHO classification of ovarian, fallopian tube, and primary peritoneal cancer and its clinical implications". Archives of Gynecology and Obstetrics, 2016. 293, 695–700.
- [10] Editorial Board WHOCOT. *WHO Classification of Tumours Female Genital Tumours: International Agency for Research on Cancer*; 2020.
- [11] Society AC. Cancer facts and figures 2017.
- [12] Society CC. Canadian cancer statistics 2017.
- [13] Grabowski, Harter, Heitz, Pujade-Lauraine, Reuss, Kristensen, Ray-Coquard, Heitz, Traut, Pfisterer, du Bois. "Operability and chemotherapy responsiveness in advanced low-grade serous ovarian cancer. An analysis of the AGO Study Group metadatabase". Gynecologic Oncology. 2016; 140:457–62.
- [14] Anis Kaldawy, Yakir Segev, Ofer Lavie, Ron Auslender, Victoria Sopik, Steven A. Narod, "Low-grade serous ovarian cancer: A review" Gynecologic Oncology", 2016. 143(2): 433-438.
- [15] Cancer Genome Atlas Research N. *Integrated genomic analyses of ovarian carcinoma*. Nature. 2011; 474:609–15.
- [16] Wong, Lu, Malpica, Bodurka, Shvartsman, Schmandt, Thornton, Deavers, Silva, Gershenson. "Significantly greater expression of ER, PR, and ECAD in advanced-stage low-

- grade ovarian serous carcinoma as revealed by immunohistochemical analysis.* International Journal of Gynecological Pathology. 2007; 26:404–9.
- [17] Xing, Rahmanto, Zeppernick, Hannibal, Kjaer, Vang, Shih, Wang. “*Mutation of NRAS is a rare genetic event in ovarian low-grade serous carcinoma.*” Human Pathology. 2017; 68:87–91.
- [18] Singer, Oldt R 3rd, Cohen, Wang, Sidransky, Kurman, Shih. “*Mutations in BRAF and KRAS characterize the development of low-grade ovarian serous carcinoma.*” Journal of the National Cancer Institute. 2003; 95:484–6.
- [19] Fernandez, Dawson, Hoenisch et al. “*Markers of MEK inhibitor resistance in low-grade serous ovarian cancer: EGFR is a potential therapeutic target.*” Cancer Cell International. 2019; 19, 10.
- [20] Jones, Tian-Li Wang, le-Ming Shih, Tsui-Lien Mao, Nakayama, Roden, Glas, Slamon, Diaz Jr., Vogelstein, Kinzler, Velculescu, Papadopoulos “*Frequent Mutations of Chromatin Remodeling Gene ARID1A in Ovarian Clear Cell Carcinoma*” Science. 2010; 330 (6001): 228-231.
- [21] Wentzensen et al “*Ovarian Cancer Risk Factors by Histologic Subtype: An Analysis From the Ovarian Cancer Cohort Consortium*” Journal of Clinical Oncology. 2016; 34(24): 2888–2898.
- [22] Kurman and Shih “*The Dualistic Model of Ovarian Carcinogenesis*” The American Journal of Pathology, 2016. 186(4):733-47.
- [23] Hee Yeon Lee et al “*Clinical Characteristics of Clear Cell Ovarian Cancer: A Retrospective Multicenter Experience of 308 Patients in South Korea*” Cancer Research and Treatment. 2020; 52(1): 277–283.
- [24] Chan, Teoh, Hu, Shin, Osann, Kapp “*Do clear cell ovarian carcinomas have poorer prognosis compared to other epithelial cell types? A study of 1411 clear cell ovarian cancers*” Gynecologic Oncology. 2008; 109(3): 370-376.
- [25] Sugiyama et al “*Clinical characteristics of clear cell carcinoma of the ovary*” Cancer, 2000; 88 (11): 2584-2589.
- [26] Hogen, Vicus, Ferguson et al “*Patterns of recurrence and impact on survival in patients with clear cell ovarian carcinoma*” International Journal of Gynecologic Cancer 2019; 29:1164-1169.
- [27] Kajiyama, Shibata, Mizuno et al “*Postrecurrent Oncologic Outcome of Patients with Ovarian Clear Cell Carcinoma*” International Journal of Gynecologic Cancer 2012; 22:801-806.
- [28] Iida, Okamoto, Hollis et al “*Clear cell carcinoma of the ovary: a clinical and molecular perspective*” International Journal of Gynecologic Cancer 2021; 31:605-616.
- [29] Bell et al. “*Integrated Genomic Analyses of Ovarian Carcinoma.*” Nature. 2011; 474.7353: 609–615.
- [30] Itamochi, Oishi, Oumi et al. “*Whole-genome sequencing revealed novel prognostic biomarkers and promising targets for therapy of ovarian clear cell carcinoma.*” British Journal of Cancer. 2017; 117: 717–724.

- [31] Samartzis, Noske, Dedes, Fink, Imesch. "ARID1A Mutations and PI3K/AKT Pathway Alterations in Endometriosis and Endometriosis-Associated Ovarian Carcinomas." *International Journal of Molecular Sciences*. 2013; 14: 18824-18849.
- [32] Yamashita, Akatsuka, Shinjo, Yatabe, Kobayashi, Seko et al. "Met Is the Most Frequently Amplified Gene in Endometriosis-Associated Ovarian Clear Cell Adenocarcinoma and Correlates with Worsened Prognosis." *PLoS ONE*. 2013; 8(3): e57724.
- [33] Ren-Chin Wu et al "Frequent somatic mutations of the telomerase reverse transcriptase promoter in ovarian clear cell carcinoma but not in other major types of gynaecological malignancy" *The Journal of Pathology*. 2014, 232(4): 473-481.
- [34] Storey et al "Endometrioid epithelial ovarian cancer: 20 Years of prospectively collected data from a single center" *American Chemical Society Journal*. 2008; 112(10): 2211-2220.
- [35] Pearce et al "Association between endometriosis and risk of histological subtypes of ovarian cancer: a pooled analysis of case-control studies", *The Lancet Oncology*. 2012; 13(4): 385-394.
- [36] Pierson, Peters, Chang, Chen, Quigley, Ashworth, Chapman, "An integrated molecular profile of endometrioid ovarian cancer", *Gynecologic Oncology*. 2020; 157(1): 55-61.
- [37] Soovares, Pasanen, Bützow, Lassus, "L1CAM expression associates with poor outcome in endometrioid, but not in clear cell ovarian carcinoma", *Gynecologic Oncology*, Volume 146, Issue 3, 2017, Pages 615-622, ISSN 0090-8258.
- [38] Cybulska et al, "Molecular profiling and molecular classification of endometrioid ovarian carcinomas", *Gynecologic Oncology*. 2019; 154(3): 516-523.
- [39] Cheasley, Wakefield, Ryland et al. "The molecular origin and taxonomy of mucinous ovarian carcinoma". *Nature Communications*. 2019. 10, 3935.
- [40] Ledermann, Luvero, Shafer et al "Gynecologic Cancer InterGroup (GCIg) Consensus Review for Mucinous Ovarian Carcinoma" *International Journal of Gynecologic Cancer* 2014; 24: S14-S19.
- [41] William "Mucinous Tumors of the Ovary: A Review" *International Journal of Gynecological Pathology*; 2005. 24(1): 4-25.
- [42] Simons et al. "A novel algorithm for better distinction of primary mucinous ovarian carcinomas and mucinous carcinomas metastatic to the ovary". *Virchows Archiv*. 2010; 474: 289-296.
- [43] Young et al., "Adjuvant therapy in stage I and stage II epithelial ovarian cancer. Results of two prospective randomized trials". *New England Journal of Medicine*, 1990. 322(15): 1021-7.
- [44] Penninkilampi, Ross, Eslick, Guy, "Perineal Talc Use and Ovarian Cancer" *Epidemiology*. 2018; 29(1): 41-49(9).
- [45] Fathalla "Incessant Ovulation – a factor in ovarian neoplasia?" *Lancet*, 1971, p.163.
- [46] Labidi-Galy, Papp, Hallberg et al. "High grade serous ovarian carcinomas originate in the fallopian tube". *Nature Communications*. 2017; 8, 1093.
- [47] Kurman and Shih, "Molecular Pathogenesis and Extraovarian Origin of Epithelial Ovarian Cancer – Shifting the Paradigm" *Human Pathology*. 2011; 42(7): 918-31.

- [48] Medeiros et al “*The Tubal Fimbria Is a Preferred Site for Early Adenocarcinoma in Women with Familial Ovarian Cancer Syndrome*” *The American Journal of Surgical Pathology*. 2006; 30(2): 230-236.
- [49] Lheureux, Braunstein, and Oza “*Epithelial ovarian cancer: Evolution of management in the era of precision medicine*”. *CA: A Cancer Journal for Clinicians*. 2019; 69(4): 280-304.
- [50] Gilks et al., “*Tumor cell type can be reproducibly diagnosed and is of independent prognostic significance in patients with maximally debulked ovarian carcinoma*”. *Human Pathology*. 2008; 39(8): 1239-51.
- [51] Soslow et al., “*Morphologic patterns associated with BRCA1 and BRCA2 genotype in ovarian carcinoma.*” *Modern Pathology*. 2012; 25(4): 625-36.
- [52] Howitt et al., “*Evidence for a dualistic model of high-grade serous carcinoma: BRCA mutation status, histology, and tubal intraepithelial carcinoma*”. *The American Journal of Surgical Pathology*. 2015; 39(3): 287-93.
- [53] Hui Zhang et al, “*Integrated Proteogenomic Characterization of Human High-Grade Serous Ovarian Cancer*”, *Cell*. 2016; 166(3): 755-765.
- [54] Konstantinopoulos et al., “*Homologous Recombination Deficiency: Exploiting the Fundamental Vulnerability of Ovarian Cancer*”. *Cancer Discovery*. 2015; 5(11): 1137-54.
- [55] Kuhn et al., “*TP53 mutations in serous tubal intraepithelial carcinoma and concurrent pelvic high-grade serous carcinoma-evidence supporting the clonal relationship of the two lesions*”. *Journal of Pathology*. 2012; 226(3): 421-426.
- [56] Berek, Crum, Friedlander, “*Cancer of the ovary, fallopian tube, and peritoneum*” *International Journal of Gynecology & Obstetrics*. 2015; 131(S2): S111-S122.
- [57] Associazione italiana di Oncologia Medica “*Linee guida per i tumori all’ovaio*”: 2018, 244.
- [58] Bristow et al., “*Survival effect of maximal cytoreductive surgery for advanced ovarian carcinoma during the platinum era: a meta-analysis*”. *Journal of Clinical Oncology*. 2002; 20(5): 1248-59.
- [59] Hennessy, Coleman, Markman, “*Ovarian cancer*”, *The Lancet*. 2009; 374(9698): 1371-1382.
- [60] Dasari and Tchounwou, “*Cisplatin in cancer therapy: Molecular mechanisms of action*”, *European Journal of Pharmacology*. 2014; 740: 364-378.
- [61] Weaver, “*How Taxol/paclitaxel kills cancer cells*” *Molecular Biology of the Cell*. 2014; 25(18): 2677-2890
- [62] Kim et al., “*FDA Approval Summary: Olaparib Monotherapy in Patients with Deleterious Germline BRCA-Mutated Advanced Ovarian Cancer Treated with Three or More Lines of Chemotherapy*”. *Clinical Cancer Research*. 2015; 21(19): 4257-61.
- [63] Schowalter “*Mechanics of Non-Newtonian Fluids*” Pergamon. 1978.
- [64] Engler, Sen, Sweeney and Discher, “*Matrix Elasticity Directs Stem Cell Lineage Specification*”, *Cell*. 2006; 126(4): 677-689.
- [65] Boal “*Mechanical properties of the cellular cytoskeleton*”. *Canadian Journal of Physics*. 1997; 53:228-236.
- [66] Fristch, Hockel, Kiessling, Kenechukwu, Wetzel, Zink and Kas “*Are biomechanical changes necessary for tumor progression?*”, *Nature Physics*. 2010; 6:370-372.

- [67] Sanger “*Changing patterns of actin localization during cell division*” Proceedings of the National Academy of Sciences of USA. 1975; 72(5): 1913-1916.
- [68] Thomas, Kirschmann, Cerhan, Folberg, Seftor, Sellers, Hendrix “*Association between keratin and vimentin expression, malignant phenotype, and survival in postmenopausal breast cancer patients*”. Clinical Cancer Research. 1999; 5(10): 2698-703.
- [69] Helmlinger, Netti, Lichtenbeld, Melder, Jain. “*Solid stress inhibits the growth of multicellular tumor spheroids*”. Nature Biotechnology. 1997; 15(8):778-83.
- [70] Park, Koch, Cardenas, Käs, Shih, “*Cell Motility and Local Viscoelasticity of Fibroblasts*”, Biophysical Journal. 2005; 89(6): 4330-4342.
- [71] Whipple, Balzer, Cho, Matrone, Yoon and Martin “*Vimentin Filaments Support Extension of Tubulin-Based Microtentacles in Detached Breast Tumor Cells*” Cancer Research. 2008; 68(14): 5678-5688.
- [72] Binnig, Quate and Gerber “*Atomic Force Microscope*” Physical Review Letters.1986; 56:930.
- [73] Malkin, Land, Kuznetsov, McPherson, and DeYoreo “*Investigation of Virus Crystal Growth Mechanisms by In Situ Atomic Force Microscopy*” Physical Review Letters. 1995; 75: 2778.
- [74] Kuznetsov, Low, Fan, McPherson, “*Atomic force microscopy investigation of wild-type Moloney murine leukemia virus particles and virus particles lacking the envelope protein*”, Virology. 2004; 323(2): 189-196.
- [75] Kuznetsov, Ulbrich, Haubova, Ruml, McPherson, “*Atomic force microscopy investigation of Mason–Pfizer monkey virus and human immunodeficiency virus type 1 reassembled particles*, Virology. 2007; 360(2): 434-446.
- [76] Chan, Lo, Liou, Lin, Syu, Lai, Chen, Li, “*Visualization of the structures of the hepatitis C virus replication complex*”, Biochemical and Biophysical Research Communications. 2011; 404(1): 574-578.
- [77] Del Sol, Armstrong, Wright, and Dyson “*Characterization of Changes to the Cell Surface during the Life Cycle of Streptomyces coelicolor: Atomic Force Microscopy of Living Cells*” Journal of Bacteriology. 2007; 189(6): 2219–2225.
- [78] Read, Connell and Adams “*Nanoscale Visualization of a Fibrillar Array in the Cell Wall of Filamentous Cyanobacteria and Its Implications for Gliding Motility*” Journal of Bacteriology. 2007, 189(20): 7361–7366.
- [79] Yang, Wang, Tan, He, Jin, Li “*Atomic force microscopy study of different effects of natural and semisynthetic beta-lactam on the cell envelope of Escherichia coli*” Analytical Chemistry. 2006; 78:7341-5.
- [80] Meincken, Holroyd, and Rautenbach “*Atomic Force Microscopy Study of the Effect of Antimicrobial Peptides on the Cell Envelope of Escherichia coli*” Antimicrobial Agents and Chemotherapy. 2005; 49(10): 4085–4092.
- [81] Kim, Cho, Park, Jung, Yoon, Park “*AFM-Detected Apoptotic Changes in Morphology and Biophysical Property Caused by Paclitaxel in Ishikawa and HeLa Cells*”. PLoS ONE. 2012, 7(1): e30066.
- [82] Plodinec, Loparic, Monnier et al. “*The nanomechanical signature of breast cancer*”. Nature Nanotechnology. 2012; 7: 757–765.

- [83] Florin, Moy, Gaub “*Adhesion forces between individual ligand-receptor pairs*” *Science*. 1994; 264(5157): 415-417
- [84] Müller and Engel, “*Voltage and pH-induced channel closure of porin OmpF visualized by atomic force microscopy*” *Journal of Molecular Biology*. 1999; 285(4): 1347-1351.
- [85] Kai-Chih Chang, Yu-Wei Chiang, Chin-Hao Yang, Je-Wen Liou, “*Atomic force microscopy in biology and biomedicine*”, *Tzu Chi Medical Journal*. 2012; 24(4): 162-169
- [86] Ting-Wei Mu, Derrick Sek Tong Ong, Ya-Juan Wang, Balch, Yates, Segatori, Kelly, “*Chemical and Biological Approaches Synergize to Ameliorate Protein-Folding Diseases*”, *Cell*. 2008; 134(5): 769-781.
- [87] Lodish, Berka, Matsudaira, Kaiser, Krieger, Scott “*Molecular Cell Biology-Lodish*” *Biologia celular y Molecular*, 2008.
- [88] Alberts, Bruce “*Molecular Biology of the Cell*” Sixth edition 2015, New York, NY: Garland Science, Taylor and Francis Group.
- [89] Díaz-Villanueva, Díaz-Molina, García-González “*Protein Folding and Mechanisms of Proteostasis*”. *International Journal of Molecular Sciences*. 2015; 16: 17193-17230.
- [90] Jung, Catalgol, Grune, “*The proteasomal system*”, *Molecular Aspects of Medicine*. 2009; 30(4): 191-296.
- [91] Pickart “*Mechanisms Underlying Ubiquitination*” *Annual Review of Biochemistry*. 2001; 70(1): 503-533.
- [92] Cooper “*The Cell*” 2<sup>nd</sup> ed. Sinauer Associates.
- [93] Huang, D'Andrea, “*Regulation of DNA repair by ubiquitylation*”. *Nature Reviews Molecular Cell Biology*. 2006; 7: 323–334.
- [94] Bard, Goodall, Greene, Jonsson, Dong, Martin “*Structure and Function of the 26S Proteasome*” *Annual Review of Biochemistry*. 2018; 87(1): 697-724.
- [95] Eletr, Wilkinson, “*Regulation of proteolysis by human deubiquitinating enzymes*”, *Biochimica et Biophysica Acta (BBA) - Molecular Cell Research*. 2014; 1843(1): 114-128.
- [96] Fraile, Quesada, Rodríguez et al. “*Deubiquitinases in cancer: new functions and therapeutic options*”. *Oncogene*. 2012; 31: 2373–2388.
- [97] Sgorbissa, Andrea et al. “*Isopeptidases in anticancer therapy: looking for inhibitors.*” *American Journal of Translational Research*. 2010; 2(3): 235-47.
- [98] Kane, Bross, Farrell, Pazdur “*Velcade®: U.S. FDA Approval for the Treatment of Multiple Myeloma Progressing on Prior Therapy*” *The Oncology*. 2003; 8(6): 508-513.
- [99] Raedler, Lisa. “*Velcade (Bortezomib) Receives 2 New FDA Indications: For Retreatment of Patients with Multiple Myeloma and for First-Line Treatment of Patients with Mantle-Cell Lymphoma.*” *American Health & Drug Benefits*. 2015; 8: 135-40.
- [100] Sharma, Preuss. “*Bortezomib*”. [Updated 2021 Feb 17]. EMA.
- [101] Tomasella et al. “*The isopeptidase inhibitor 2cPE triggers proteotoxic stress and ATM activation in chronic lymphocytic leukemia cells.*” *Oncotarget*. 2016; 7(29): 45429-45443
- [102] Coughlin et al “*Small-Molecule RA-9 Inhibits Proteasome-Associated DUBs and Ovarian Cancer In Vitro and In Vivo via Exacerbating Unfolded Protein Responses*” *Clinical Cancer Research*. 2014; 20(12): 3174-3186.

- [103] Cersosimo et al “*Synthesis, Characterization, and Optimization for in Vivo Delivery of a Nonselective Isopeptidase Inhibitor as New Antineoplastic Agent*” *Journal of Medical Chemistry*. 2015; 58(4): 1691–1704.
- [104] Santos, Moreira. “*Michael acceptors as cysteine protease inhibitors*”. *Mini Reviews in Medicinal Chemistry*. 2007; 10:1040-1050.
- [105] Foti, Floean, Pezzutto, Roncaglia, Tomasella, Gustincich and Brancolini “*Characterization of caspase-dependent and caspase-independent deaths in glioblastoma cells treated with inhibitors of the ubiquitin-proteasome system*” *Molecular Cancer Therapeutics*. 2009; 8(11): 3140-50.
- [106] Tomasella et al. “*A receptor-interacting protein 1 (RIP1)-independent necrotic death under the control of protein phosphatase PP2A that involves the reorganization of actin cytoskeleton and the action of cofilin-1.*” *The Journal of Biological Chemistry*. 2014; 289(37): 25699-710.
- [107] Cowley, Weir, Vazquez et al. “*Parallel genome-scale loss of function screens in 216 cancer cell lines for the identification of context-specific genetic dependencies*”. *Scientific Data*. 2014; 1, 140035.
- [108] Buick, Pullano and Trent “*Comparative Properties of Five Human Ovarian Adenocarcinoma Cell Lines*” *Basic Sciences*. 1985, 45(8).
- [109] Selby, Thomas, Monaghan et al. “*Human tumor xenografts established and serially transplanted in mice immunologically deprived by thymectomy, cytosine arabinoside and whole-body irradiation*”. *British Journal of Cancer*. 1980; 41: 52–61.
- [110] Bénard, Da Silva, De Blois, Boyer, Duvillard, Chiric and Riou “*Characterization of a Human Ovarian Adenocarcinoma Line, IGROV1, in Tissue Culture and in Nude Mice*” *Basic Sciences*. 1985; 45(10).
- [111] Wilson, Dent, Pejovic et al. “*Characterization of seven human ovarian tumor cell lines*”. *British Journal of Cancer*. 1996; 74: 722–727.
- [112] Louie, Behrens, Kinsella, Hamilton, Grotzinger, McKoy, Winker and Ozols “*Radiation Survival Parameters of Antineoplastic Drug-sensitive and -resistant Human Ovarian Cancer Cell Lines and Their Modification by Buthionine Sulfoximine*” *Basic Sciences*. 1985; 45(5).
- [113] Baguley, Marshall, Whittaker, Dotchin, Nixon, McCrystal, Finlay, Matthews, Holdaway, van Zijl, “*Resistance mechanisms determining the in vitro sensitivity to paclitaxel of tumour cells cultured from patients with ovarian cancer*”, *European Journal of Cancer*. 1995; 31(2): 230-237.
- [114] Morimoto, Yonehara and Bonavida “*Overcoming Tumor Necrosis Factor and Drug Resistance of Human Tumor Cell Lines by Combination Treatment with Anti-Fas Antibody and Drugs or Toxins*” *Experimental Therapeutic*. 1993; 53(11).
- [115] Fogh and Trempe “*New human tumor cell lines*” Fogh, J., ed. *Human tumor cell lines in vitro*. 1975; New York: Plenum Press.
- [116] Yoshiya “*Establishment of a cell line from human ovarian cancer (undifferentiated carcinoma of FIGO classification) and analysis of its cell-biological characteristics and sensitivity to anticancer drugs*”. *Nihon Sanka Fujinka Gakkai Zasshi*; 1986; 38(10): 1747-1753.
- [117] Yoshiya, Adachi, Misawa et al. “*Isolation of cisplatin-resistant subline from human ovarian cancer cell line and analysis of its cell-biological characteristics*”. *Nihon Sanka Fujinka Gakkai Zasshi*. 1989; 41(1): 7-14.

- [118] Ertel, Verghese, Byers et al. “*Pathway-specific differences between tumor cell lines and normal and tumor tissue cells*”. *Molecular Cancer*. 2006; 5(55).
- [119] Greb “*Introduction to Mammalian Cell Culture: Morphology and Cell Types & Organization*” Leica Microsystems 2017.
- [120] Pei-Hsun Wu et al “*Single-cell morphology encodes metastatic potential*” *Science Advances*. 2020; 6(4).
- [121] Nguyen, Yoshida, Goodarzi, Tavaoie, “*Highly variable cancer subpopulations that exhibit enhanced transcriptome variability and metastatic fitness*”. *Nature Communications*. 2016; 7:11246.
- [122] Abramoff, Magalhães, Ram “*Image processing with ImageJ*” *Biophotonics international*. 2004; 11(7): 36 – 42.
- [123] Haiyang Yu, Kee Pah Lim, Sijing Xiong, Lay Poh Tan, Winston Shim “*Functional Morphometric Analysis in Cellular Behaviors: Shape and Size Matter*” *Advanced Healthcare Materials*. 2013; 2(9): 1188-1197.
- [124] Jiahuan Chen, Ying Xu, Yan Shi, Tie Xia “*Functionalization of Atomic Force Microscope Cantilevers with Single-T Cells or Single-Particle for Immunological Single-Cell Force Spectroscopy*” *Journal of Visualized Experiments*. 2019; 149: e59609.
- [125] Thomas, Gawain et al. “*Measuring the mechanical properties of living cells using atomic force microscopy*.” *Journal of Visualized Experiments*. 2013; 76:50497.
- [126] JPK application note, 2015.
- [127] Pérez, Pérez, Méndez, Juan, Vazquez, Varela, Vera, Norma. (2018). “*Recent advances in atomic force microscopy for assessing the nanomechanical properties of food materials*”. *Trends in Food Science & Technology*. 2018; 8.
- [128] Hou, Li, Liu, Liu, Liu, Mi, “*Modulation of osteogenic potential by recombinant human bone morphogenic protein-2 in human periodontal ligament cells: effect of serum, culture medium, and osteoinductive medium*” *Journal of Periodontal Research*. 2007; 42(3): 244-252.
- [129] Nikkhah, Strobl, Schmelz, Agah, “*Evaluation of the influence of growth medium composition on cell elasticity*.” *Journal of Biomechanics*. 2011; 44(4) 2011, Pages 762-766, ISSN 0021-9290.
- [130] Van der Valk et al “*Fetal Bovine Serum (FBS): Past – Present – Future*” *Altex*. 2018; 35(1): 1 – 20.
- [131] Albini, Iwamoto, Kleinman, Martin, Aaronson, Kozlowski and McEwan “*A Rapid in Vitro Assay for Quantitating the Invasive Potential of Tumor Cells*” *Basic Sciences*. 1987; 47(12).
- [132] Moustakas, Stournaras “*Regulation of actin organisation by TGF-in H-ras transformed fibroblasts*”. *Journal of Cell Science*. 1999; 112: 1169–1179.
- [133] Ciotti et al. “*The binding landscape of a partially-selective isopeptidase inhibitor with potent pro-death activity, based on the bis(arylidene)cyclohexanone scaffold*.” *Cell death & disease*. 2018; 9(2): 184.
- [134] Sebaugh “*Guidelines for accurate EC50/IC50 estimation*” *Pharmaceutical statistics*. 2011; 10(2): 128-134.

- [135] Capani et al. "*Phalloidin-Eosin Followed by Photo-oxidation: A Novel Method for Localizing F-Actin at the Light and Electron Microscopic Levels*" *Journal of Histochemistry & Cytochemistry*. 2001; 49(11).
- [136] Zonderland, Wieringa, Moroni, "A quantitative method to analyse F-actin distribution in cells", *MethodsX*. 2019; 6: 2562-2569.
- [137] Anglesio, Wiegand, Melnyk, Chow, Salamanca, Prentice et al. "Type-Specific Cell Line Models for Type-Specific Ovarian Cancer Research". *PLoS ONE*. 2013; 8(9): e72162.
- [138] Domcke, Sinha, Levine et al. "Evaluating cell lines as tumour models by comparison of genomic profiles". *Nature Communications*. 2013; 4: 2126.
- [139] Constantinides, Chandran, Ulm, Vliet, "Grid indentation analysis of composite microstructure and mechanics: Principles and validation", *Materials Science and Engineering A*. 2006; 430: 189–202.
- [140] Larsson, Engqvist, Biermann et al. "Optimization of cell viability assays to improve replicability and reproducibility of cancer drug sensitivity screens". *Scientific Reports*. 2020; 10: 5798.
- [141] Leveque, Monteiro Carvalho and Maloisel "Clinical Pharmacokinetics of Bortezomib" *In vivo*. 2007; 21(2): 273-278.
- [142] Ramachandran, Quist, Kumar, Lal "Cisplatin nanoliposomes for cancer therapy: AFM and fluorescence imaging of cisplatin encapsulation, stability, cellular uptake, and toxicity" *Langmuir*. 2006; 22(19): 8156-8162.
- [143] Sharma, Santiskulvong, Bentolila, Rao, Dorigo, Gimzewski, "Correlative nanomechanical profiling with super-resolution F-actin imaging reveals novel insights into mechanisms of cisplatin resistance in ovarian cancer cells" *Nanomedicine: Nanotechnology, Biology and Medicine*. 2012; 8(5): 757-766.
- [144] Kroeger, Drapkin "Pathogenesis and heterogeneity of ovarian cancer." *Current Opinion in Obstetrics and Gynecology*. 2017; 29(1): 26-34.
- [145] Grady, Composto, Eckmann, "Cell elasticity with altered cytoskeletal architectures across multiple cell types", *Journal of the Mechanical Behavior of Biomedical Materials*. 2016; 61: 197-207.
- [146] Calzado-Martín, Encinar, Tamayo, Calleja, and San Paulo "Effect of Actin Organization on the Stiffness of Living Breast Cancer Cells Revealed by Peak-Force Modulation Atomic Force Microscopy" *ACS Nano*. 2016; 10(3): 3365–3374
- [147] Osborne, Li, How, O'Brien, Blobe, Superfine, and Myhre "TGF- $\beta$  regulates LARG and GEF-H1 during EMT to affect stiffening response to force and cell invasion" *Molecular Biology of the Cell*. 2014; 25(22): 3437-3716
- [148] Liu, Ching-Yi et al. "Vimentin contributes to epithelial-mesenchymal transition cancer cell mechanics by mediating cytoskeletal organization and focal adhesion maturation." *Oncotarget*. 2015; 6(18): 15966-83.
- [149] Braga, "Spatial integration of E-cadherin adhesion, signalling and the epithelial cytoskeleton", *Current Opinion in Cell Biology*. 2016; 42: 138-145.

- [150] Jalal, Shi, Acharya, Yun-Ju Huang, Viasnoff, Bershadsky, Yee Han Tee; “*Actin cytoskeleton self-organization in single epithelial cells and fibroblasts under isotropic confinement*”. *Journal of Cell Science*. 2019; 132(5): jcs220780.
- [151] Burridge. “*Focal adhesions: a personal perspective on a half century of progress*”. *FEBS Journal*. 2017; 284: 3355-3361.
- [152] Xu, Mezencev, Kim, Wang, McDonald, Sulchek “*Cell Stiffness Is a Biomarker of the Metastatic Potential of Ovarian Cancer Cells*”. *PLoS ONE*. 2012; 7(10): e46609.
- [153] Swaminathan, Mythreye, O'Brien, Berchuck, Blobe and Superfine “*Mechanical Stiffness Grades Metastatic Potential in Patient Tumor Cells and in Cancer Cell Lines*” *Cancer Research*. 2011; 71(15).
- [154] Hallas-Potts, Dawson & Herrington “*Ovarian cancer cell lines derived from non-serous carcinomas migrate and invade more aggressively than those derived from high-grade serous carcinomas*”. *Scientific Report*. 2019; 9: 5515.
- [155] Lengyel “*Ovarian cancer development and metastasis*”. *The American Journal of Pathology*. 2010; 177: 1053–1064.
- [156] Frixen, Behrens, Sachs, Eberle, Voss, Warda, Löchner, Birchmeier; “*E-cadherin-mediated cell-cell adhesion prevents invasiveness of human carcinoma cells*”. *Journal of Cell Biology*. 1991; 113(1): 173–185.
- [157] Sharma, Santiskulvong, Rao, Gimzewski, Dorigo, “*The role of Rho GTPase in cell stiffness and cisplatin resistance in ovarian cancer cells*”, *Integrative Biology*. 2014; 6(6) 611–617.
- [158] Fontanini et al. “*The Isopeptidase Inhibitor G5 Triggers a Caspase-independent Necrotic Death in Cells Resistant to Apoptosis: A COMPARATIVE STUDY WITH THE PROTEASOME INHIBITOR BORTEZOMIB.*” *The Journal of biological chemistry*. 2009; 284(13): 8369-81.
- [159] Raudenska, Kratochvilova, Vicar et al. “*Cisplatin enhances cell stiffness and decreases invasiveness rate in prostate cancer cells by actin accumulation*”. *Scientific Report*. 2019; 9: 1660.
- [160] Sum, Chi Shing et al. “*Establishing a High-content Analysis Method for Tubulin Polymerization to Evaluate Both the Stabilizing and Destabilizing Activities of Compounds.*” *Current chemical genomics and translational medicine*. 2014; 8(1) 16-26.
- [161] ChrzanowskaWodnicka, Burridge “*Rho-stimulated contractility drives the formation of stress fibers and focal adhesions*” *Journal of Cell Biology*. 1996; 133: 1403-1415
- [162] Ren, Kiosses, Schwartz “*Regulation of the small GTP-binding protein Rho by cell adhesion and the cytoskeleton*” *Embo Journal*. 1999; 18: 578-585.
- [163] Ananthkrishnan, Guck, Wottawah, Schinkinger, Lincoln, Romeyke, Moon, Kas “*Quantifying the contribution of actin networks to the elastic strength of fibroblasts*” *Journal of Theoretical Biology*. 2006; 242: 502-516.
- [164] Rotsch, Radmacher “*Drug-induced changes of cytoskeletal structure and mechanics in fibroblasts: an atomic force microscopy study*” *Biophysical Journal*. 2000; 78: 520-535.

- [165] Hunter, Sally et al. "Molecular profiling of low grade serous ovarian tumours identifies novel candidate driver genes." *Oncotarget*. 2015; 6(35): 37663-77.
- [166] Jones, Drapkin. "Modeling High-Grade Serous Carcinoma: How Converging Insights into Pathogenesis and Genetics are Driving Better Experimental Platforms". *Frontiers in Oncology*. 2013; 26(3):217.
- [167] Matulonis et al., "Ovarian cancer." *Nature Reviews Disease Primers*. 2016; 2: 16061.
- [168] <http://biomechanicalregulation-lab.org/afm>.
- [169] Turakhiya, Ankit. "Functional characterization of the role of ZFAND1 in stress granule turnover". Doctoral thesis, University of Wuerzburg, 2019.
- [170] Min, Hong, Lee. "Interleukin-6 expression by interactions between gynecologic cancer cells and human mesenchymal stem cells promotes epithelial-mesenchymal transition." *International Journal of Oncology*. 2015; 47: 1451-1459.
- [171] <https://www.atcc.org/products/htb-75>.
- [172] <https://www.atcc.org/products/htb-77>.
- [173] <https://cellbank.nibiohn.go.jp/legacy/celldata/jcrb0234.1.htm>.
- [174] <https://www.ebiohippo.com/en/cell-lines/human-ovary-adenocarcinoma-cell-line-oaw-42-bhc11100602.html>.
- [175] [http://ezbiosystems.com/view2.asp?d\\_id=333&Name=OVCAR-4%20Cell%20Avalanche%AE%20Transfection%20Reagent%20\(human%20ovary%20carcinoma%20cell\)](http://ezbiosystems.com/view2.asp?d_id=333&Name=OVCAR-4%20Cell%20Avalanche%AE%20Transfection%20Reagent%20(human%20ovary%20carcinoma%20cell)).
- [176] <https://rsscience.com/how-to-use-a-hemocytometer-to-count-cells/>.
- [177] Deng, Xiong, Li et al. "Application of atomic force microscopy in cancer research". *Journal of Nanobiotechnology*. 2018; 16: 102.
- [178] Helenius, Heisenberg, Gaub, Muller. "Single-cell force spectroscopy". *Journal of Cell Science*. 2008; 121: 1785 - 1791.
- [179] Pérez, Pérez, Méndez, Vazquez, Hernández-Varela, Vera, Norma. (2018). "Recent advances in atomic force microscopy for assessing the nanomechanical properties of food materials". *Trends in Food Science & Technology*. 2018; 87(10).
- [180] <https://www.cellbiolabs.com/sites/default/files/CBA-100-C-cell-migration-invasion-assay.pdf>
- [181] Wang, Ren, Li, Song, Chen, Ouyang, Ling. (2019). "Ellagic acid exerts antitumor effects via the PI3K signaling pathway in endometrial cancer." *Journal of Cancer*. 2019; 10: 3303-3314.
- [182] Beam, Motsinger-Reif, Alison. (2014). "Beyond IC50s: Towards Robust Statistical Methods for in vitro Association Studies." *Journal of pharmacogenomics & pharmacoproteomics*. 2014; 5.
- [183] Wang-Shick Ryu, "Chapter 4 - Diagnosis and Methods" *Molecular Virology of Human Pathogenic Viruses*, Academic Press, 2017. 47-62.

- [184] Hodges, Lehmann (1956). "*The efficiency of some nonparametric competitors of the  $t$ -test*". *The Annals of Mathematical Statistics*. 1956; 27:324–335.
- [185] Spearman "*The Proof and Measurement of Association between Two Things*" *The American Journal of Psychology*. 1904; 15: 72–101.
- [186] Anderson and Darling "*A Test of Goodness of Fit*", *Journal of the American Statistical Association*. 1954, 49: 765-769.
- [187] Mann "*Non-parametric tests against trend*" *Econometrica*. 1945; 13:163-171.